Available online at www.sciencedirect.com

SciVerse ScienceDirect

Procedia Engineering 00 (2012) 000–000

Procedia Engineering

www.elsevier.com/locate/procedia

5th BSME International Conference on Thermal Engineering

Effects of Dean Number and Curvature on Fluid Flow through a Curved Pipe with Magnetic Field

Md. Mainul Hoque[a] and Md. Mahmud Alam[b]

[a]*Departmetnt of Electrical and Computer Engineering, Presidency University,Gulshan, Dhaka-1212, Bangladesh*
[b]*Mathematics Discipline, Khulna University, Khulna-9208, Bangladesh*

Abstract

Numerical study is performed to investigate the Magnetohydrodynamics fluid flow through a curved pipe with circular cross-section under various conditions. Spectral method is applied as a main tool for the numerical technique; where, Fourier series, Chebyshev polynomials, Collocation methods, and Iteration method are used as secondary tools. The Magnetohydrodynamics incompressible viscous steady flow through a curved pipe with circular cross-section is investigated numerically to examine the combined effects of high Dean Number D_n, magnetic parameter M_g and non- dimensional curvature δ. The flow patterns have been shown graphically for large Dean Numbers as well as magnetic parameter and a wide range of curvatures $0.01 \le \delta \le 0.4$.Two vortex solutions have been found. Axial velocity has been found to increase with the increase of Dean Number and decrease with the increase of curvature and magnetic parameter. For high magnetic parameter, Dean Number and low curvature almost all the fluid particles strength are weak.

Keywords: *Dean Number; Magnetic parameter and Curvature*

Nomenclature

D_n	Dean Number
M_g	Magnetic Parameter
δ	Non-dimensional Curvature of the Pipe
$\sigma^{/}$	Electrical Conductivity
J	Current density
H	Magnetic field
μ_e	Magnetic Permeability

1. Introduction

Fully developed flow in curved ducts is encountered in various practical processes. In the analysis of fluidic devices, flows in separation processes, heat exchangers, physiological systems are examples of such processes. In the past few decades, most of the research works have been done on the fully developed flow through curved ducts. Therefore, the fully developed flow phenomena in the curved ducts with magnetic field have drawn a keen attention.

* Corresponding author. Tel. +88 01912 982 811; +88 01712 343 063
E-mail address: alam_mahmud2000@yahoo.com; pavel.math.ku@gmail.com

Dean (1927) first formulated the curved duct problem mathematically under the fully developed flow conditions and confirmed the existence of a pair of counter rotating vortices as a secondary flow in the curved pipe. For the fully developed flow in a curved circular pipe, Ito (1951) separately showed the existence of a two-vortex secondary flow patterns by using perturbation method as was done by Dean (1927). Cheng and Akiyama (1970) and Cheng et al. (1975) reported two-vortex secondary flow patterns in a curved duct with square cross-section by using finite difference method. Masliyah (1980) investigated both numerically and experimentally the flow through a semi-circular duct with a flat outer wall. He found the existence of dual solution i.e. both two-vortex and four-vortex secondary flow patterns exist at the same Dean number. Both Nandakumar and Masliyah (1982) and Dennis and Ng (1982) separately obtained dual solution for the flow through a curved tube with circular cross-section. They found that two-vortex solution and four-vortex solution coexist. Later, the stability of the dual solutions of two-vortex and four-vortex secondary flow patterns was studied by Yanase et al. (1989). They found that the two-vortex secondary flow patterns are stable while the four-vortex flow patterns are unstable. In the numerical research works by Shanthini and Nandakumar (1986), Winters (1987) and Daskopolous and Lenhoff (1989), dual solutions for fully developed flow in a curved duct of square cross-section are found. Yang and Wang (2001) studied numerically the bifurcation structure and stability of the solutions of fully developed viscous flow in curved square duct. The governing equations were discretized by using the finite volume method.

Dean's work was extended by Reid (1958). Dean vortices were observed experimentally by Brewster et al. (1959) in a channel with an aspect ratio of 35 and a curvature ratio of 12.5. Later, Finlay (1989) used a weakly non-linear perturbation analysis to determine the non-linear equation of two dimensional vortices in a curved channel with infinite aspect ratio. Finlay and Nandakumar (1990) investigated the onset of Dean vortices in curved rectangular channels with aspect ratios ranging from 20 to 30. They used two dimensional finite difference methods in this investigation and found vortex pairs in the centre of the channel.

The effects of the magnetic field on fluid flow have been studied primarily for straight pipes by Chang and Lundgren (1961), Shercliff (1956), Walker (1986) and Holroyd (1978). Shercliff (1956) solved the problem of flow in circular pipes under transverse magnetic fields in an approximate manner for large Hartmann numbers assuming walls of zero and small conductivity. The effect of wall conductivity was also studied by Chang and Lundgren (1961). Pressure drop in thin walled circular straight ducts was studied by Holroyed and Walker [9], neglecting the inertial effects and induced magnetic field. Recently, Walker (1986) developed solutions to MHD flow equations by asymptotic analysis for circular straight ducts under strong transverse magnetic fields.

At present, our aim is to obtain a detail results on the Dean numbers as well as magnetic parameter at curvatures $(\delta) = 0.01$ and 0.2. In this present study, the magnetic field has been imposed along the centre line of a curved pipe.

2. Governing Equation

The basic equations for steady laminar flow are

Continuity: $\nabla.\mathbf{q} = 0$ (1)

Navier-Stoke's equation for incompressible fluid is

$$\frac{\partial \mathbf{q}}{\partial t} + (\mathbf{q}.\nabla)\mathbf{q} = F - \frac{1}{\rho}\nabla p + \upsilon \nabla^2 \mathbf{q} \tag{2}$$

Now, in the equation of motion appears a body force $\frac{1}{\rho} J \wedge B$ per unit volume of electro- magnetic origin. If there is no other body force then the equation (2) becomes

$$\frac{\partial \mathbf{q}}{\partial t} + (\mathbf{q}.\nabla)\mathbf{q} = -\frac{1}{\rho}\nabla p + \upsilon \nabla^2 \mathbf{q} + \frac{1}{\rho} J \wedge B \tag{3}$$

Let us consider a curved pipe with circular cross-section containing incompressible inviscid fluid. Let the radius of the pipe be L, radius of cross-section be a (Fig. 1). To reach the point (x, y, z) we have to travel $L + r$ unit ($0 \le r \le a$) along *x*-axis, then turn an angle θ considering the origin as centre in the *xy* plane, then turn again an angle α in the plane of cross-section. Then (x, y, z) and (r, α, θ) are related as,

$$x = (L + r\cos\alpha)\cos\theta,\ y = (L + r\cos\alpha)\sin\theta,\ z = r\sin\alpha$$

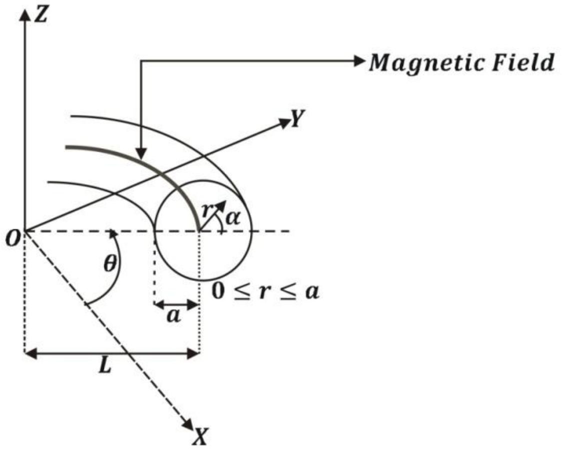

Fig.1. Toroidal Coordinate system for curved pipe with magnetic field

Let $\mathbf{q} = q_x\mathbf{i} + q_y\mathbf{j} + q_z\mathbf{k} = q_r\mathbf{e_r} + q_\alpha\mathbf{e_\alpha} + q_\theta\mathbf{e_\theta}$ be the velocity of a particle of the fluid when it is supposed to a constant pressure gradient force only. So the equation of continuity takes the form,

$$\nabla.\mathrm{q} = \frac{\partial}{\partial r}\left\{r\left(L + r\cos\alpha\right)q_r\right\} + \frac{\partial}{\partial\alpha}\left\{\left(L + r\cos\alpha\right)q_\alpha\right\} + \frac{\partial}{\partial\theta}\left\{rq_\theta\right\} = 0 \tag{4}$$

By using Ohm's law and Maxwell's equation the Navier-Stokes equation in the radial, circumferential and axial direction becomes.

Radial direction (from the coefficient of $\mathbf{e_r}$)

$$\begin{aligned}
&\frac{\partial q_r}{\partial t} + \left\{q_r\frac{\partial}{\partial r} + \frac{q_\alpha}{r}\frac{\partial}{\partial\alpha} + \frac{q_\theta}{\left(L + r\cos\alpha\right)}\frac{\partial}{\partial\theta}\right\}q_r - \frac{q_\alpha^2}{r} - \frac{q_\theta^2\cos\alpha}{\left(L + r\cos\alpha\right)} \\
&\quad = -\frac{1}{\rho}\frac{\partial p}{\partial r} - \upsilon\left\{\begin{matrix}\left(\dfrac{\partial}{r\partial\alpha} - \dfrac{\sin\alpha}{\left(L + r\cos\alpha\right)}\right)\left(\dfrac{\partial q_\alpha}{\partial r} + \dfrac{q_\alpha}{r} - \dfrac{\partial q_r}{r\partial\alpha}\right) - \\ \dfrac{1}{\left(L + r\cos\alpha\right)^2}\dfrac{\partial^2 q_r}{\partial\theta^2} + \dfrac{1}{L + r\cos\alpha}\left(\dfrac{\partial^2 q_\theta}{\partial\theta\partial r} + \dfrac{rq_\theta\cos\alpha}{\left(L + r\cos\alpha\right)}\dfrac{\partial q_\theta}{\partial\theta}\right)\end{matrix}\right\} - \frac{\sigma^{/}\mu_e^2}{\rho}q_r H_\theta^2
\end{aligned}$$

Circumferential direction (from coefficient of $\mathbf{e_\alpha}$)

$$\begin{aligned}
&\frac{\partial q_\alpha}{\partial t} + \left(q_r\frac{\partial}{\partial r} + \frac{q_\alpha}{r}\frac{\partial}{\partial\alpha} + \frac{q_\theta}{L + r\cos\alpha}\frac{\partial}{\partial\theta}\right)q_\alpha + \frac{q_r q_\alpha}{r} + \frac{\sin\alpha}{L + r\cos\alpha}q_\theta^2 \\
&\quad = -\frac{1}{\rho}\frac{\partial p}{r\partial\alpha} - \upsilon\left\{\begin{matrix}\dfrac{1}{r\left(L + r\cos\alpha\right)}\dfrac{\partial^2 q_\theta}{\partial\theta\partial\alpha} - \dfrac{\sin\alpha}{\left(L + r\cos\alpha\right)^2}\dfrac{\partial q_\theta}{\partial\theta} - \dfrac{1}{\left(L + r\cos\alpha\right)^2}\dfrac{\partial^2 q_\alpha}{\partial\theta^2} \\ -\left(\dfrac{\cos\alpha}{\left(L + r\cos\alpha\right)} + \dfrac{\partial}{\partial r}\right)\left(\dfrac{q_\alpha}{r} + \dfrac{\partial q_\alpha}{\partial r} - \dfrac{\partial q_r}{r\partial\alpha}\right)\end{matrix}\right\} - \frac{\sigma^{/}\mu_e^2}{\rho}q_\alpha H_\theta^2
\end{aligned}$$

Axial direction (from coefficient of $\mathbf{e}_\theta$)

$$\frac{\partial q_\theta}{\partial t}+\left(q_r\frac{\partial}{\partial r}+\frac{q_\alpha}{r}\frac{\partial}{\partial \alpha}+\frac{q_\theta}{L+r\cos\alpha}\frac{\partial}{\partial\theta}\right)q_\theta+\frac{\cos\alpha}{L+r\cos\alpha}q_r q_\theta-\frac{\sin\alpha}{L+r\cos\alpha}q_\alpha q_\theta$$
$$=-\frac{1}{\rho}\frac{1}{L+r\cos\alpha}\frac{\partial p}{\partial\theta}+\upsilon\left\{\begin{array}{r}\left(\frac{1}{r}+\frac{\partial}{\partial r}\right)\frac{\partial q_\theta}{\partial r}+\left(\frac{1}{r}+\frac{\partial}{\partial r}\right)\frac{q_\theta\cos\alpha}{(L+r\cos\alpha)}+\frac{1}{r^2}\frac{\partial^2 q_\theta}{\partial\alpha^2}-\frac{\partial}{r\partial\alpha}\left\{\frac{q_\theta\sin\alpha}{(L+r\cos\alpha)}\right\}\\ -\left(\frac{1}{r}+\frac{\partial}{\partial r}\right)\left\{\frac{1}{(L+r\cos\alpha)}\frac{\partial q_r}{\partial\theta}\right\}-\frac{\partial}{r\partial\alpha}\left\{\frac{1}{(L+r\cos\alpha)}\frac{\partial q_\alpha}{\partial\theta}\right\}\end{array}\right\}$$

3. Toroidal Coordinates

Let us defined the following non-dimensional variables

$$u'=\frac{q_r}{\frac{\upsilon}{a}}\qquad v'=\frac{q_\alpha}{\frac{\upsilon}{a}}\qquad w'=\frac{q_\theta}{\frac{\upsilon}{a}}\sqrt{\frac{2a}{L}}\qquad r'=\frac{r}{a}\qquad S'=\frac{L\theta}{a}\qquad \frac{a}{L}=\delta\qquad p'=\frac{p}{\rho\left(\frac{\upsilon}{a}\right)^2}$$

where u',v',w' are non-dimensional velocities along the radial, circumferential and axial direction respectively. r' is non-dimensional radius, S' is the non-dimensional axial variable, δ is non-dimensional curvature and p' non-dimensional pressure.

Constant pressure gradient force is applied along the axial direction through the centre of cross section. At the centre of the cross-section $r=0$ and at the boundary of the cross-section $r=a$, where all the velocity components are zero. In dimensionless form this reduces to $r'=0$ at the centre of cross-section and $r'=1$ at the boundary of the cross-section. With the help of the above dimensionless variables and the boundary conditions the radial and circumferential equation of motion reduces to the following form:

$$\frac{1}{r'}\left\{\frac{\partial\psi}{\partial r'}\frac{\partial(\Delta\psi)}{\partial\alpha}-\frac{\partial\psi}{\partial\alpha}\frac{\partial(\Delta\psi)}{\partial r'}\right\}+\Delta^2\psi\ +w'\left(\sin\alpha\frac{\partial w'}{\partial r'}+\frac{\cos\alpha}{r'}\frac{\partial w'}{\partial\alpha}\right)-M_g\Delta\psi=0 \qquad (5)$$

and the axial equation becomes

$$\frac{1}{r'}\left(\frac{\partial\psi}{\partial r'}\frac{\partial w'}{\partial\alpha}-\frac{\partial\psi}{\partial\alpha}\frac{\partial w'}{\partial r'}\right)+\Delta w'+D_n=0 \qquad (6)$$

where, $\Delta\equiv\frac{\partial^2}{\partial r'^2}+\frac{1}{r'}\frac{\partial}{\partial r'}+\frac{1}{r'^2}\frac{\partial^2}{\partial\alpha^2}$, $G=-\frac{\partial p}{\partial S}$, $D_n=\frac{a^3}{\mu\upsilon}\sqrt{\frac{2a}{L}}G$ and $M_g=\sigma^/\mu_e a^2H_\theta^2$. Here, ψ is the stream function defined by, $u'=\frac{1}{r'}\frac{\partial\psi}{\partial\alpha}$, $v'=-\frac{\partial\psi}{\partial r'}$, G is the constant pressure gradient force, μ is the viscosity, υ is the kinematic viscosity, D_n is the Dean number and M_g is the magnetic parameter. Equation (5) and (6) are called secondary and axial flow respectively. The dimensionless flux κ is given by, $\kappa=\frac{\sqrt{2}}{\pi}\int_0^1 r'\int_0^{2\pi} w'd\alpha dr'$.

4. Numerical Technique

The Spectral method which is a very useful numerical tool for solving Navier-Stokes equation(Gottelib and Orszag 1977) has been used to solve the equations (1) and (2). Fourier series and Chebyshev polynomials are used in circumferential and radial directions respectively. Assuming that steady solution is symmetric with respect to the horizontal line of the cross-section, ψ and w' are expanded as,

$$\psi(r',\alpha)=\sum_{n=1}^{N} f_n^s(r')\sin n\alpha+\sum_{n=0}^{N} f_n^c(r')\cos n\alpha \text{ and } w'(r',\alpha)=\sum_{n=1}^{N} w_n^s(r')\sin n\alpha+\sum_{n=0}^{N} w_n^c(r')\cos n\alpha$$

The collocation points are taken to be, $R=\cos\left\{\dfrac{N+2-i}{N+2}\right\}\pi\ [1\le i\le N+1]$. Then we get non-linear equations for $W_{nm}^s, W_{nm}^c, F_{nm}^s, F_{nm}^c$. The obtained non-linear algebraic equations are solved under by an iteration method with under-relaxation. Convergence of this solution is taken up to five decimal places by taking $\varepsilon_{\mathrm{p}} < 10^{-5}$. Where

$$\varepsilon_p=\sum_{n=1}^{N}\sum_{m=0}^{M}\left[\left(F_{mn}^{s(p)}-F_{mn}^{s(p+1)}\right)^2+\left(W_{mn}^{s(p)}-W_{mn}^{s(p+1)}\right)^2\right]+\sum_{n=0}^{N}\sum_{m=0}^{M}\left[\left(F_{mn}^{c(p)}-F_{mn}^{c(p+1)}\right)^2+\left(W_{mn}^{c(p)}-W_{mn}^{c(p+1)}\right)^2\right]$$

Here, p is the iteration number. The values of M and N are taken to be 60 and 35 respectively for better accuracy.

5. Results and Discussions

Flow through a curved pipe of circular cross section with Magnetic field has been considered. The flow is governed by two non dimensional parameters: the Dean number (D_n) and the magnetic parameter (M_g). In this paper, steady laminar flow for viscous incompressible fluid has been analyzed under the action Dean numbers as well as magnetic parameter at curvatures $\delta = 0.01$ and 0.2.

The results have been shown through stream line, vector plots of the secondary flow and contour plots of the axial flow. The stream line, vector and contour plots of the flow development have been shown at different magnetic parameters for Dean number $D_n = 800$, 1500 and 2000 at non-dimensional curvature $\delta = 0.01$ and 0.2 which are arranged in a column form left to right. In each figure, six columns have been produced. Among them the first three columns shows the stream line, vector plots of the secondary flow and contour plots of the axial flow behaviours for non-dimensional curvature $\delta = 0.01$ at different Dean number. Similarly, the last three columns shows the stream line, vector plots of the secondary flow and contour plots of the axial flow behaviours for non-dimensional curvature $\delta = 0.2$ at different Dean number as well as magnetic parameter.

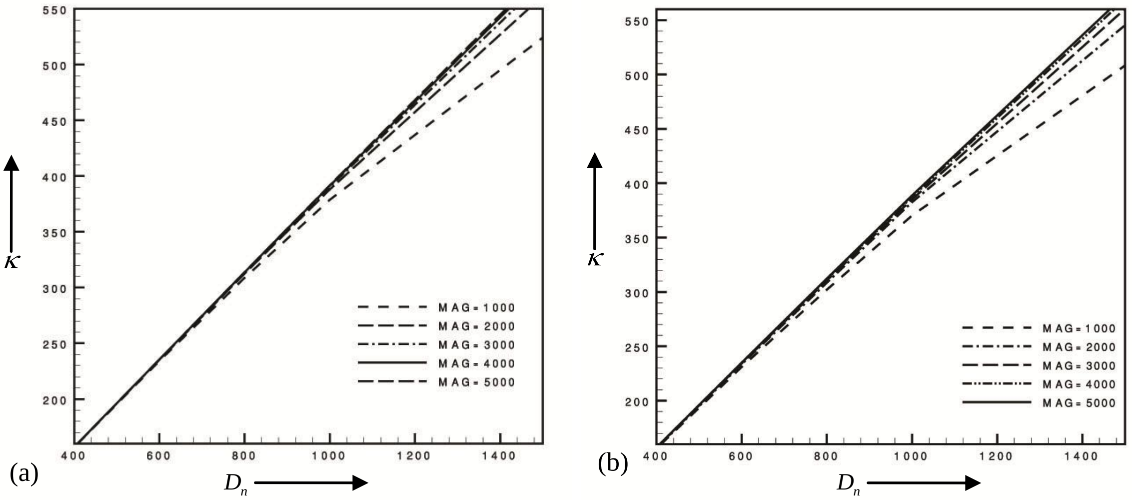

Fig. 2. (a) Dean number D_n versus non-dimensional flux for non- dimensional curvature $\delta = 0.01$ and (b) Dean number D_n versus non-dimensional flux for non- dimensional curvature 0.2 respectively.

In Fig. 2 non-dimensional flux (κ) has been plotted against Dean number at δ = 0.01 and 0.2 for different magnetic parameter respectively. And for each figure it is clear that the flux increases with the increase of Dean number as well as magnetic parameter. But if the magnetic parameter increases continuously the rate of change of flux is negligible. It is found that if the magnetic parameter increased then total flow will automatically be increased for each figure. And finally after a comprehensive survey over the parametric space, steady solution curve has been obtained in Fig. 3-Fig. 5.

The stream line, vector plots of the secondary flow and axial flow for Dean Number D_n = 800, 1500, 2000 at non-dimensional curvature δ = 0.01 and 0.2 have been shown at the first, second and third column respectively in Fig. 3- Fig. 5. The highest values of magnetic parameter, increment in axial velocity (Δw), increment in constant $\psi -$lines $(\Delta\psi)$ have been given on the left side.

The length of arrow indicates the ratio of the stream velocity to the axial velocity and the direction of the flow in vector plots are always indicates by an arrowhead, no matter how small the flow is. Thus, the relative strength of the flow is not resolved for areas of a very weak secondary flow. In Fig. 3 the vector plots of the secondary flow show the direction of the fluid particles and the strength of the vortex is shifted towards outer half of the cross-section as magnetic parameter increases.

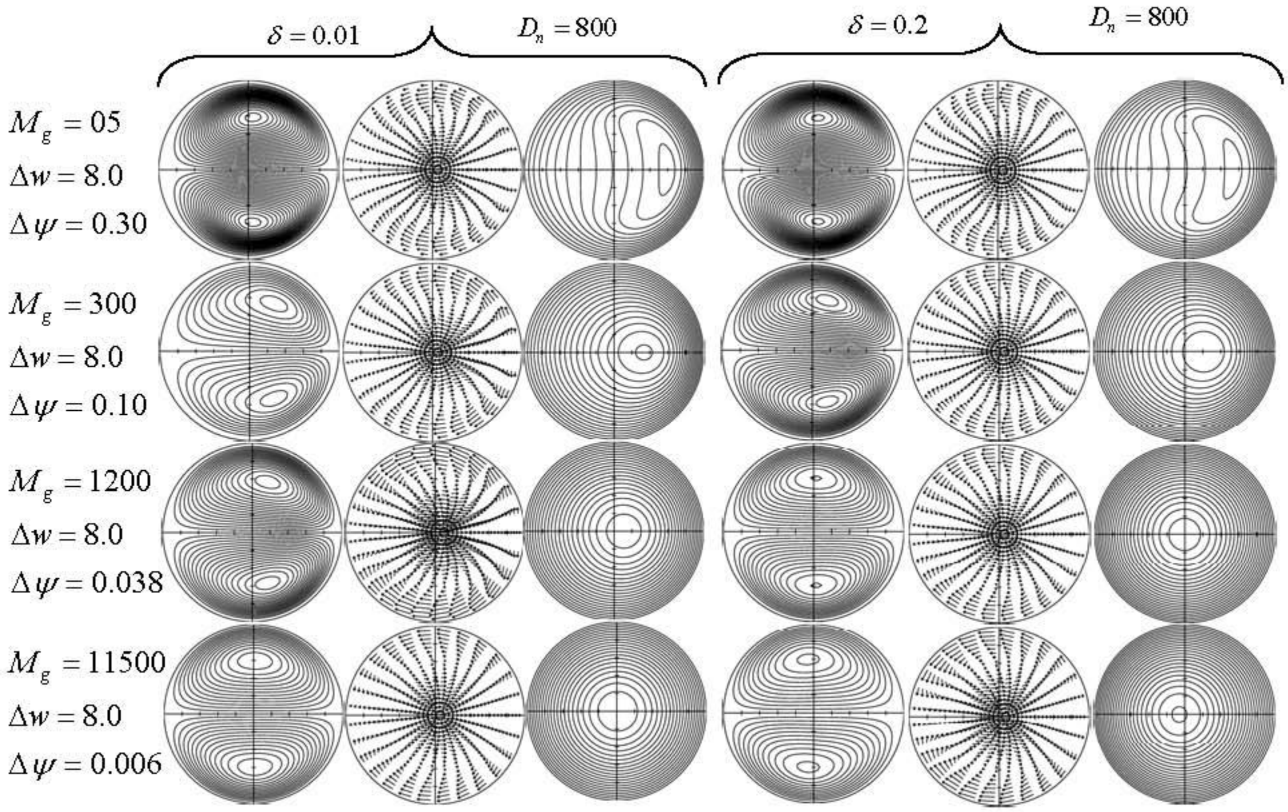

Fig. 3. The secondary flow, vector plots of the secondary flow and axial flow for different values of magnetic parameter at Dean Number D_n = 800

In case of secondary flow behaviour, symmetric contour plots have been found which are shown Fig 3. As magnetic parameter increases there originate a secondary flow and only 2-vortex solution has been found for the secondary flow. The two vortexes are of same strength but rotating in counter clockwise direction. In Fig. 3 the axial flow is greater in magnitude than secondary flow and it varies a great deal with magnetic parameter. As a result the difference between two consecutive contours line of the axial flow have been taken different for different magnetic parameters. For high magnetic parameter, Dean number and low curvature, the axial flow is shifted towards the centre of the pipe as a result almost all the fluid particles strength are weak.

In case of axial flow behaviour (Fig. 4), the axial flow is also symmetric. The fluid particles are shifted towards the outer wall of the cross section and form a *low velocity band* inside the outer wall of the cross-section in Fig. 4. As magnetic parameter decreases the magnitude of the axial flow gets higher. The axial flow decreases with the increase of Magnetic parameter. Also the maximum axial flow is shifted to the centre from the wall of the cross section as Magnetic parameter increases. With the development of the flow, the magnitude of the secondary velocity decreases up to a certain limit. When the flow is fully developed, it does not change further.

Two vortex secondary flows have been found which is symmetric about the horizontal line passing through the centre of the cross section with the presence of magnetic field in Fig. 4. Most of the particle gets the radial velocity. The two vortexes are of same strength but rotating in opposite direction. Where the upper vortex is rotating anti–clock wise and the lower vortex is rotating clock wise. At $M_g = 500$ and $D_n = 2000$ axial flow contours are nearly circular and are eccentric with the centres shifted towards the outer wall of the tube pipe in Fig 5. At $M_g = 25000$ a strong magnetic field has been found to confine the secondary flow streamlines to a thin layer near the tube wall. The secondary flow rate in the near wall boundary is increased by the magnetic field. The stable solution zone initially increases with the increase of curvature.

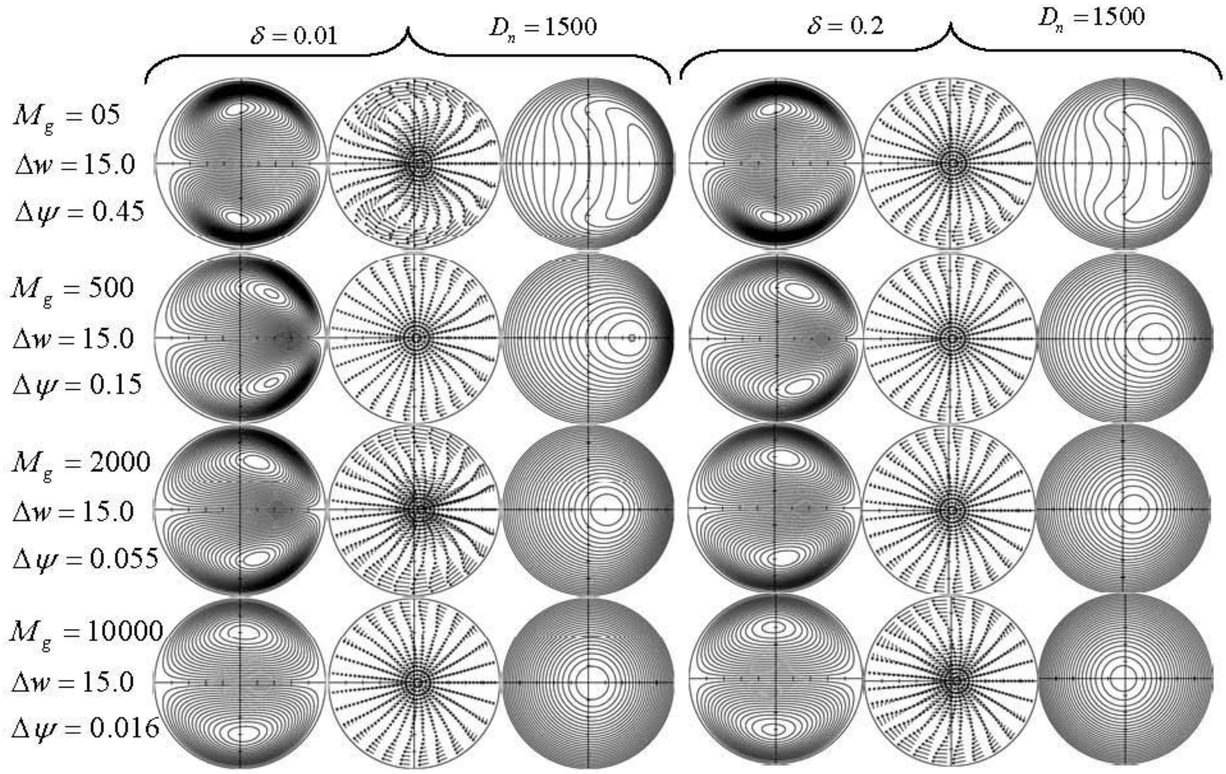

Fig. 4. The secondary flow, vector plots of the secondary flow and axial flow for different values of magnetic parameter at Dean Number $D_n = 1500$

In Fig. 5 the largest magnetic parameter to give stable solution as well as an extra circular zone is $M_g = 25000$ for $D_n = 2000$. The contour plots of the axial velocity have been shown in Fig 5. for magnetic parameter $M_g = 20$, 150, 1500, 3000, 25000 respectively at $D_n = 2000$.

As the flow enters the pipe boundary layer begins to develop. Boundary layer near the inner wall develops faster than that at the outer wall. Just after the entrance, the axial velocity of the particle in the inner half is lower for small curvature. But as the flow precedes downstream the particles in outer half attains higher velocity.

Due to the effect of magnetic field a ***bracelet*** has been originates from the right corner of the duct and expands at $M_g = 1500$ in Fig. 5. This bracelet gradually increases with the increase of magnetic parameter and shifted to the centre. In Fig. 5. the bracelet finally dropped to the centre at $M_g = 25000$. In the case, of vector plots of secondary flow (Fig. 5) a clock wise rotating vortex is set up after the entrance at $M_g = 20$. Also an anti–clock wise rotating vortex originates from the top and expands. On the other hand the secondary velocity of the particles around the centre of cross–section decreases starting from the particles above the centre to the particles below the centre in Fig. 5. Finally a strong magnetic field is found to confine the secondary flow streamlines to a thin layer near the tube wall.

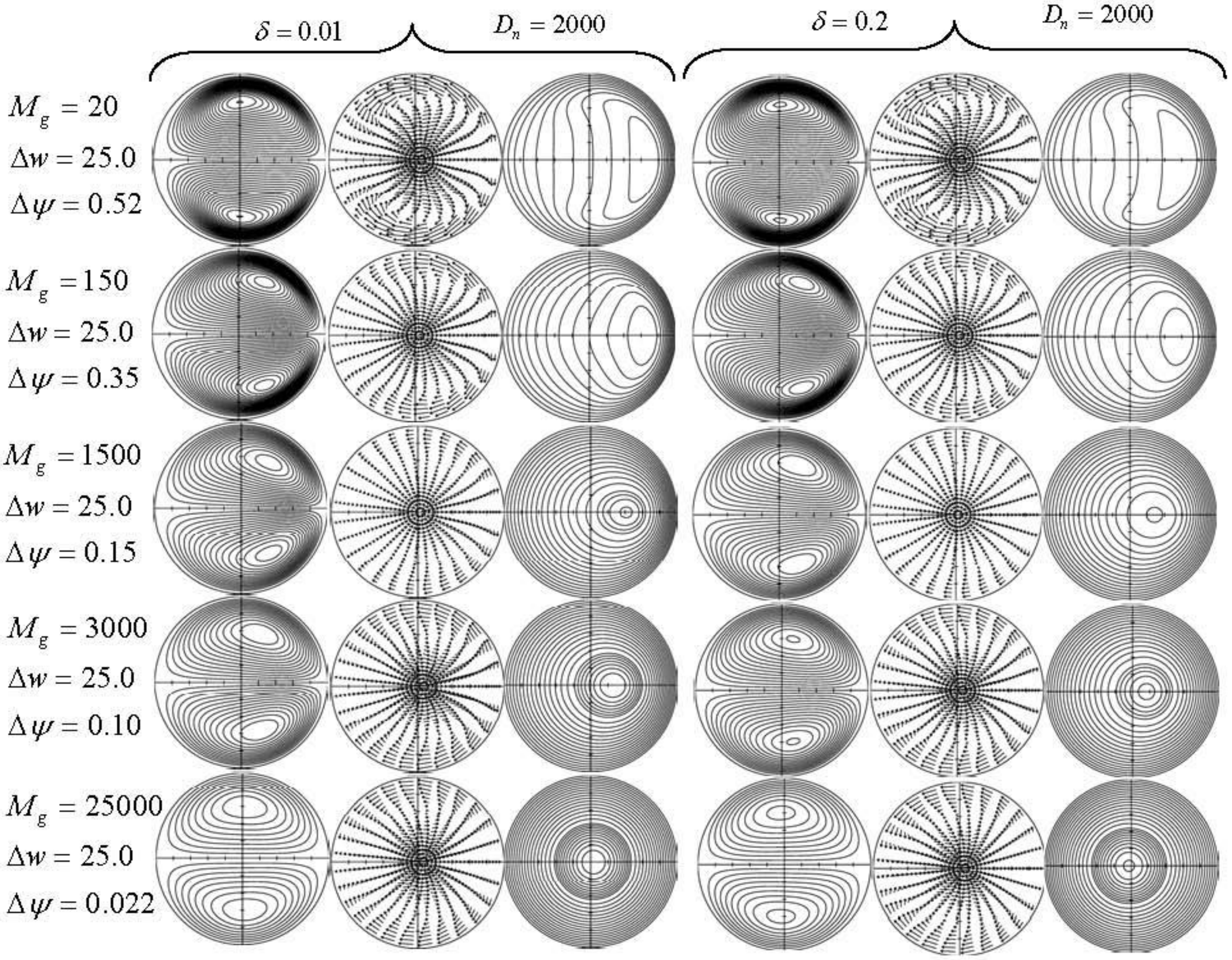

Fig. 5. The secondary flow, vector plots of the secondary flow and axial flow for different values of magnetic parameter at Dean Number $D_n = 2000$

6. Conclusions

As magnetic parameter as well as magnetic parameter increases there originate a symmetric contour plot of secondary flow and only 2-vortex solution has been found for the secondary flow. The two vortexes are of same strength but rotating in counter clockwise direction. The strength of the vortices is shifted to the outer half from the inner half with the increase of Dean number and curvature. For high magnetic parameter, Dean number and low curvature, the axial flow is shifted towards the centre of the pipe as a result almost all the fluid particles strength are week. And finally due to the combined effect of the Dean number and curvature a ***bracelet*** has been originates from the right corner of the duct and expands at $D_n = 2000$.

Acknowledgements

This work was supported by the Ministry of Science and Technology, People's Republic of Bangladesh.

References

[1] Akiyama, M. and Cheng, K. C. Graetz problem in curved pipe with uniform wall Heat; 1970
[2] Akiyama, M. and Cheng, K. C. Graetz problem in curved pipes with uniform wall Heat flux, *Applied Science Research*, **Vol. 29**, pp. 401-418; 1975
[3] Brewster, D. B., Grosberg, P. and Nissan, A. H. The stability of viscous flow between horizontal concentric cylinders, *Proceeding of Royal Society of London A*, **Vol. 251**, pp. 76-91; 1959

[4] Cheng, K. C., Lin, R. and Ou, J. W. Graetz problem in curved square channels, *Trans. ASME Journal of heat transfer*, **Vol. 97**, pp. 244-248; 1975

[5] C. C. Chang and T. S. Lundgren, Z, Angew. Math. Phys. 12, 100; 1961

[6] Daskopoulos, P. and Lenhoff, A. M. Flow in curved ducts: bifurcation structure for stationary ducts, *Journal of Fluid Mechanics*, **Vol. 203**, pp. 125-148; 1989

[7] Dean, W. R. Note on the motion of fluid in a curved pipe, *Philosophical magazine and Journal of Science*, **Vol. 4(20**), pp. 208-223; 1927

[8] Dennis, S. C. R. and Ng, M. Dual solutions for steady laminar flow through a curved tube, *Quarterly Journal of Mechanics and Applied Mathematics*, **Vol. 35**, pp.305-324; 1982

[9] Gottlieb, D. and Orszag, S. A. Numerical Analysis of Spectral Methods, *Society for Industrial and Applied Mathematics, Philadelphia*; 1977

[10] Ito, H. Theory on laminar flows through curved pipes of elliptic and rectangular cross-section, The report of the institute of high speed Mechanics, Tohoku University, Sendai, Japan, **Vol. 1**, pp. 1-16; 1951

[11] J. A. Shercliff, *J. Fluid Mech.* 1, 644; 1956

[12] J. S. Walker, *J. Fluid Mech.* 167, 199;1986

[13] Masliyah, J. H. On laminar flow in curved semicircular ducts, *Journal of Fluid Mechanics*, **Vol. 99**, pp. 469-479; 1980

[14] Nandakumar, K. and Masliyah, J. H. Swirling flow and heat transfer in coiled and twisted pipes, *Advances in Transport Processes*, **Vol.4**, pp 49-112; 1982

[15] Nandakumar, K., Mees, P. A. J. and Masliyah, J. H. Multiple two-dimensional solutions to the Dean problem in triangular ducts, *Physics of Fluids A*, **Vol. 5 (5)**,pp. 1182-1187; 1993

[16] Reid, W. H. On stability of viscous flow in curved channel, *Proceeding of Royal Society of London A*, **Vol. 244**, 186-198; 1958

[17] R. J. Holroyd and J. S. Walker, *J. Fluid Mech.*84, 47; 1978

[18] Yanase, S., Goto, N. and Yamamoto, K. Dual solutions of the flow through a curved tube, *Fluid Dynamics Research*, **Vol. 5**, pp. 191-201; 1989

[19] Yang, T. and Wang, L. Solution Structure and Stability of Viscous Flow in Curved Square Ducts, *ASME Journal of Fluids Engineering*, **Vol. 123**, pp. 863-868; 2001

Available online at www.sciencedirect.com

SciVerse ScienceDirect

Procedia Engineering 00 (2012) 000–000

Procedia Engineering

www.elsevier.com/locate/procedia

5th BSME International Conference on Thermal Engineering

Wake-flat plate boundary layer interaction at low Reynolds number

Sanchita Amin*, Dipak Kanti Das

Department of Mechanical Engineering, Bangladesh University of Engineering and Technology (BUET), Dhaka-1000, Bangladesh.

Abstract

The present numerical study has been conducted to observe the unsteady boundary layer characteristics on a flat plate induced by a von Karman vortex street wake. This flow situation is an idealization of that occurring on turbomachinery blades where unsteady wakes are generated by the preceding row of blades. In this research, the boundary layer is developed under zero pressure gradient while the vortex street is generated by an elliptic cylinder positioned in the free stream. The minor-major axes ratio of the elliptic cylinder is taken as 0.6 with an angle of attack 0^0. The investigation covers a Reynolds number range up to 1000 based on the focal distance of the elliptic cylinder and free stream velocity. The time dependent, two dimensional flow is simulated numerically using finite element formulation. The development of the flow field up to certain time period is considered. Instantaneous streamlines of the disturbed flow field, instantaneous velocity field, boundary layer integral parameters, and skin friction on different streamwise locations on the plate are presented for different Reynolds numbers. The wake vortices strongly affect the boundary layer over the flat plate.

Keywords: Wake; Boundary layer; Separation bubble.

Nomenclature

a	Semi-major axis length of the elliptic cylinder (m)
b	Semi-minor axis length of the elliptic cylinder (m)
c	Focal distance of the ellipse (m)
C_{fx}	Skin friction Co-efficient on different on plate axial location
H	Shape factor (δ/θ)
H_{av}	Average shape factor
Re_{2c}	Reynolds number based on cylinder distance between the foci, $\rho U(2c)/\mu$
t	Time (s)
U	Free stream velocity (m/s)
u	x-velocity component (m/s)
v	y-velocity component (m/s)
X	Dimensional Co-ordinate(m)
Y	Dimensional Co-ordinate(m)
x_c	Axial distance between cylinder and plate leading edge, (m)
y_c	Vertical distance between cylinder and plate leading edge, (m)
x_p	Streamwise location on the plate from plate leading edge, (m)
Greek symbols	
α	Angle of attack of the elliptic cylinder (^{0}, deg)
μ	Kinematic viscosity of air ($N.s/m^2$)
ρ	Fluid density (kg/m^3)
τ	Global Dimensionless time, Ut/c

---

* Corresponding author. Tel.: +88-01816472959; fax: +88-02-8613046.
E-mail address: sanchita@me.buet.ac.bd

1. Introduction

Unsteady boundary layers are encountered in many engineering applications, and they are often transitional, especially in turbomachines and aeronautics, where the boundary layer transition originates from boundary layer interaction with transverse and longitudinal vortices. In turbines and compressors, the relative motion of adjacent blade rows gives rise to a variety of unsteady flow interactions. The blades in any moving blade row are continually passing through the individual wakes of the upstream blade rows. Similarly, the blades in the fixed blade rows are being struck by the wakes of the upstream moving blades. The wakes exhibit a defect in mean velocity and a superimposed high level of turbulence intensity. These conditions have a significant influence upon boundary layer transition process. The boundary layer, laminar or turbulent, strongly influences skin friction, and therefore, drags losses. Also the transition region of boundary layer affects the machine performance, the flow losses and especially the heat transfer to turbine blades. Hence, good understanding of the unsteady boundary layer behavior is important for improving the design of turbomachines.

Engineering applications often involve flows over complex bodies like wings, submarines, missiles, and rotor blades, which depends on parameters such as thickness ratio and angle-of-attack and these parameters greatly influence the nature of separation and the wake structure. Elliptic cylinders, which are more general geometrical configurations than the canonical circular cylinder, can provide a richer flow behavior characteristic of typical engineering flow configurations and significantly augment the understanding of wake flows.

Badr et al. [1], solved numerically the problem of uniform flow past an impulsively started inclined elliptic cylinder for Reynolds numbers ranging from 900 to 5000 and for the range of angle of attack between 0 and 90°. The results reveal an unusual phenomenon of negative lift occurring shortly after the start of motion depending upon the value of the angle of inclination and are consistent with the experimental findings of Taneda [2, 3]. Taneda [2] studied the relationship between the time dependent lift and flow pattern for the case of an impulsively started elliptic cylinder (AR = 2.1) at angles of incidence of 20^0 and 45^0 at Reynolds numbers 3500 and 6000 respectively. He reported very high initial lift values and a gradual downward movement of the rear stagnation point. In addition, it was pointed out that lift takes negative values in a small time interval shortly after the impulsive start in the case of angle of attack 20^0 unlike the case of angle of attack 45^0.

A study had been made of the process of laminar to turbulent transition induced by the von Karman vortex street, in the boundary layer on a flat plate by Kyriakides et al. [4]**.** It was established that, the onset of the strong von karman wake induced transition process was a function of the free stream velocity, the position of the cylinder with respect to the plate, the cylinder diameter, the drag coefficient and the minimum velocity in the developing wake at the streamwise position of the onset of the boundary layer transition. It was also established that, in the case of weak wake-boundary layer interaction, the boundary layer transition process was accelerated by the overall free stream turbulence increase due to the wake of the cylinder. From the experimental observations they also developed a correlation which can predict the onset of transition under strong wake-boundary layer interaction. Liu and Rodi [5] investigated in detail the development of boundary layer along a flat plate under the influence of periodically passing wakes by hot-wire measurements. When wakes passed over the plate, the boundary layer was found to be turbulent quite early underneath the free-stream disturbances due to wakes, while it remained initially laminar. The turbulent boundary layer stripes underneath the disturbed free-stream traveled downstream and grew together so that the embedded laminar regions disappear and the boundary layer became fully turbulent.

Savill and Zhou [6] made an extensive study at low Reynolds numbers of various types of simple interactions, using flow visualization. They studied, what they called, “slow” or “weak” interactions in which the wake was initially sufficiently far from the boundary layer and was effectively fully developed, before starting to merge with the boundary layer. In contrast to the above type of transition, “fast” or “strong” interactions were also studied. In this type of interaction, the initial vortex street was still present, when the two shear layers merged together. Savill and Zhou concluded that the main parameter governing the growth of the interaction is the level of turbulence in the interaction region. Wu et al. [7] numerically simulated the interaction between an initially laminar boundary layer developing spatially on a flat plate and wakes. They found that the inlet wake disturbances inside the boundary layer evolved rapidly into longitudinal puffs during an initial receptivity phase. In the absence of strong forcing from free-stream vortices, these structures exhibited streamwise elongation with gradual decay in amplitude. Selective intensification of the puffs occurred when certain types of turbulent eddies from free-stream wake interact with the boundary layer through a localized instability. Breakdown of the puffs into young turbulent spots was preceded by a wavy motion in the velocity field outer part of the boundary layer.

Turbulent wakes swept across a flat plate boundary layer i.e. the phenomenon of wake-induced bypass transition was simulated by Wu and Durbin [8]. Benchmark data from a direct numerical simulation of this process were presented and compared to Reynold-averaged predictions. The data were averaged skin-friction and mean velocities. Choi and Lee [9] experimentally investigated the flow characteristics around an elliptic cylinder with an axis ratio of AR=2 located near a flat plate. The elliptic cylinder was embedded in a turbulent boundary layer whose thickness was larger than the cylinder height. The Reynolds number based on the height of the cylinder cross-section was 14000. The wake velocity profiles behind the cylinder were measured using hot-wire anemometry. In the near-wake region, the vortices were shed regularly only when the gap ratio was greater than the critical value of G/B=0.4. The critical gap ratio was larger than that of a circular cylinder.

As the gap ratio increased, the drag co-efficient of the cylinder itself increased, but lift co-efficient decreases.

In the current research, numerical simulations have been performed to study the interaction between the unsteady wake of an upstream element and the boundary layer over a downstream element. To study such flows in a simpler setting, a model problem is considered, illustrated in Fig. 1, which consists of an elliptic cylinder positioned over a flat plate. Although there have been a number of experimental investigations on such flows, numerical investigations is limited due to its complexity in grid generation. Also wake induced from the elliptic cylinder got less attention in this regard. A numerical study of this type of flow on laminar Reynolds number ranges will be considered in this research work.

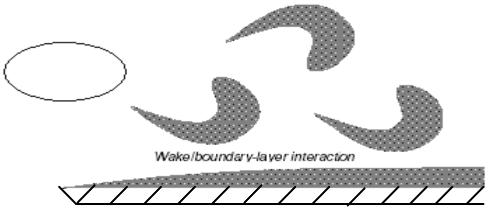

Fig. 1. Interaction in a simplified geometry

2. Mathematical modeling

An elliptic cylinder having major and minor axis of lengths 2a and 2b respectively and axis ratio (AR = b/a) of 0.6, in an otherwise uniform flow, U can be modeled by unsteady 2-D Navier-Stokes equation neglecting body forces,

$$\rho \frac{\partial V}{\partial t} + \rho\,(V.\nabla)V = -\nabla P + \mu \nabla^2 V \tag{1}$$

Dimensionless Analysis

The dimensionless quantities are,

$$V' = \frac{V}{U}\ ,\ x' = \frac{x}{c}\ ,\ y' = \frac{y}{c}\ ,\ P' = \frac{P}{\rho U^2}\ ,\ t' = \frac{U t}{c}\ \text{ also, } \nabla = \frac{1}{c}\nabla' \text{ and } \nabla^2 = \frac{1}{c^2}\nabla'^{\,2}$$

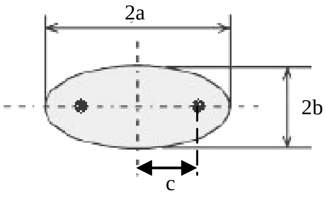

where, c stands for the focal distance of the ellipse defined by, $c = \sqrt{a^2 - b^2}$.
Now equation (3) in dimensionless form,

$$\rho \frac{\partial V' U}{\partial\left(\frac{t' c}{U}\right)} + \rho\left(V' U.\frac{1}{c}\nabla'\right)V' U = -\frac{1}{c}\nabla' P' \rho U^2 + \mu \frac{1}{c^2}\nabla^2 V' U$$

$$\text{or,}\quad \frac{\partial V'}{\partial t'} + \left(V'.\nabla'\right)V' = -\nabla' P' + \frac{2}{\mathrm{Re}_{2c}}\nabla'^{\,2} V' \tag{2}$$

where $\mathrm{Re}_{2c} = \frac{\rho U(2c)}{\mu}$. Equation (2) is the dimensionless form of 2-D unsteady Navier-Stokes equation. And dimensionless form of conservation of mass,

$$\nabla'.V' = 0 \tag{3}$$

Equation (3) along with the compressibility constraint, equation (2) will be used for the present numerical computation.

In the present computation dimensionless time is considered as $\tau = \frac{Ut}{c}$ which was used by Badr et al. [1] where they used the vorticity/stream function formulation of unsteady 2-D Navier-Stokes equation.

3. Boundary conditions

The computational Domain subjected to initial condition, $(u,v)\ \big|_{t=0} = (U,V)$

The boundary conditions to be considered are as follows:

a. An inflow boundary condition is applied at the left boundary: $\boldsymbol{V}$ = U i.e. $u = U$ and $v = 0$
b. Slip boundary condition is applied at the lower left boundary: $\partial u / \partial y = 0$, $v = 0$

c. No-slip velocity condition for all velocity components on all solid walls. So,
   i. On the plate surface, $\boldsymbol{V} = 0$ i.e. $u = v = 0$.
   ii. On the surface of the cylinder, also $\boldsymbol{V} = 0$ i.e. $u = v = 0$.

d. An open boundary condition is applied at the upper boundary of the domain.

$$(-p\mathbf{I} + \mu(\nabla \mathbf{V} + (\nabla \mathbf{V})^{T}))\,\mathbf{n} = 0$$

e. An outflow boundary condition is applied at the right boundary: $\mu(\nabla \mathbf{V} + (\nabla \mathbf{V})^{T})\,\mathbf{n} = 0$ and $p = p_0$.

This boundary condition specifies vanishing viscous stress along with a pressure condition for incompressible flow configuration. This boundary condition is physically equivalent to a boundary that is exiting into a large container. It is numerically stable and admits total control of the pressure level along the entire boundary.

4. Computational details

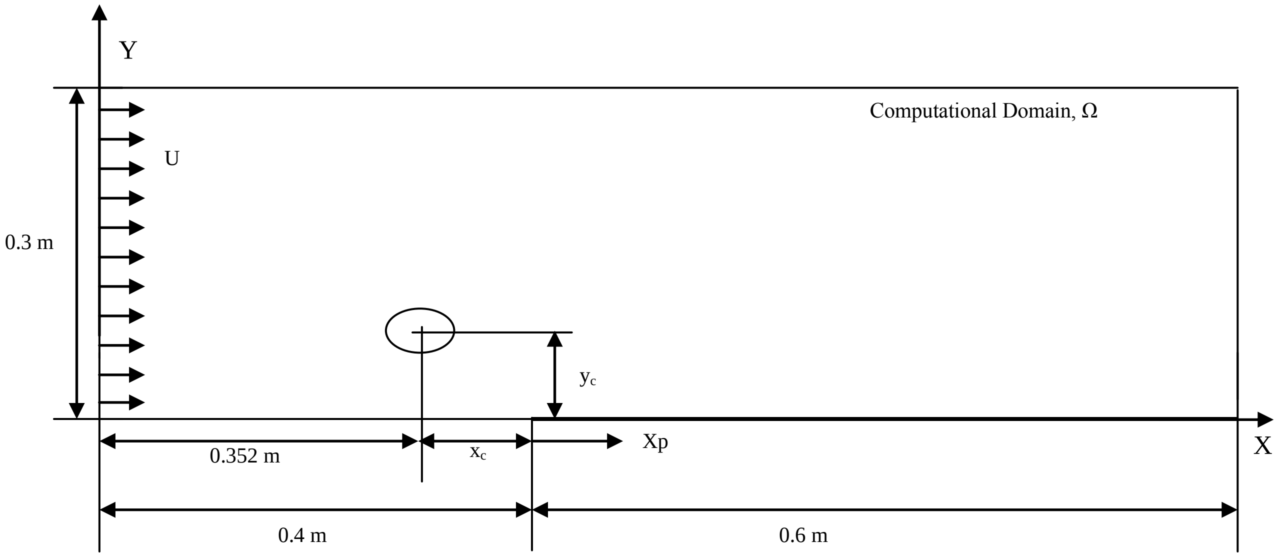

Fig. 2. Scheme of the computational domain (not to scale)

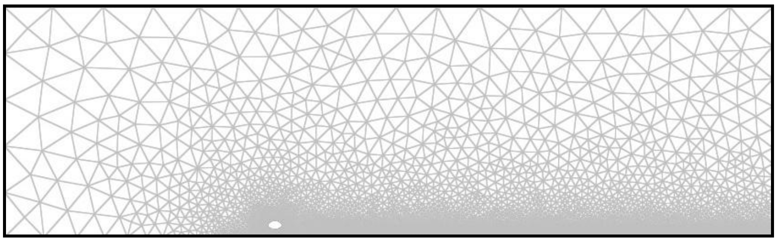

Fig. 3. The mesh mode for the present numerical computation.

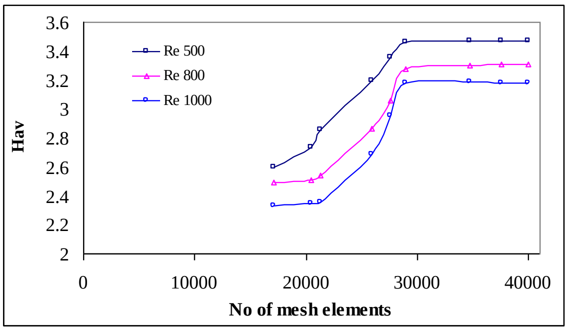

Fig .4. Grid Independency test for $x_c/2c = -3$ $y_c/2c = 1$, at Xp = 400 mm.

Figure 2 shows the computational domain of the present numerical study. As numerical results greatly depend on the mesh generation, a grid sensitivity test has been carried out to find the optimum element number. From the results of the grid sensitivity tests (shown in Fig. 4), around 29,000 elements mesh has been selected to predict the results based on accuracy and time. Figure 3 shows the mesh mode of this numerical study. Special attention has been given for mesh generation on the cylinder surface and on the plate surface.

The present numerical study focuses on the flow field where the flat plate boundary layer is interrupted by the wake boundary layer, not on the flow field around the elliptic cylinder. The authors have assumed a 2D model for preliminary study on the physics of wake-flat plate boundary layer interaction, where 3D effect of the wake has not been considered. .

5. Results and discussion

The "Results and discussion" part has been divided into two sections: the first section deals with the results obtained from the elliptic cylinder in uniform flow, comparing with the results of the published data available in literature (i.e. code validation) and in the second section, results of the present numerical study of the 2D boundary layer development on the surface of a flat plate under the influence of passing wake vortices induced from an elliptic cylinder has been presented. The Reynolds number, Re_{2c} considered here are 500, 800, and 1000 and the distance between the center of the cylinder and the plate leading edge as $x_c/2c = -3$, $y_c/2c = 1$.

The method of the solution and the accuracy of the numerical scheme of elliptic cylinder in uniform flow is verified for Reynolds number $Re_{2c} = 1000$, the angle of attack of $\alpha = 0^0$ and cylinder axis ratio AR = 0.6. In order to verify the present numerical scheme used in this work, the initial flow for the problem of flow field of the elliptic cylinder only is considered.

Figure 5 shows that at the start of motion, the wake cavity behind the cylinder (at $\alpha = 0^0$) contains a symmetrical pair of equal and opposite recirculating-flow regions (upper clockwise and lower counter-clockwise vortex pairs) on either side of the wake whose length grows (due to viscous stresses) with the increase of time τ. The drag coefficient of a flow can be split into two parts, one due to frictional forces and the other due to pressure forces. $C_D = C_{DF} + C_{DP}$, C_{DF} and C_{DP} are the friction and pressure components of the drag coefficient. The calculated values of C_{DF}, C_{DP} and C_D for $Re_{2c} = 1000$ and $\alpha = 0^0$, when the flow is symmetric about the major axis are plotted in Fig. 6. The figure shows that the contribution of frictional force to the total drag coefficient C_D is relatively small. The figures (figure 5 and 6) of instantaneous streamline and drag coefficients found in the present problem show a good agreement with the numerical solution of Badr et al. [1].

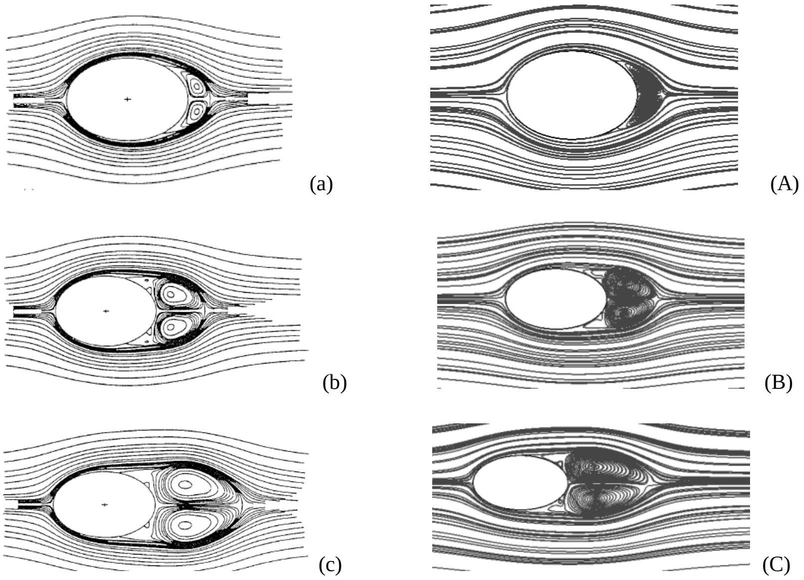

Fig. 5. Comparison of Instantaneous streamlines of the flow for Re_{2c}=1000, and $\alpha = 0^0$: (a,A) $\tau = 2.0$; (b,B) $\tau = 5.0$; (c,C) $\tau = 10.0$. (a-c) Flow visualization by Badr et al. [1] and (A-C) Present Finite Element Computation.

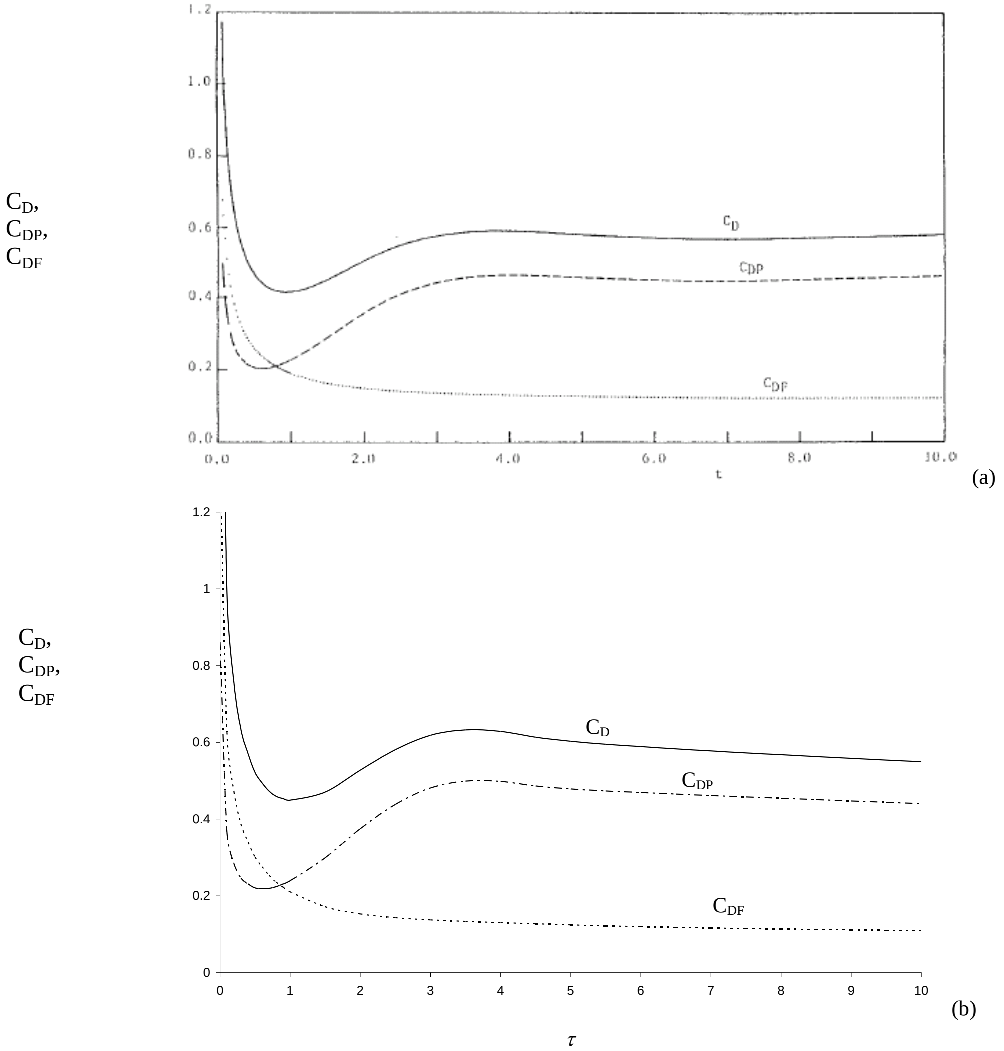

Fig. 6. Variation of the Drag Coefficients C_D, C_{DF}, and C_{DP} with τ at $Re_{2c} = 1000$ and $\alpha = 0^0$. (a) results from Badr, Danis and Kocabiyik, (b) Present Finite Element Computation

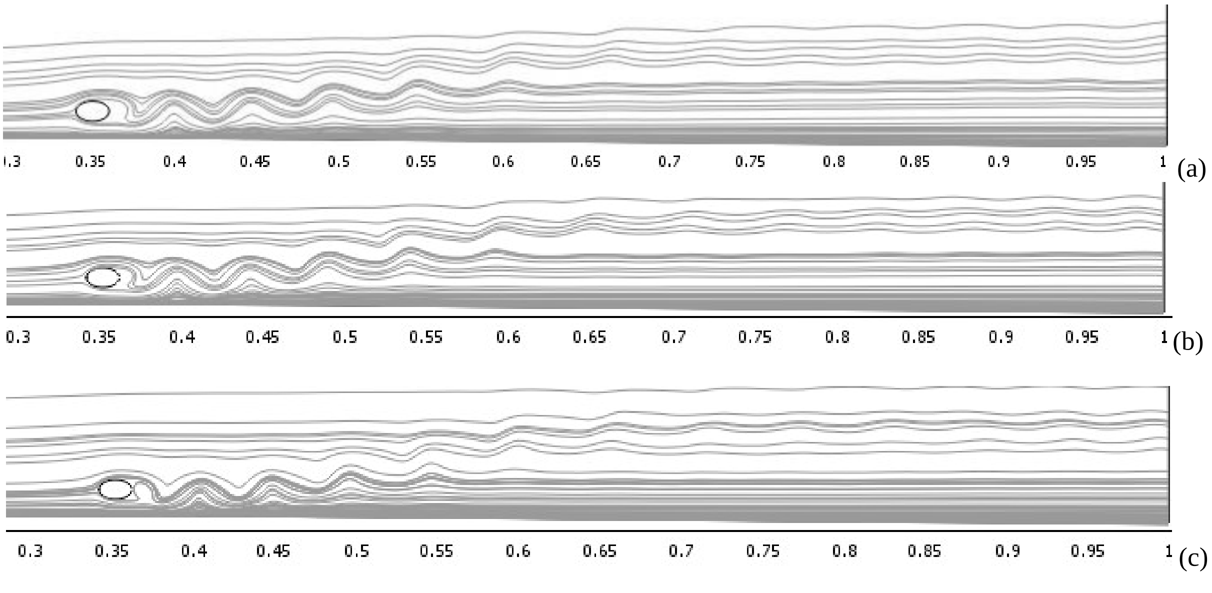

Fig. 7. Instantaneous streamlines on the flow fields at $\tau = 800$ and $x_c/2c = -3$ $y_c/2c = 1$ (a) Re_{2c}=500, (b) Re_{2c}=800 (c) Re_{2c}=1000.

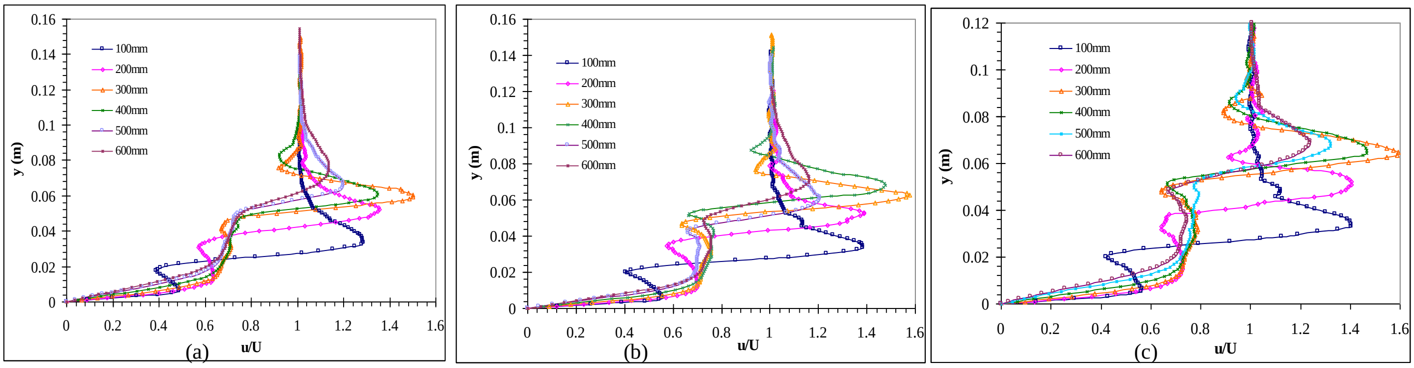

Fig. 8. Instantaneous velocity distribution on different flat plate axial locations for τ = 800, $x_c/2c$ = -3 $y_c/2c$ = 1 (a) Re_{2c}=500, (b) Re_{2c}=800 (c) Re_{2c}=1000.

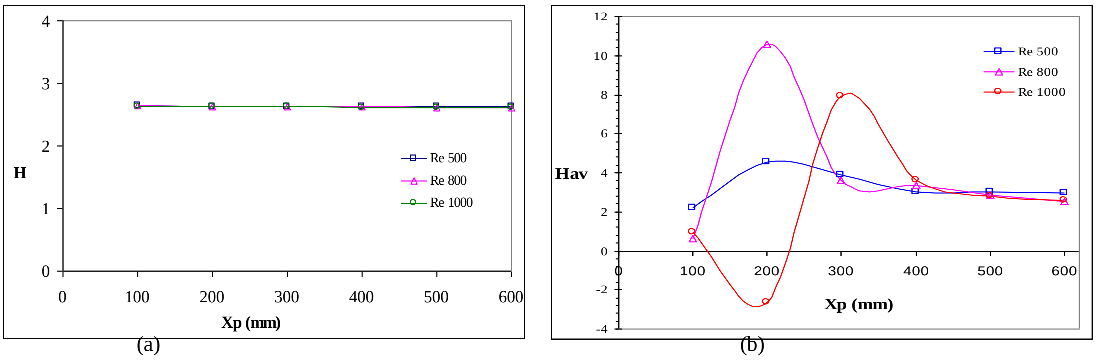

Fig. 9. Average shape factor (H_{av}) variation with plate stream-wise locations for different Reynolds number and for cylinder to plate relative position $x_c/2c$ = -3 $y_c/2c$ = 1, (a) for undisturbed flow and (b) in the presence of elliptic cylinder.

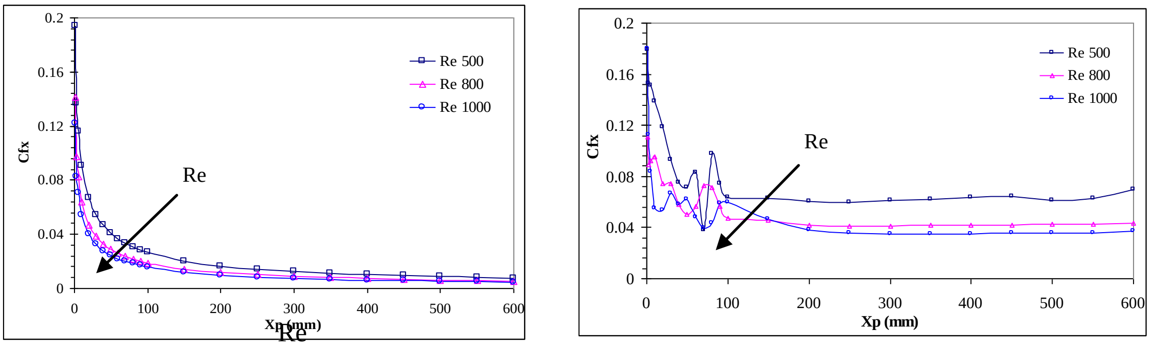

(a) (b)

Fig. 10. Variation of skin friction coefficient (C_f) with different plate location for τ = 800 □-Re_{2c} 500, Δ-Re_{2c} 800, ○-Re_{2c} 1000, (a) undisturbed flow case and (b) in the presence of elliptic cylinder, $x_c/2c$ = -3 $y_c/2c$ = 1.

Figure 7 represent the instantaneous stream lines development of the flow field for the test cases of the present numerical problem. Actually the wake region can be classified into some flow regimes based on the Reynolds number such as laminar steady regime, laminar vortex shedding regime, wake transition regime, shear layer transition regime, asymmetric reattachment regime (critical transition), symmetric reattachment regime (or supercritical regime) etc. From the visualization of the flow field, it can be said that for the three Reynolds numbers used in the present numerical problem, the flow fields were in the laminar vortex shedding regime. As the wake moves downstream, it starts interaction with the boundary layer on the plate by advecting low speed fluid from the wall into the outer region and high speed fluid from the core towards the wall, as rollers of alternating rotation are convected above the boundary layer and so the shape of the streamlines found in the figures are in wavy shape. The interaction procedure of the cylinder wake and the boundary layer of the flat plate can be divided into three stages [10]. In the first stage, the wake and the boundary layer are separated and can be well represented by the usual relationships (i.e. only the wake behaviors behind an elliptic cylinder and the boundary layer on the plate for undisturbed flow individually). The second stage corresponds to the initial merging of the wake and the boundary layer and is the most important and the most complicated in the evolution of the merging flow. Here, the outer part of the wake and the innermost part of the boundary layer are substantially unaffected by the interaction, although the flow in the merging region is completely different from that in the undisturbed flow. In the final stage, the merging flow disappears and the layer gradually reverts to a new thicker boundary layer. The wake spreads outward from the source until its energy is lost, usually by friction or dispersion and becomes weaker. Strong inviscid-viscid interaction takes place in the form of an eruption in the boundary layer and these eruptions and the vortices penetrate into the wake region and weaken the vortex formation in the shear layer. The merging distance depends, of course, on the spreading rate of the wake and on the boundary-layer growth (i.e. on the Reynolds number), as well as on the initial distance between the wake and the solid body. The shape of the body that forms the wake is also affect the merging distance.

An overall picture of the flat plate boundary layer-cylinder wake interaction could be obtained, by studying the velocity profiles. The velocity profiles of all cases, for several streamwise locations on the plate, are presented in Fig. 8 for a particular non-dimensional time τ = 800. The shape of the profiles are largely dependent on the combined effect of Reynolds number, cylinder to plate relative position and the size of the wake, But in general, in every velocity profile, two regions could be identified. The first one is a wake region; it appeared downstream of the cylinder, creating a velocity defect which gradually disappeared with the streamwise distance. The second is the boundary layer region. In this case the velocity distribution, up to the point of interaction, followed the shape of Blasius profile, indicating that the boundary layer is still laminar. As we move from the plate leading edge to the downstream, it is found that the shape of the streamlines are wavy and the velocity profile is not as Blassius because of the effect of the shed vortices to the near wall region. In this region the wake from the cylinder perturbs the boundary layer by advecting low-speed fluid from the wall into outer region and, and high speed fluid from the core towards the wall, as rollers of alternating rotation are convected above the boundary layer. Thus approximately S-shaped velocity profile under the influence of wake vortices is identified. As the wake decays, the advection effect becomes less significant. In the low Reynolds number cases (in the present problem) the flow tends towards a more quiescent state towards the end of the computational domain and the statistics never reach turbulent level. With the increase in Reynolds number, the free stream disturbance level increases due to the inherent increase in vortex street strength.

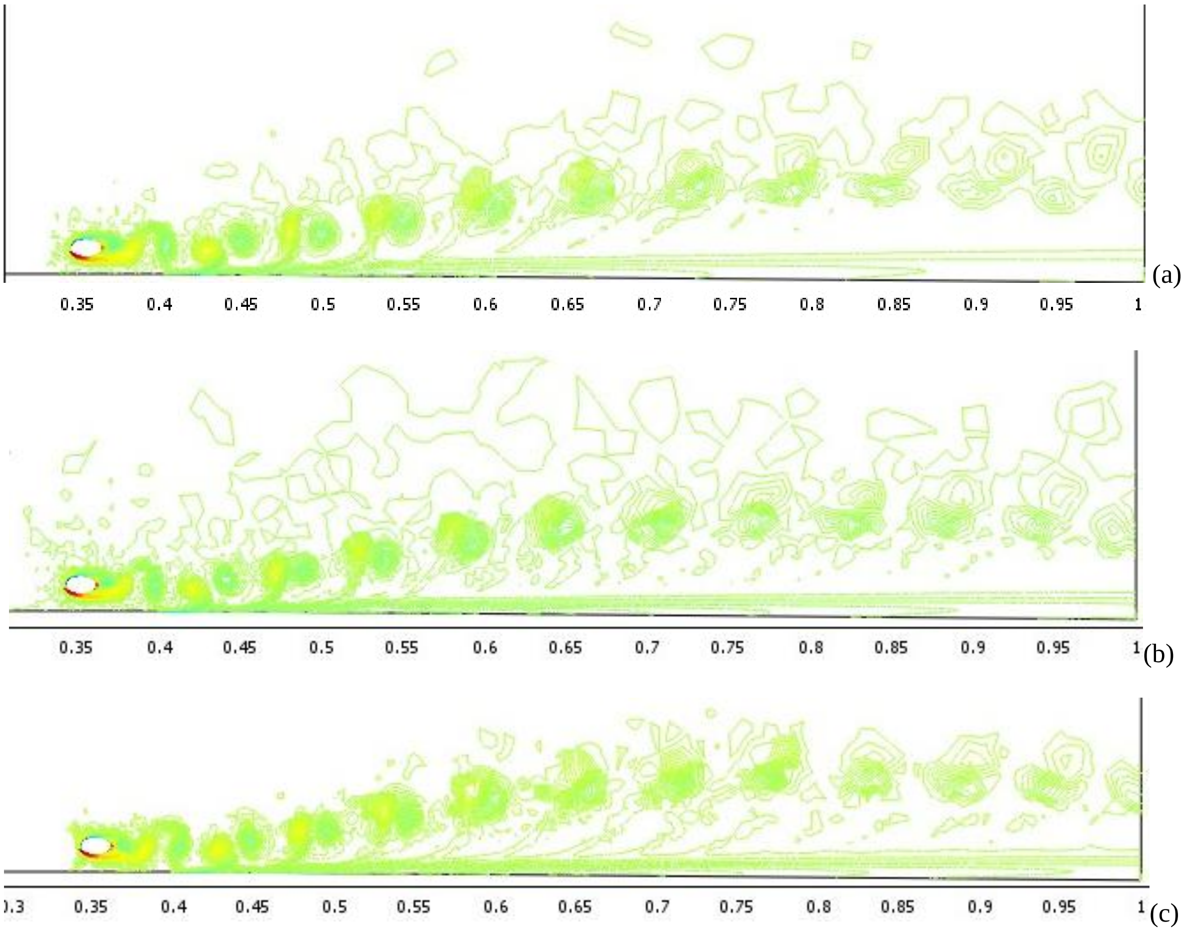

Fig. 11. Instantaneous vorticity contours at τ = 800 and $x_c/2c = -3$ $y_c/2c = 1$, (a) $Re_{2c}=500$, (b) $Re_{2c}=800$ (c) $Re_{2c}=1000$.

For a particular Reynolds number, it is clearly observed that the boundary layer thickness increases with the increase of plate axial location. This is due to, wake vortices widen further downstream and thus the merging of wake vortices with boundary layer occurs in large scale. More wake vorticity elements available in the boundary layer which can interact more with increasing plate axial locations. Thus velocity deficit starts (for wake region) somewhat earlier in upward direction from the plate with increasing the streamwise positions. It can be concluded that if the plate length is much more than 600mm (as in present numerical problem), there may be a region when the velocity profile will follow the Blassius profile due to weak interation of the wake and boundary layer. Figure 11 shows vorticity contours for the interaction of wake shear layer and plate boundary layer for $\tau = 800$.

The boundary layer integral parameter such as shape factor (H), is of particular interest to turbine designer, since they provide an accurate first estimation of the quality of the designed blade. Figure 9 shows the variation of shape factor with the plate axial location for undisturbed and disturbed flow condition. It is clear from fig 9(a) that the shape factor remain same i.e. $H \approx 2.6$ for all the Reynolds number indicating that the flow is laminar. For disturbed flows (Fig. 9(b)), for a particular Reynolds number the trend of graphs shows a fluctuating behaviour but with the increase of plate axial distance, the amplitude of the fluctuations gradually decreases. This behaviour may be due to the fact that there was strong interaction near the plate leading edge where the size of the wake was small but as the wake passes forward i.e. to the downstream of the plate the interaction was weaker and the wake size became larger. With the increase of Reynolds number, the average shape factor decrease.

Figure 10 shows the variation of skin friction with the plate streamwise axial position. For the undisturbed flow case and also for the disturbed cases (with the presence of cylinder wake), it is found that as the axial distance of the plate increases, skin friction decreases for a particular Reynolds number. This trend can be found in literature. For undisturbed flow case, the figure 10(b) slows that, with the increase of Reynolds number, skin friction decreases.

6. Conclusion

Unsteady boundary layer development over a flat plate under the influence of wake vortices induced from an elliptic cylinder is investigated here for different Reynolds number. The interaction between the boundary layer developed over a flat plate and the cylinder wake has been studied from the view-point to visualize the effect of the presence of a cylinder in the laminar boundary layer over a flat surface, where the cylinder controls the laminar boundary layer flow. Two types of boundary layer-wake interaction are obtained from the computations, one is the strong wake-boundary layer interaction and another is the weak wake-boundary layer. The intensity of interaction greatly depends on plate streamwise location and the Reynolds number. The higher the Reynolds number, the more rapidly the wake loses its coherence, and the more unstable the boundary layer is to perturbation. Despite the difference in the Reynolds number, the mechanism of interaction is the same for all the cases.

7. References

[1] Badr H.M., Dennis S.C.R. and Kocabiyik S., (2001), Numerical simulation of the unsteady flow over an elliptic cylinder at different orientations, International Journal for Numerical Methods in Fluids; 37, p. 905-931.

[2] Taneda S., (1972), The development of the lift of an impulsively started elliptic cylinder at incidence, Journal of the Physics Society of Japan, vol. 33, pp. 1706–1711.

[3] Taneda S., (1977), 'Visual study of unsteady separated flows around bodies', Progress in Aerospace Science, 17, p. 287-348.

[4] Kyriakides, N. K., Kastrinakis, E.G., Nychas, S.G., Goulas, A., (1996), Boundary layer transition induced by a von karman vortex street wake, IMechE, PartG: Journal of Aerospace Engineering, 210**,** p. 167-179.

[5] Liu, X., and Rodi, W., (1991), Experiments on transitional boundary layers with wake induced unsteadiness, J.Fluid Mech., 231, p. 229-256.

[6] Savill, A., and Zhou, M., (1983), Wake/boundary layer and wake/wake interactions-smoke flow visualization and modeling, Proceedings of the second Asian Congress of Fluid Mechanics, p. 743-754.

[7] Wu, X., Jacobs, R.G., Hunt, J.C.R. and Durbin, P., (1999), Simulation of boundary layer transition induced by periodically passing wakes, J. Fluid Mech., 398**,** p. 109-153.

[8] Wu, X. and Durbin, P.A., (2000), Boundary layer transition induced by periodic wakes, Journal of Turbomachinery, 122**,** p. 442- 449.

[9] Choi, J.-H. and Lee, S.-J.,(2000), Ground effect of flow around an elliptic cylinder in a turbulent boundary layer, Journal of Fluids and Structures, 14**,** p. 697-709.

[10] Squire, L. C., (1989), Interactions between wakes and boundary layers, Prog. Aerospace Sci., 26, p. 261-288.

Available online at www.sciencedirect.com

SciVerse ScienceDirect

Procedia Engineering 00 (2012) 000–000

Procedia Engineering

www.elsevier.com/locate/procedia

5th BSME International Conference on Thermal Engineering

Study the Effect of Seepage on the Higher Order Moment to Extract Information About the Turbulent Flow Structure in an Open Channel Flow

Md Abdullah Al Faruque[a],*, Ram Balachandar[b]

[a]*Assistant Professor, Civil Engineering Technology, Rochester Institute of Technology, 78 Lomb Memorial Drive, Rochester, NY 14623, USA*
[b]*Professor, Faculty of Engineering, University of Windsor, 401 Sunset Ave., Windsor, ON, Canada N9B 3P4*

Abstract

An experimental study was carried out to focus the effect of introduction seepage on different turbulent characteristics for an open channel flow. Test results with both suction and injection is presented and discussed to understand the extent of influence of seepage in the depth-wise direction. Particular attention was given on mean velocity, turbulence intensity, Reynolds shear stress, shear stress correlation, higher order moments and quadrant analysis. Two different Reynolds numbers (R_e = 31000 and 47500) were used for each test condition. Reynolds numbers were chosen in order to keep flow condition as sub-critical (i.e. Froude numbers less than unity). The results from the analysis show that the effect of seepage on different turbulent characteristics is not restricted to the near-bed region but can be seen for most of the flow depth. Effect of injection on different turbulent characteristics is more evident with the lower flow rate, however the effect of suction seems to be independent of the flow rates. Results from the analysis of turbulent bursting events show clearly visible effect of seepage well beyond the near-bed region.

Keywords: Seepage; Injection; Suction; Open channel flow; turbulence; Higher order moment.

Nomenclature

d	nominal flow depth (mm)
b	width of the flume (mm)
y	vertical distance from the test bed (mm)
$\overline{u^3}$	streamwise turbulent transport of kinetic energy $\overline{u^2}$
$\overline{v^3}$	vertical turbulent transport of kinetic energy $\overline{v^2}$
D_u	Turbulence diffusion in the longitudinal direction
$(\overline{v^2u})$	Turbulence diffusion in the longitudinal direction
D_v	Turbulence diffusion in the vertical direction
$(\overline{u^2v})$	Turbulence diffusion in the vertical direction
U_e	maximum mean velocity
R_e	Reynolds number

---

* Corresponding author. Tel.: 1-585-475-6664; fax: 1-585-475-7964.
E-mail address: aafite@rit.edu

1. Introduction

Natural channels, rivers, and streams have beds formed by earthen permeable materials and experience seepage flow through boundaries due to the difference between water levels in the channel and the adjoining ground-water levels. Seepage flow through a channel can be in the form of 'suction' or 'injection'. If the free water surface in the channel is higher than the adjoining ground-water level, seepage flow occurs through a channel bed and is called 'suction'. Whereas, if the free water surface in the channel is lower than the adjoining ground-water level, seepage flow occurs into the channel and is called 'injection'. Seepage flow can significantly alter the hydrodynamic behaviour of the channel flow as well as its sediment transport characteristics. It has been noted that the hydrodynamic characteristics of a channel flow can be significantly altered by seepage flow [1]. Although in most cases the magnitude of seepage flow is much less in comparison to the main flow, in certain cases where the inflow seepage (injection) from the channel bed can be large enough to produce a 'quick' condition in the channel bed or the outflow seepage (suction) from the channel bed can be large enough to cause a loss of water of as high as 45% of the water supplied at the upstream of a channel [2]. In comparison with the number of studies on the turbulent flows over impervious smooth and rough boundaries, little is known about the interaction of the pervious bed and the turbulent flow.

The permeable boundary enables mass and momentum transfer across the interface between the fluid and porous media. The interaction between turbulent flow and a permeable boundary may result in changes in the structural features of the flow, such as velocity profile, turbulent intensity and boundary shear stress, as compared with those in relation to an impermeable boundary. Mass and momentum transfer across the interface between the fluid and porous media should be accounted for in addition to those in relation to an impermeable boundary. The variable intensity of seepage flow may cause variation in flow properties. The flow that moves across the porous bed interacts in a complex manner with the flow above. Porous bed can work as a sink or source for harmful toxicants and fine sediments.

[3] reviewed the effect of seepage on the channel boundary layer. [3] observed a reduction in the sublayer thickness due to suction. [3] pointed out that the suction effectively increases the hydrodynamic roughness. [3] also noted that in the presence of suction, there is a decrease in turbulence level, which eventually leads to lesser momentum exchange between fluid particles. This analysis contradicts recent observations that roughness increases turbulence levels in the flow [4-5]. In the presence of injection, [4-5] observed an increase in sublayer thickness and noted an increase in turbulence level, which eventually leads to a greater momentum exchange between fluid particles. [4-5] noted that turbulence fluctuations were more intense for injection than for suction or without seepage.

[6] found that the injection increases turbulence along the interface and thought that the fluid shear and particle to particle momentum transfer between the main and seepage flow is responsible for this increase of turbulence. [7] also noted that along the seepage zone, the turbulent intensities increase significantly in the near-bed region due to injection.

Seepage can alter the flow boundary conditions and eventually affect sediment transport and can change scour phenomenon. Excess scour can cause problem for structural stability of bridges or can undesirably expose the water intake. Whereas, excess sediment deposition can cause severe navigational problem and may need extensive dredging work to keep the flowing of goods through waterways uninterrupted.

2. Experimental setup

Experiments were carried out in a 9-m long rectangular open channel flume (cross-section 1100 mm x 920 mm). The nominal flow depth (d) in the measurement region was 100 mm, resulting in a width-to-depth ratio (b/d) of approximately 11. This value of the aspect ratio is considered to be large enough to minimize the effect of secondary currents and the flow can be considered to be nominally two-dimensional [8]. The bottom slope of the flume was adjustable and for this study, it was kept horizontal and two constant discharges of 720 GPM (Gallon per minute) and 450 GPM (Gallon per minute) were used.

The zone subjected to suction or injection is 2.4 m long, 200-mm deep and spans the entire width of flume. Several variations of the seepage module were considered with the objective of attaining uniform seepage velocity over the entire zone. In the final design, fifteen identical perforated pipes were used to supply water into the flow field (injection) or drain out of the flow field (suction) uniformly. The perforation diameter of the pipe varied from ¾ inch to ⅜ inch. The maximum perforation diameter is at the center of the seepage module and reduced to minimum at the ends of the seepage module. Outside the seepage module, all these fifteen perforated pipes were connected to a common feeder pipe and regulated with a valve. Two separate identical pumps with control valves were used to maintain the flow rate for suction/injection, which was monitored using a flow meter. The sand was placed on top of a filter net, which in turns, overlays a perforated plate. The use of filter net prevents the bed particles from falling down. Water is allowed to seep through the perforated plate, filter net and sand layer to ensure uniform seepage flow within the granular materials. All the measurements were conducted along the centreline of the channel to minimize secondary flow effects and the velocity measurements were conducted in the middle of the seepage module.

A commercial two-component fibre-optic LDA system (Dantec Inc.) powered by a 300-mW Argon-Ion laser was used for the velocity measurements. The optical elements include a Bragg cell, a 500-mm focusing lens and the beam spacing was 38 mm. 10,000 validated samples were acquired at each measurement location. The configuration of the present two-component LDA system would not permit measurements very close to the wall, while one-component (streamwise velocity) measurements were made over the entire depth.

3. Results and discussion

The distribution of velocity triple products $\overline{u^3}$ and $\overline{v^3}$, normalized by maximum mean velocity, which provide valuable information about turbulence flow structures, are shown in Figure 1. One can define $\overline{u^3}$ and $\overline{v^3}$ as the streamwise and vertical turbulent transport of kinetic energy $\overline{u^2}$ and $\overline{v^2}$ respectively. Due to physical obstruction of second component of the laser beam by the sand bed, only variation of $\overline{u^3}$ can be seen for the locations close to the bed (y < 0.15d). As one can note from Figure 1a that $\overline{u^3}$ is positive close to the bed for all flow conditions. Moving farther from bed, a rapid decrease in the value of $\overline{u^3}$ was observed, and $\overline{u^3}$ becomes negative at around y ~ 0.04d for no seepage condition and stays negative for the remainder of the depth. [9] also observed $\overline{u^3}$ to be negative through most of the depth and indicated that the sweep event is significant only near the bed, whereas the ejection events are prevalent through most of the boundary layer. With the introduction of injection, the value of $\overline{u^3}$ becomes negative at locations farther away from the wall (y ≈ 0.1d ~ 0.2d) in comparison to the no seepage condition. The variation of $\overline{u^3}$ in the negative territory is very mild, reaching a local maximum negative value at around y ~ 0.3d for no seepage condition followed by y ~ 0.4d with injection. The value of $\overline{u^3}$ increases beyond this and reaches a near-zero value at y ~ 0.85d for no seepage. With injection, the magnitude of $\overline{u^3}$ tends to remain non-zero even close to the free surface. In the region of negative $\overline{u^3}$, one can note that for y < 0.4d, injection reduces the absolute value of $\overline{u^3}$ and increases the absolute value of $\overline{u^3}$ beyond this. Injection also nominally increases the maximum positive value of $\overline{u^3}$ at locations very close to the bed. The variation of $\overline{v^3}$ is found to be positive throughout the depth for all flow conditions (Figure 1b). Similar observation of positive $\overline{u^3}$ near the bed and positive $\overline{v^3}$ throughout the depth was also made by [5]. A change in the sign of $\overline{u^3}$ is an indication of change in turbulent events. Much higher positive value of $\overline{u^3}$ near the bed is a sign of strong sweep events and injection has a very nominal effect on the near-bed turbulent activity. Negative value of $\overline{u^3}$ and the positive value of $\overline{v^3}$ indicate a slower moving fluid parcel with an upward transport of u momentum representing an ejection type motion and can be seen throughout the depth with the exception of the near-bed location. The near-zero value of $\overline{u^3}$ at y < 0.2d is a cancellation effect of sweep and ejection type events. Farther from the wall, the strength of ejection events increase with increasing negative value of $\overline{u^3}$ and increasing positive value of $\overline{v^3}$. Rapidly diminishing values of both $\overline{u^3}$ and $\overline{v^3}$ in the outer layer is an indication of reducing turbulent bursts and approach to a non-turbulent zone close to the free surface. The variation of $\overline{u^3}$ and $\overline{v^3}$ for higher flow rates are more or less similar to the lower flow rate except the increased magnitude of $\overline{u^3}$ and reduced magnitude of $\overline{v^3}$ with effect of injection is less than that noted for the lower flow rate. Another significant difference is about non-zero value of $\overline{u^3}$ near free surface indicating weakening ejection events. The variation of normalized velocity triple products $\overline{u^3}$ and $\overline{v^3}$ for lower flow rate with the introduction of suction is shown in Figure 2. The overall variation of both triple products is very similar to injection. However, the location where $\overline{u^3}$ changes sign moves closer to the bed with the introduction of suction narrowing the zone of strong sweep events.

Turbulence diffusion in the longitudinal direction D_u ($\overline{v^2u}$) and in the vertical direction D_v ($\overline{u^2v}$), normalized by maximum mean velocity is shown in Figure 3. As seen in Figure 3, the values of D_u and D_v are always negative and positive, respectively, for the present range of measurements. One can note from Figure 3a that as value of D_v increases farther from bed and attain its maximum value at around y ~ 0.4d indicates intense turbulent diffusion in upward direction. One can also note that D_v decays in the outer region (y > 0.4d) and become negligible near the free surface. Although there are no distinct effect of injection for the variation of D_v upto depth of y ~ 0.45d but injection reduces the decaying rate of D_v in the outer region in comparison to no seepage condition. As shown in Figure 3b, D_u tends to be more negative indicates streamwise deceleration with increasing distance from near bed region and attains minimum at around the same location (y ~ 0.4d) of maximum D_v. Value of D_u increases beyond this towards zero near the free surface. Increased value of D_u observed in the outer region (y > 0.4d) in comparison to no seepage condition with the introduction of injection. The distribution of D_v and D_u is found to be very similar for the higher flow rate (not shown here for brevity).

Figure 4 shows the variation of D_u and D_v with the introduction of suction for lower flow rate. The effect of suction is clearly opposite to that noticed by injection. The trend of the variation of D_u and D_v for y < 0.2d seen in Figures 3 and 4 could be an indication of change in sign in the region very close to the wall, not covered by the present range of measurement. The change of sign is a reflection of the change of dominance of sweep/ejection events.

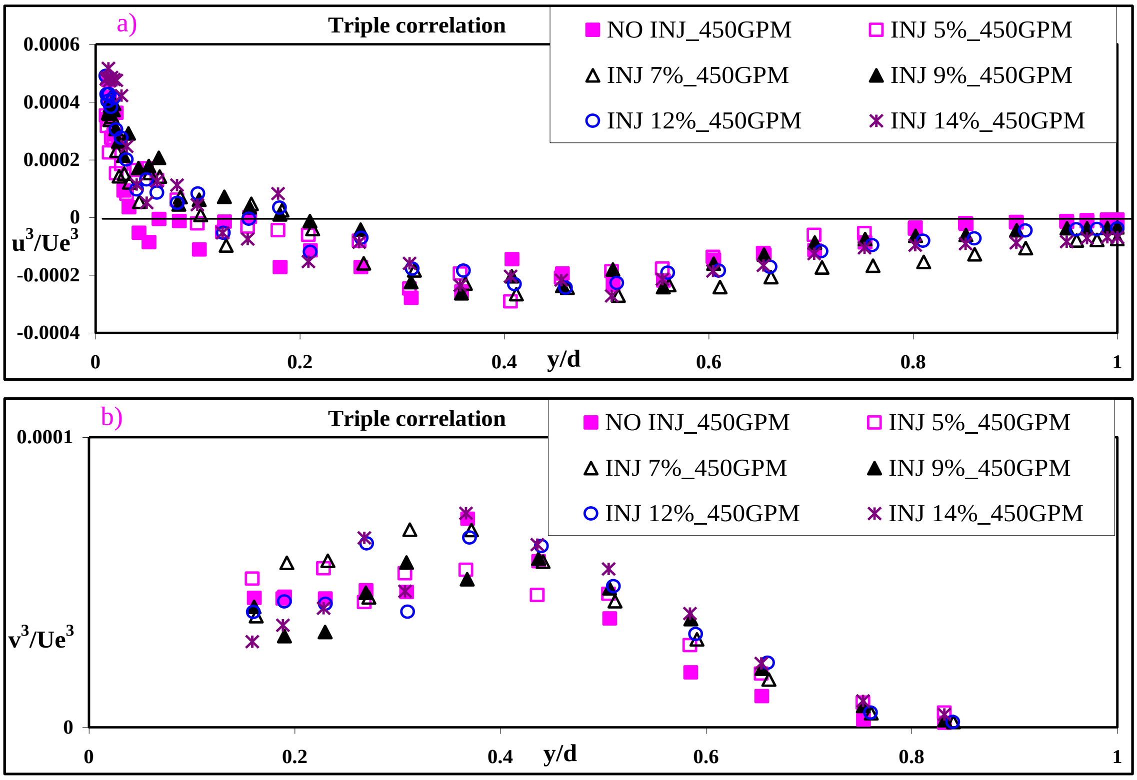

Figure 1: Distribution of different velocity triple product, a) u^3: Injection_450GPM, b) v^3: Injection_450GPM.

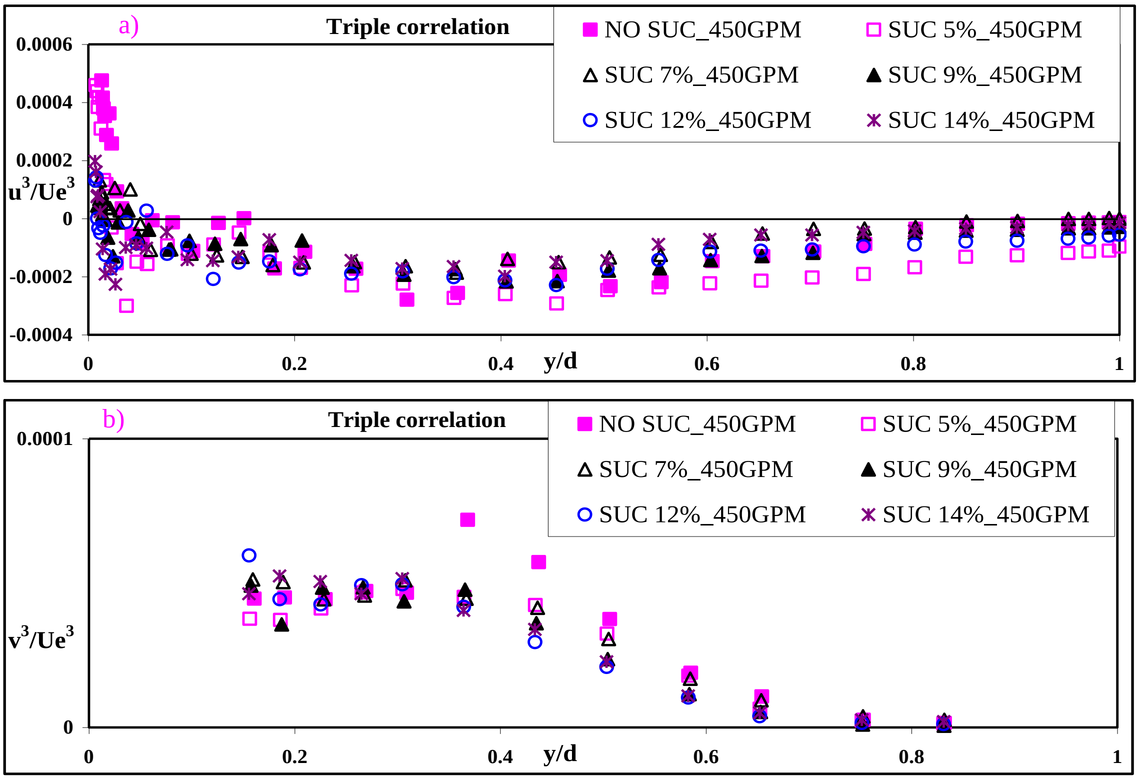

Figure 2: Distribution of different velocity triple product, a) u^3: Suction_450GPM, b) v^3: Suction_450GPM.

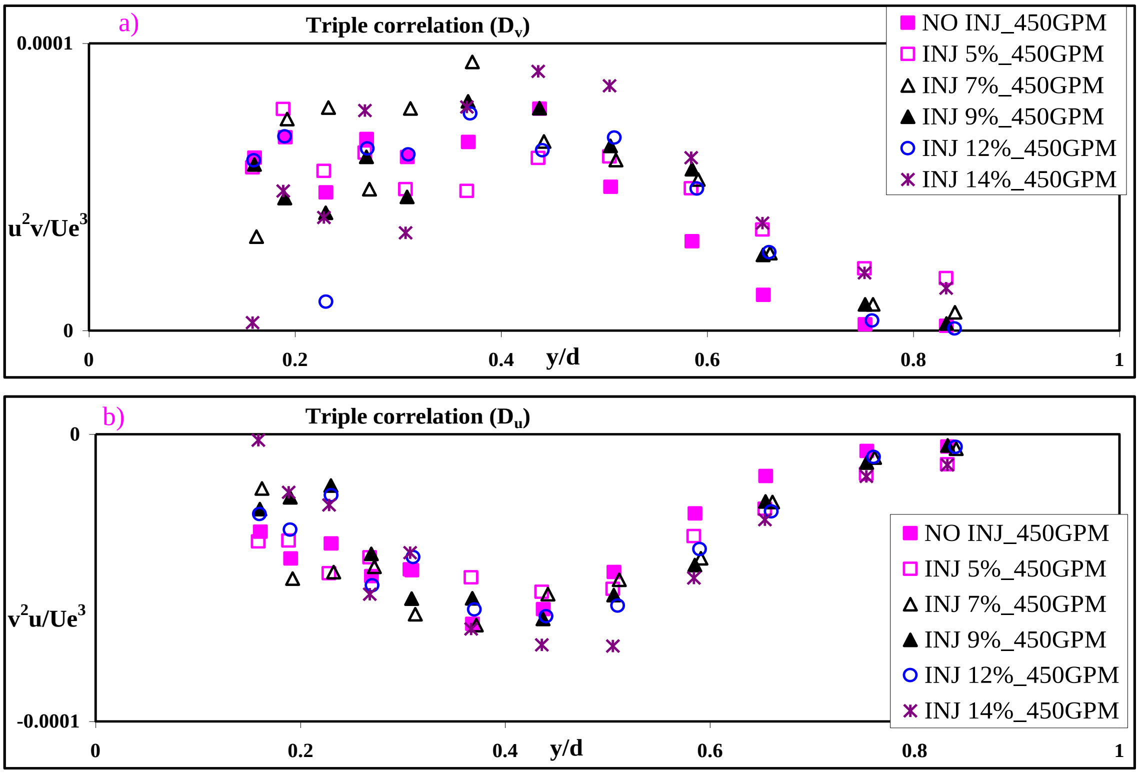

Figure 3: Distribution of turbulence diffusion, a) D_v: Injection_450GPM, b) D_u: Injection _450GPM.

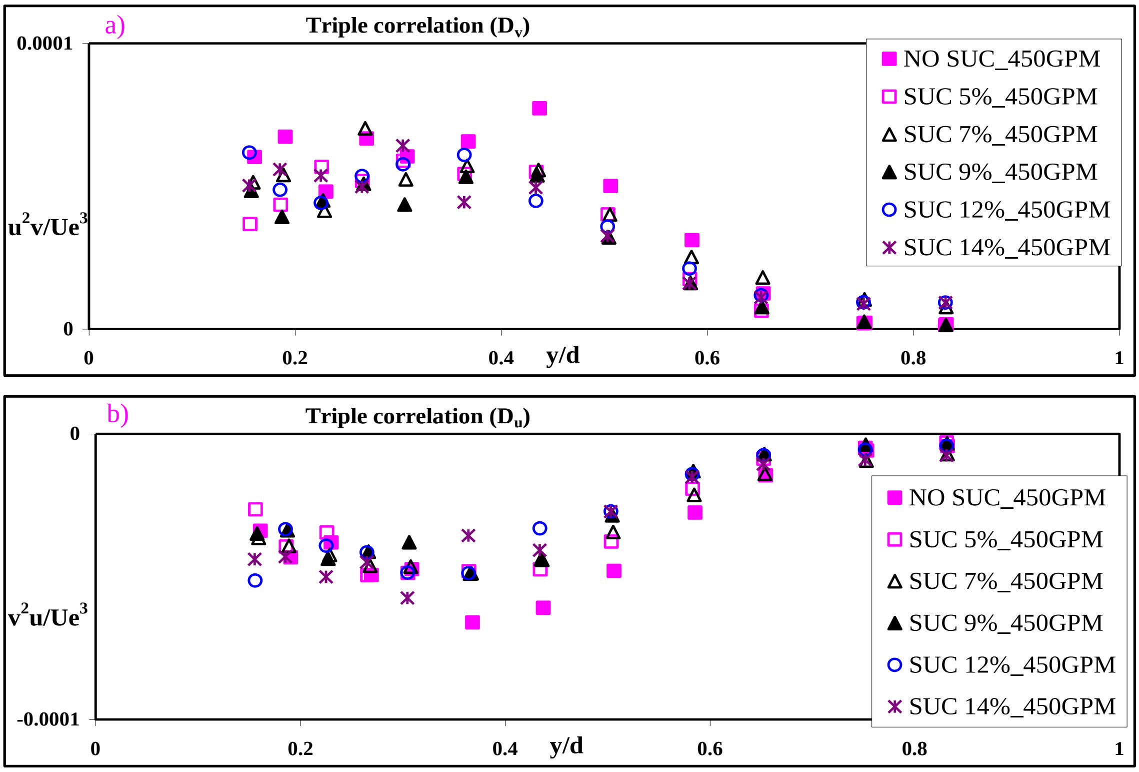

Figure 4: Distribution of turbulence diffusion, a) D_v: Suction_450GPM, b) D_u: Suction_450GPM.

4. Conclusion

The present study was carried out to understand the effects of seepage on different turbulence characteristics, velocity triple products in open channel flow (OCF) for two different flow rates. The main findings are summarized as follows:

- The effect of seepage on different turbulent characteristics is not restricted to the near-bed region but can be seen for most of the flow depth.
- Effect of injection on different turbulent characteristics is more evident with the lower flow rate, however the effect of suction seems to be independent of the flow rates.
- The effect of seepage on different turbulent characteristics is not restricted to the near-bed region but can be seen for most of the flow depth.
- Seepage can alter the flow boundary conditions and eventually affect sediment transport and can change scour phenomenon.
- The effect of suction on turbulence diffusion is clearly opposite to that noticed by injection. The change of turbulent events can potentially influence the sediment transport, resuspension of pollutant from bed, bed formation.

References

[1] Rao, A. R., and Sitaram, N. (1999). “Stability and Mobility of Sand-Bed Channels Affected by Seepage.” *Journal of Irrigation and Drainage Engineering*, 125(16), 370-379.
[2] Shukla, M. K., and Mishra, G. C. (1994). “Canal discharge and seepage relationship.” *Proceeding 6th National symposium on Hydro.* 263-274.
[3] Watters, G. Z., and Rao, M. V. P. (1971). “Hydrodynamic effects of seepage on bed particles.” J. Hydr. Div., ASCE, 101(3), 421-439.
[4] Tachie, M. F., Bergstrom, D. J., and Balachandar, R. (2003). “Roughness effects in low-*Re*□ open-channel turbulent boundary layers.” *Experiments in Fluids*, 35, 338-346.
[5] Balachandar, R., and Bhuiyan, F. (2007). “Higher-order moments of velocity fluctuations in an open channel flow with large bottom roughness.” *Journal of Hydraulic Engineering*, 133(1), 77-87.
[6] Richardson, J. R., Abt, S. R., and Richardson, E. V. (1985). “Inflow seepage influence on straight alluvial channels.” *Journal of Hydraulic Engineering*, 111(8), 1133-1147.
[7] Cheng, N. S., and Chiew, Y. M. (1998). “Turbulent open-channel flow with upward seepage.” *Journal of Hydraulic Research*, 36(3), 415-431.
[8] Nezu, I. (2005). “Open-channel flow turbulence and its research prospect in the 21st century.” *Journal of Hydraulic Engineering*, 131(4), 229-246.
[9] Grass, A. J. (1971) “Structural features of turbulent flow over smooth and rough boundaries.” *Journal of Fluid Mechanics*, 50(2), 233-255.

Available online at www.sciencedirect.com

SciVerse ScienceDirect

Procedia Engineering 00 (2012) 000–000

Procedia Engineering

www.elsevier.com/locate/procedia

5th BSME International Conference on Thermal Engineering

Study on Underexpanded Impinging Jet issued from Rectangular Nozzle

Ruhul Azam[a], Hiroaki Ozono[b], Minoru Yaga[c]*, Isao Teruya[c], Masaaki Ishikawa[c]

[a] Gentry Corporation Limited, 333/3 Segun Bagicha, Dhaka, 1000, Bangladesh
[b] Graduate school of Engineering and Science, University of the Ryukyus, 1 Senbaru, Nishihara, 903-0213, Japan
[c] Department of Mechanical Systems Engineering, University of the Ryukyus, 1 Senbaru, Nishihara, 903-0213, Japan

---

Abstract

This research is concerned primary with pressure distributions and oil flow on the plate to figure out the flow structures for the rectangular nozzles by comparing three-dimensional calculations to the experiments. Flow visualizations were performed using the oil-flow method and schlieren method in our experiments. Underexpanded impinging jet issued from rectangular nozzle of three aspect ratio (1, 3 and 5) were investigated. The flow field was calculated by solving three dimensional compressible Navie-Stokes equations. According to the flow visualization on the plate using oil flow method, it is confirmed that the flow is separated on the impinging plate from center point toward outside at only aspect ratio 1. These experimental results tell us that the flow on the plate avoids the four high pressure areas near the center point only for aspect ratio 1. The corresponding calculations were fairly good agreement with the experimental ones.

Keywords: *Supersonic, Underexpanded impinging jet, rectangular nozzle*

Nomenclature

D	characteristic length (mm)
L	nozzle to plate distance (mm)
P	pressure (Pa)
T	temperature (k)
Subscripts	
o	stagnation condition
c	center of the impinging plate
b	ambient (back) condition
w	wall condition

1. Introduction

When an impinging jet issuing from a nozzle and impinges on a surface, the surface is cooled or heated by thermal convection. A means of experimentally investigating the convective heat transfer coefficients, two dimensional temperature field and wall static pressure distributions on the impinging flat plate surface was investigated. Underexpanded impinging jets have been attracting the interest of many researchers not only because they have potentially engineering applications such as surface cooling devices, a plasma spray coating also because they are not fully understood yet. According to the

---

* Corresponding author. Tel.: +81-98-895-8617; fax: +81-98-895-8707.
E-mail address: yaga@tec.u-ryukyu.ac.jp

previous reports, even the single underexpanded impinging jet still has difficulties such as complex three dimensional flow structures which must be clarified to achieve the high performance of these devices. However, besides the investigation of these complexities, applications of these jets to engineering fields must be considered utilizing the flow characteristics of the underexpanded jets. One of the methods to achieve the goal is to have rectangular nozzle exit. So the jet impinges normally on to a heated surface, the measurement and representation of the heat transfer is not so simple. Rectangular nozzle has complex structure compare with circular exit. Minoru Yaga [1] has compared numerical and experimental results of two dimensional pressure and temperature distributions and found the results fairly good. Most of the reports of rectangular nozzles have tried to focus on the jet screech or an oscillating phenomenon and also flow structure like barrel shock waves, a core boundary, mixing regions, oblique shocks, Mack shock disk etc. However, this kind of flow is also important for rectangular nozzle because of sharp corner which has vortices effect. This research is concerned mainly with pressure distributions on the plate to figure out the flow structures for the rectangular nozzles by comparing three-dimensional calculations to the experiments. In this study, authors has focused two dimensional pressure distribution effects on the flat plate and compared with the oil flow pattern which has more clear information about the flow field of the impinging jet.

2. Experimental apparatus

All tests were carried out in intermittent blow down open jet facility. High pressure dry air at 0.7MPa and ambient temperature were discharged into atmosphere through the converging rectangular nozzles. The pressure in the settling chamber was continuously monitored using a semi-conductor pressure sensor and digitized by a computer to send a trigger to a light source for the schlieren visualization system. The two dimensional static pressure distributions on the plate were measured by utilizing traversing device. The two dimensional temperature fields were captured by an infrared radio-meter with a two dimensional array of InSb sensors (TVS-8200,AVio). The flow visualization was conducted by schlieren method with a light source as a Xenon strobe flash tube. A high resolution digital camera is used for taking the oil flow image where flax seed oil and titanium oxide are used as a solution. The detailed geometries and the definitions of the test section are illustrated in Fig.1

Three different dimension of rectangular nozzle are used in this experiment which has shown in fig.2(a). The dimensions are (7.5x7.5) mm, (15x5) mm, and (18x 3.6) mm for aspect ratio 1, 3 and 5 respectively. The characteristic length *D* is defined by:

$$D = \frac{2ab}{(a+b)}\left[mm\right] \tag{1}$$

where a and b are the width and height respectively. *D* is referred to as a hydraulic diameter. The main parameters of this experiment are the pressure ratio p_0/p_b and L/D, where the ratio of the distance L to the hydraulic diameter D. L is represented the distance between the nozzle exit and the impinging plate. The test was performed with the ratio L/D = 2, 3 and 4.

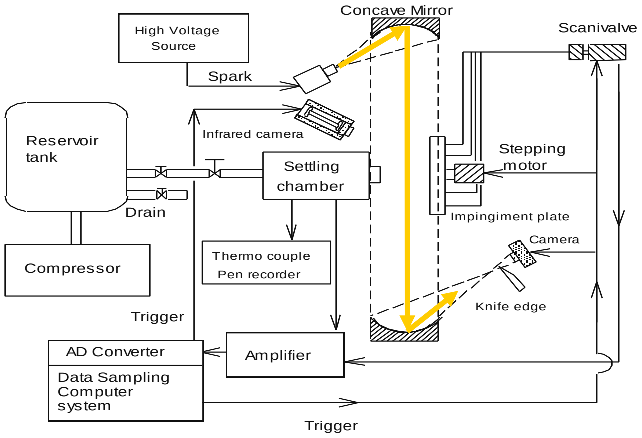

Fig.1 Experimental apparatus

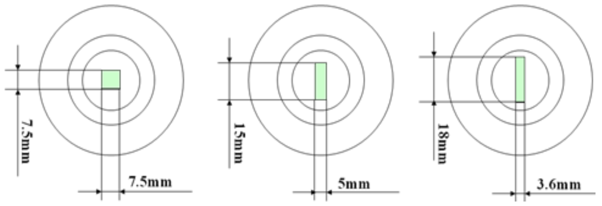

Fig.2(a) Nozzle geometry

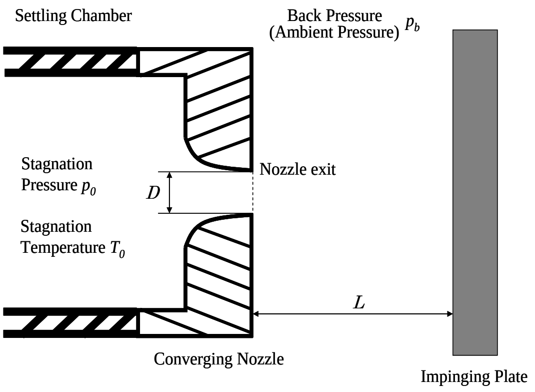

Fig.2(b) Test section

3. Numerical procedure

In this study, numerical calculations were also conducted. Three dimensional compressible Navie-Stokes equations are solved using the computational fluid dynamics solver CFD 2000 5.5i SP. The number of the grid points depends on the calculation conditions, for example, 80 x 80 x 40 for aspect ratio 1. The vertical and horizontal boundaries were considered as outgoing flow conditions. The pressure was fixed at the atmospheric pressure. The uniform choke condition was applied to the nozzle exit. Non slip conditions were applied to the impinging plate.

4. Results and Discussion

4.1. pressure variation at the stagnation point

Figure 3 shows the variation in the stagnation pressure at the center point of the impinging plate with *L/D*=2 for aspect ratio 1, 3 and 5. The pressure is normalized by the back pressure condition. It is found that the stagnation pressure at the center position does not increase monotonically with the pressure ratio and that the variations in the stagnation pressure are affected considerably by the nozzle type, that is, the aspect ratio. Among the variations in the stagnation pressure, the largest one was achieved by the aspect ratio of 5 at the p_0/p_b=3.8. Each stagnation pressure increases in the range of pressure ratio from 1.0 to 3.5 and it reaches maximum for each aspect ratio 1 and 3 at p_0/p_b=3.5. After that the pressure drops rapidly larger than p_0/p_b= 3.5 and then increases gradually only for aspect ratio 1. Figure 3 also shows that the sudden decrease in the pressure at p_0/p_b=3.5, where as the other two causes reveal no sudden change as that for aspect ratio 1.

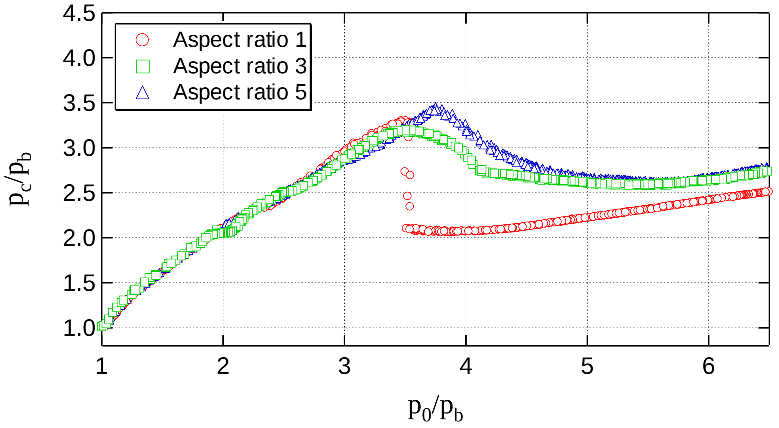

Fig.3 Variations of pressure at stagnation point with pressure ratio for *L/D*=2.0

4.2. oil flow pattern

In order to confirm the flow direction and the phenomenon on the plate, the visualization using the oil flow method was performed. Figures 4 show the cases for the aspect ratio 1 and *L/D* =2.0 at the pressure ratio p_0/p_b = 3.0, 3.5 and 4.0, which cover the range of the pressure ratio with the great change in the stagnation pressure as shown in Fig.3. Figure 4 (a) shows the circular dark region around *x/D* = ±1.0 meaning that the strong shear flow exists around this region. In Fig.4 (b), three white spots accumulating oil solution on the circular dark region can be seen. In this pressure ratio of p_0/p_b = 3.5, the stagnation pressure is sharply decreased at the center point which suggests that the flow mechanism is changed and might be separated around on the circular dark regions. For the pressure ratio p_0/p_b= 3.0 and 3.5 in Fig.4 (a) and 4(b), the flow stream line from the center point to outward in a radial pattern can be seen. However, from Fig.4 (c), the oil solution is accumulated at the center point, which suggests the flow direction is changed near the center point and a separation bubble is generated around it. Therefore, the stagnation pressure is sharply decreased at the center point over the p_0/p_b = 3.5.

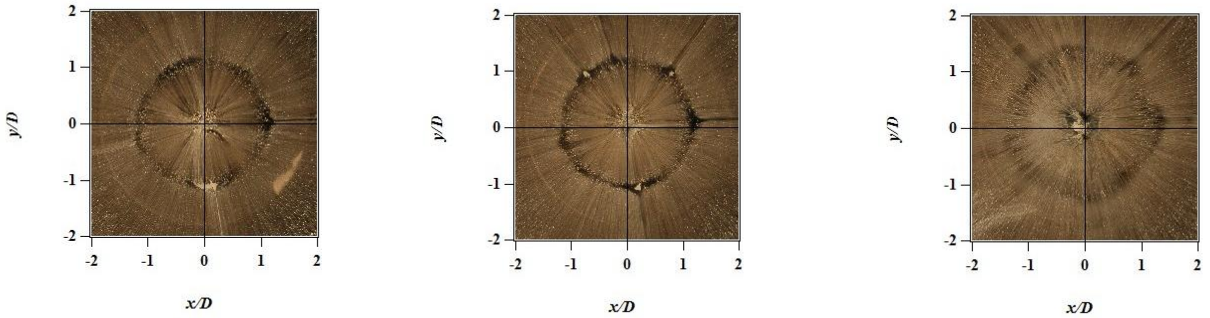

(a) p_0/p_b = 3.0

(b) p_0/p_b = 3.5

(c) p_0/p_b = 4.0

Fig.4 Oil flow images for aspect ratio 1 and *L/D*=2.0

4.3. Flow pattern of aspect ratio 1

Figures 5 and 6 show the experimental results of the oil flow images, the pressure contour, pressure distribution and calculated pressure contour at the pressure ratio p_0/p_b = 4.0 and 5.0 for *L/D* =2.0. Figures 5 tell us that the calculation agrees well with experiment concerning the wall pressure distributions. Oil flow image shown in Fig.5 (a) illustrates the separation bubble near the center point and that the dark polygonal shape region along *x/D* = ±1.2 was similar to calculated contour shown in Fig.5 (c). In Fig.5 (a), four or three dark lines from center point to outward diagonally can be seen. It is found that the flow on the plate avoids the high pressure areas near center plate. Both pressure contours Figs.5 (b) and 5 (c) indicate that the pressure peak on the impinging plate occurred around *y/D* = ±0.8 and the stagnation pressure (at *x/D* and

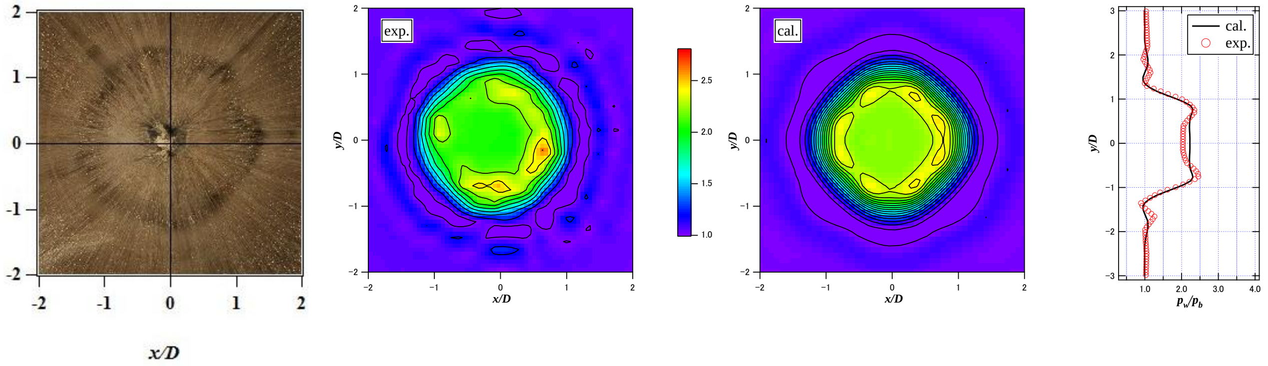

(a) Oil flow images

(b) Pressure contour

(c) Calculated contour

(d) Pressure distribution along *x/D* = 0

Fig.5 Aspect ratio 1 with p_0/p_b = 4.0 for *L/D*=2.0

y/D = 0) does not recover up to the total pressure p_0/p_b = 4.0, which is due to the generating separation bubble. Figure 5 (c) also indicates that the comparisons between experiment and the calculation show fairly good agreements. These pressure drops are also confirmed in Fig. 3.

In case of p_0/p_b = 5.0 as shown in Figs.6, these figures also show the calculation agrees with the experiment. Especially, in oil flow image shown in Fig.6 (a), the dark polygonal region around $\sqrt{x^2+y^2}/D = \pm 1.5$ was considerably similar to calculated pressure contour as shown in Fig.6 (c). Moreover Fig.6 (a) indicates that separation bubble near the center point extends region of accumulating oil solutions compared with previous Fig.5 (a). According to the experimental pressure contour Fig.6 (b), region around *y/D* and *x/D* = ±0.8, sharp pressure peaks can not be seen. However, the calculated contour shows that the clear several peaks at *y/D* and *x/D* = ±1.0.

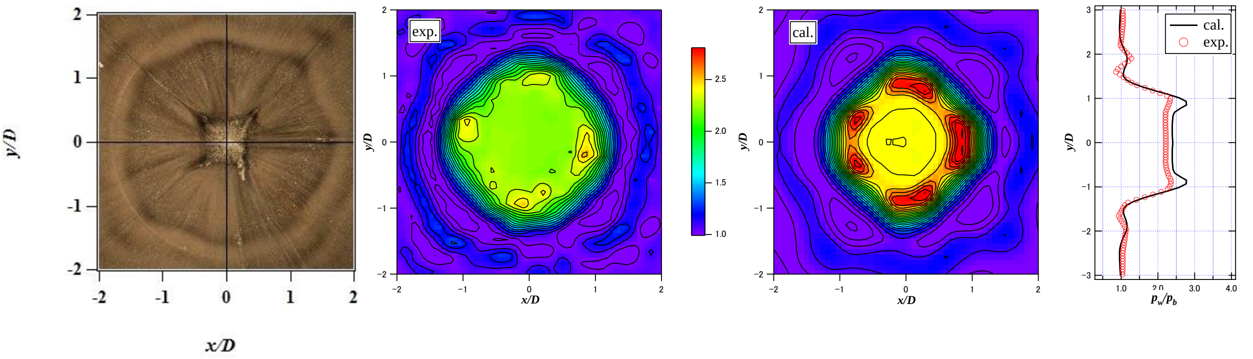

(a) Oil flow images (b) Pressure contour (c) Calculated contour (d) Pressure distribution along *x/D* = 0

Fig.6 Aspect ratio 1 with p_0/p_b = 5.0 for *L/D*=2.0

4.4. Vector fields and schlieren images

Calculations provide us with detail flow structures that cannot be obtained by experiments. One of the useful data from the calculations is vector fields. In order to figure out more detail of the flow structures, comparison calculated density contours, vector fields and visualization using the schlieren method were performed and shown in Fig.7 (a) and (b) for aspect ratio of 1, *L/D*=2.0, p_0/p_b = 4.0 and 5.0, respectively. These schlieren images illustrate the flow boundary, oblique shock wave and mach disk. Schlieren image for p_0/p_b = 5.0 shown in figure7 (b), flow boundary was extends compared with Fig.7 (b). Both cross view show the flow on the plate was separated at *y/D* = ±0.6 and the recirculation flow near the

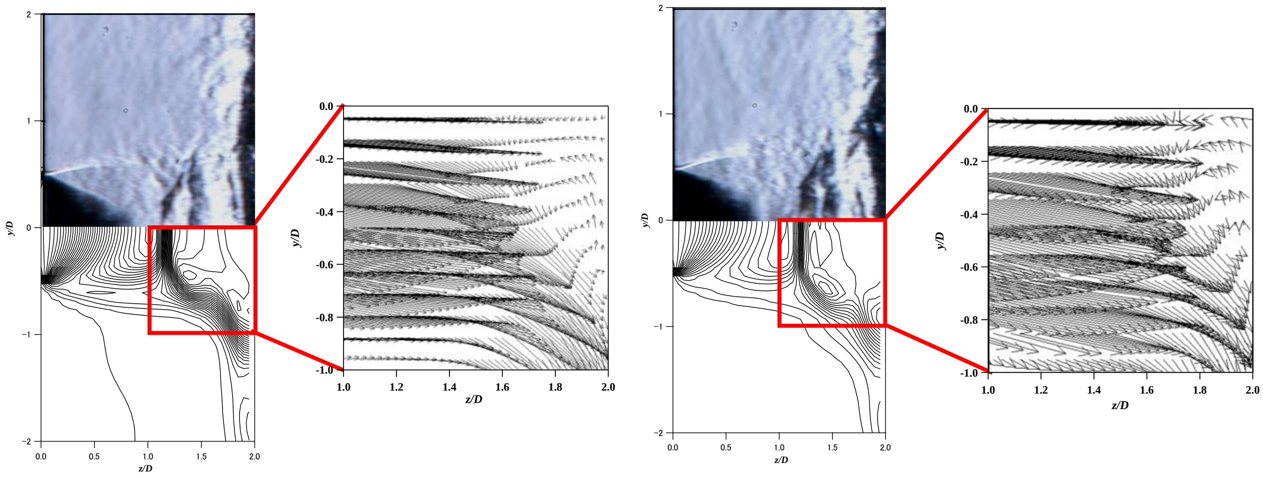

(a) p_0/p_b = 4.0 (b) p_0/p_b = 5.0

Fig.7 Schlieren images, density contours and flow vectors with aspect ratio1 plate can be seen. It suggests that the accumulating oil solution at center point on the plate shown in previous Fig.6 (a) was caused by this recirculation flow.

Conclusion

The underexpanded impinging jets are experimentally and numerically investigated with the rectangular nozzles. The results are summarized as follows:

1) The stagnation wall pressure drop rapidly at larger than p_0/p_b= 3.5 and then increases gradually only for aspect ratio 1. It caused by separation bubble near the center point on the plate.
2) In case of the aspect ratio 1 and L/D=2.0, flow direction on the impinging plate was separated at y/D = ±0.6 and the recirculation flow near the plate can be seen for calculated vector field.
3) In case of p_0/p_b = 5.0, oil flow image illustrates the dark polygonal region around $\sqrt{x^2+y^2}\,/D$ = ±1.5 which correspond to the low pressure area of the calculated pressure contour.

References

[1] M.Yaga, K.Ueda, T,Oshiro, Experimental and Three-Dimensional Numerical Study on Underexpanded Impinging Jets. Journal of Thermal Science, 2000, 9, No.4: 316-321
[2] M.Yaga, M.Okano, M.Tamashiro, K.Oyakawa, Experimental and Numerical Study of Twin Underexpanded Impinging Jets, Journal of Thermal Science Vol.12, No.3, pp.254-259, 2003.
[3] Kowalsky, K A, Marantz, D R, Smith, M F, et al. HVOF: Particle, Flame Diagnostics and Application. In: Proc. of the Third National Thermal Spray Conference, Long Beach, CA, USA, 1990. 587–792
[4] Sakakibara, Y, Iwamoto, J. Numerical Study of Oscillation Mechanism in Underexpanded Jet Impinging on Plate. ASME Journal of Fluid Engineering, 1998, 120: 477–481.
[5] Kitamura, S, Iwamoto, J. Numerical Analysis of Supersonic Impinging Jet. Trans. Japan Soc. Aero. Space Sci., 1997, 41(132): 57–64
[6] Tannehill, J C, Anderson, D A, Pleycher, R H. Computational Fluid Mechanics and Heat Transfer. 2nd Edition. Bristol, Pennsylvania, USA: Taylor & Francis, 1997. 388–39

Available online at www.sciencedirect.com

SciVerse ScienceDirect

Procedia Engineering 00 (2012) 000–000

Procedia Engineering

www.elsevier.com/locate/procedia

5th BSME International Conference on Thermal Engineering

Impact of DWR Radial Winds, Reflectivity and Cumulus Physics on the predictions of Mesoscale Convective Systems

Mohan K. Das[a,*], Sujit K. Debsarma[a], Someshwar Das[b]

[a]*Research Officer, SAARC Meteorological Research Centre (SMRC), Plot-E-4/C, Sher-E-Bangla Nagar, Dhaka-1207, Bangladesh*
[b]*Scientist-G/Adviser*, **National Centre For Medium Range Weather Forecasting** *(NCMRWF), NOIDA, PIN-201307, India*

Abstract

The quantitative data such as Doppler Weather Radar (DWR) radial winds and reflectivity are useful for improvement of the numerical prediction of weather events like squalls. Mesoscale convective systems (MCS) are responsible for majority of the squall and hail events and related natural hazards that occur over Bangladesh and surrounding region in pre-monsoon season. In this study, DWR observations (radial winds and reflectivity) of Bangladesh Meteorological Departments (BMD) are used during 19 May 2011 squall events in order to update the initial and boundary conditions through three-dimensional variational assimilation (3DVAR) technique within the Weather Research Forecasting (WRF) modeling system. The simulated mean sea level pressure and 850 hPa wind fields from the experiments are presented in this study in order to analyze the observed and simulated features of the squall events. The model results are also compared with the Kalpana-1 images and the India Meteorological Department (IMD) predicted results. Further, the intensity of the events, generated from the simulations is also compared with the BMD predictions in order to evaluate the model performance.

Keywords: Squall; MCS; WRF modeling system; 3DVAR assimilation; DWR radial winds; reflectivity.

---

1. Introduction

The variational data assimilation approach is one of the most promising techniques available to directly assimilate heterogeneous mesoscale observations in order to improve the estimate of the models initial state. In this study a 3DVAR data assimilation scheme has been used with the Weather Research and Forecasting (WRF) model to assimilate the special observations collected during the STORM Field Experiments. STORM is an acronym for Severe Thunderstorm Observations and Regional Modeling. The STORM Pilot Field Experiment was conducted during April to May 2009 to 2011 jointly with India, Bangladesh, Nepal and Bhutan to study the characteristics of severe thunderstorms (also known as Nor'westers) that affect these countries during the pre-monsoon season.

In order to study the impact of the special observations on forecasts, 2 sets of experiments were conducted to study the episodes of 19 May 2011 thunderstorm. The 1st set of experiments were the control experiments (CTRL) in which 24 hours forecasts were made based on the initial conditions produced by the T254L64 global model of NCMRWF. The 2nd set of experiments (DA) was conducted based on the initial conditions produced by assimilating the special field observations. Results were analyzed and compared for the 2 experiments CTRL and DA. The simulated and assimilated results showed the presence of strong vertical wind shear and an advection of warm air forming a solenoidal field during the Nor'wester (Das et al., 2006). Study of Radar data showed that the Nor'westers propagate in the form of parallel bow shaped squall lines having horizontal length of more than 250 km at 0500 to 1000 UTC. The model underestimated the strength of the squall lines in general in its present configuration.

---

* Corresponding author. Tel.: +880-2-8181728; fax: +880-2-8181727.
E-mail address: mkdas@saarc-smrc.org

2. Materials and Method

The WRF Model has been used over the study domain. The model is run at 9 km resolution with 27 vertical levels using initial and boundary conditions obtained from NCMRWF T254L64 global model. 6 hourly NCEP-FNL Data (1°x1°), GTS data, BMD Khepupara DWR radial wind and reflectivity data are utilized in the Experiments. Kain-Fritsch and Grell-Devenyi (GD) ensemble cumulus scheme have been used in the model run. Realized weather phenomena over Bangladesh and surroundings on 19 May 2011 shown in Table 1. Six persons died due to lightning strike in Orrissa, India at night.

Table 1. Realized weather phenomena over Bangladesh and surroundings on 19 May 2011.

Station	Types	Wind Speed kph	Occurrence Time (UTC)
Chittagong	Squall	56	0100
Ranchi	Squall	44	1655-1657
Alipur	Squall	49	2100-2101
Lengpuri	TS	--	0300-0345
Shillong	TS Rain	--	0310-0930
Tezpur	TS	--	2130-0040

If table footnotes should be used, place footnotes to tables below the table body and indicate them with superscript lowercase letters. Be sparing in the use of tables and ensure that the data presented in tables do not duplicate results described elsewhere in the article.

2.1. *Synoptic main feature*

i) Trough of low lies over North Bay.
ii) Seasonal low lies over South Bay.
iii) The upper air cyclonic circulation over Punjab and neighbourhood in lower levels persists. A trough from this system extends up to Gangetic West Bengal across Haryana, south Uttar Pradesh, north Madhya Pradesh, Chhattisgarh and Jharkhand.
iv) The upper air cyclonic circulation lies over Assam and neighbourhood in lower levels.

2.2. *The 3DVAR System*

The three dimensional variational assimilation (3DVAR) is designed for a community data assimilation system flexible enough to allow a variety of research studies apart from its operational utilization. The basic goal of the 3DVAR system is to produce an “optimal” estimate of the true atmospheric state at any desired analysis time through iterative solution of a prescribed cost-function (Ide *et al.*, 1997).

The 3DVAR system consists of the four components (Barker *et al.*,, 2003, 2004): (1) Background Pre-processing, (2) Observation Pre-processing and quality control, (3) Variational Analysis, (4) Updation of Boundary Conditions.

2.3. *Updating boundary condition*

In order to run WRF forecast model using 3DVAR analysis as initial conditions, the lateral boundary conditions (originally computed from global model data) is updated to reflect the modified fields.

Three-dimensional observations are mainly centered on the main synoptic hours (0000, 0600, 1200, 1800 UTC) of observation. Keeping this in mind, the present assimilation system is designed as a 6-hrly intermittent assimilation scheme, where analysis is performed four times a day i.e. at 0000, 0600, 1200, 1800 UTC. The control analysis consists of the global data received through GTS/internet, which are ingested in the system at the analysis time with ±3 hours time window. Modules have been developed for reading the decoded observed data from NCMRWF’s operational data sets and for packing in LITTLE-R format, required for ingesting in 3DVAR observation preprocessor. In the present study, two experiments have been conducted. The first one is a control run (CTRL) in which the analysis produced by the NCMRWF global model (T254L64) is used for initial and boundary conditions to run the WRF model. In the second experiment (DA), continuous data assimilation (cyclic run) is carried out using the observations collected during the SAARC STORM Pilot Field Experiment of 2011 (mainly the AWS and SYNOP). In the cyclic run, the boundary conditions for WRF run are taken from global model analysis. However, the lateral boundary conditions are updated after each analysis. Subsequently, after each analysis, six-hour forecasts are made using WRF model. The 6-hour forecast of each run (valid for next analysis time) is used as the first guess for the next analysis (Parish *et al.*, 1992). The assimilation started at 06Z of 19 May 2011 and completed at 06Z of 20 May 2011. Subsequently, 24 hours forecasts were made for the event of widespread thunderstorms (discussed in the next section) based on the CTRL and DA run.

3. Results and Discussion

The impact of 3DVAR assimilation upon the first guess is studied here. It is seen that the experimental (DA) runs have simulated 10m wind speed of about 12-24 m/s in big patches in the West Bengal and northwest region. Whereas the control run has produced 10m wind speed greater than 12 m/s over the region. High shear regions are wide spread in the West Bengal and Bihar region in the experimental forecasts whereas, the control forecasts have small wind shear restricted over a small region (Barker *et al.*, 2004). Fig. 1 presents the reflectivity, for forecasts valid at 0855 UTC of 19 May, 2011. 850hPa horizontal winds in the experimental forecasts are having higher gustiness over the region of the observed system compared to the control forecasts.

3.1. *T- Φ gram analysis*

Dhaka T- Φ gram indicated K index 42.7 and Totals Totals Index 47.8 at 0000 UTC. The total precipitable water content stayed at 71.87 mm favouring convective activity.

Kolkata T- Φ gram indicated K index 37 and Totals Totals Index 46.3 at 0000 UTC. The total precipitable water content stayed at 58.37 mm favouring convective activity.

Mohanbari T- Φ gram indicated K index 38.2 and Totals Totals Index 48.3 at 0000 UTC. The total precipitable water content stayed at 57.53 mm favouring convective activity.

Agartala T- Φ gram indicated K index 38 and Totals Totals Index 46.80 at 0000 UTC. The total precipitable water content stayed at 54.82 mm favouring convective activity.

Patna T- Φ gram indicated a low CAPE (636.96 J/kg) at 0000 UTC. The total precipitable water content stayed at 58.94 mm favouring convective activity.

Guwahati T- Φ gram indicated K index 35.30 and Totals Totals Index 52.20 at 0000 UTC. The total precipitable water content stayed at 43.28 mm favouring convective activity.

Bhubaneshwar T- Φ gram indicated a very high CAPE (4036 J/kg) and low CINE (-151 J/kg) at 0000 UTC. The total precipitable water content stayed at 50.02 mm favouring convective activity.

3.2. Doppler Weather Radar and Kalpana-1 Satellite Analysis

Doppler Weather Radar (DWR) Kolkata recorded the vertical extent of the system of about 16 km and the RADAR reflectivity 45 dBz. Fig. 1 showed an echo to the east of India at 0855 UTC, which intensified into a squall line of 300 km length by 1000 UTC.

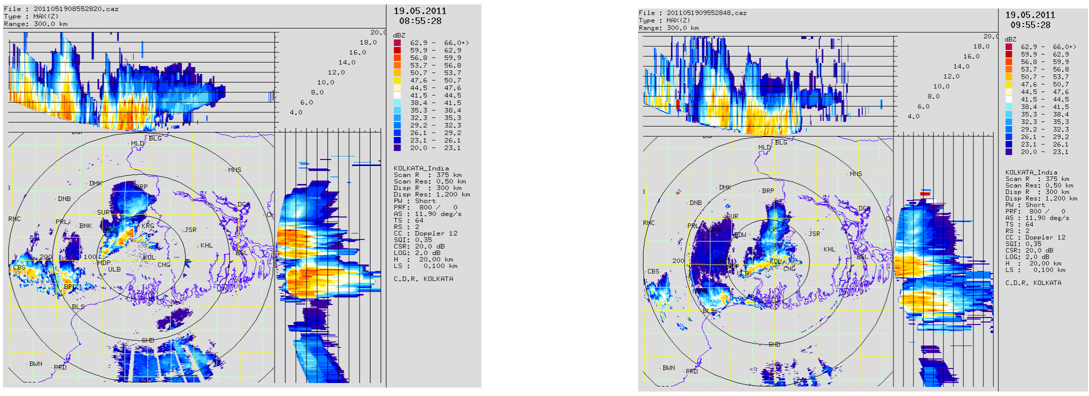

(a)

(b)

Fig. 1. Observed Reflectivity on 19 May 2011 at (a) 0855 UTC and (b) 0955 UTC.

Kalpana-1 satellite imagery (Fig. 2) showed strong convection over eastern India (Cloud Top Temperature, CTT = -70^{0}C), moving southeastwards it expanded into Bangladesh and merged with convection over Jharkhand, Orissa and West Bengal (CTT = -80^{0}C). Moving south it dissipated over the sea after 2330 UTC. Convection persisted over northwest Bay.

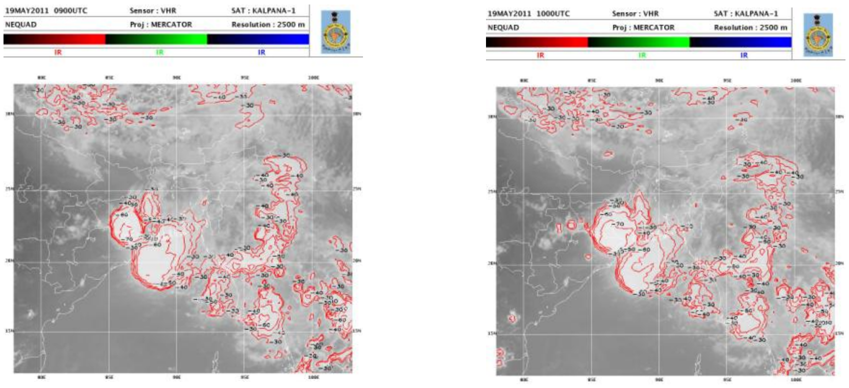

(a) (b)

Fig. 2: Observed CTT on 19 May 2011 at (a) 0900 UTC and (b) 1000 UTC.

3.3. Impact of assimilated data on the forecast fields

The 19 May 2011 episode of thunderstorms was simulated using both CTRL and DA analyses. The model was integrated for 24 hours for the case. Results of simulations and the impact of data assimilation on the case are described below.

3.3.1. Convective parameterization schemes (CPSs)

The state-of-the-art mesoscale model (WRF–NMMV2.2) was used by Litta and Mohanty (2008) to study the performance of cloud-resolving simulation of the cloud ensemble scheme for cumulus parameterization. The first simulation used the Kain-Fritsch scheme (KF), based on Kain (Kain, 2004) and Kain and Fritsch (Kain and Fritsch, 1993). The second one used Grell-Devenyi ensemble (GD) parameterization, based on Grell and Devenyi (Grell and Devenyi, 2002).

A particular convective scheme may work for a particular event or Idealized case convective environment, but may not work in others. The initialization effectiveness of a particular scheme to simulate the convection depends on the design aspects of the scheme that includes its triggering function, closure assumption, and precipitation scheme. However, the assumption and simplification of a particular convective scheme has basically limited its effectiveness.

The choice of schemes was based on a prior experiment for which the results were reported elsewhere. To compare the differences among the CPSs, simulations are performed for a particular time period utilizing the same initial and boundary conditions (BC) and other physical parameterizations for each CPSs and then model outputs are compared with observation. An attempt is made to examine different stability indices obtained from simulations with different CPSs on 19 May 2011 at 0900 UTC over Dhaka (23.76^0 N, 90.38^0 E). Observed data is used for the validation of model simulated stability indices (Table 2).

Table 2. The inter-comparison of Observed at 0000 UTC and model simulated stability indices with different CPSs and DA run over Dhaka valid for 19May 2011 at 0900 UTC.

Stability Index	KF	GD	DA Run	Observed
K	24	27	30	42.7
TT	40	41	45	47.8

3.3.2 Simulated Characteristics

Fig. 3 presents the 850 hPa horizontal wind, for forecasts valid at 1200 UTC of 19 May, 2011. 850hPa horizontal winds in the experimental forecasts are having higher gustiness over the region of the observed system compared to the control forecasts. There is a strong trough at 850 hPa simulated by the DA; this is absent in the CTRL run. The 700 hPa horizontal wind shows a trough and high wind velocity over the thunderstorm location. The phenomena are stronger in the DA run (Dasgupta *et al.*, 2005).

Fig. 4 presents the 10 m wind speed and vector wind at 950 hPa, for CTRL and DA valid at 1200 UTC of 19 May, 2011. It is seen that in the region 18.5^0 - 22.5^0N and 83^0 - 88^0E, the DA runs have simulated more than 22 m/s of 10 m wind speed. The value simulated by the control run is quiet less (about 14-16 m/s) and in the region 18^0 - 22.5^0N and 84^0 - 88^0E. The control and DA run has also simulated high 10m wind speed along the coastal belt of West Bengal. Wind shear significantly improved over the region of northeast India and the eastern region of the study domain.

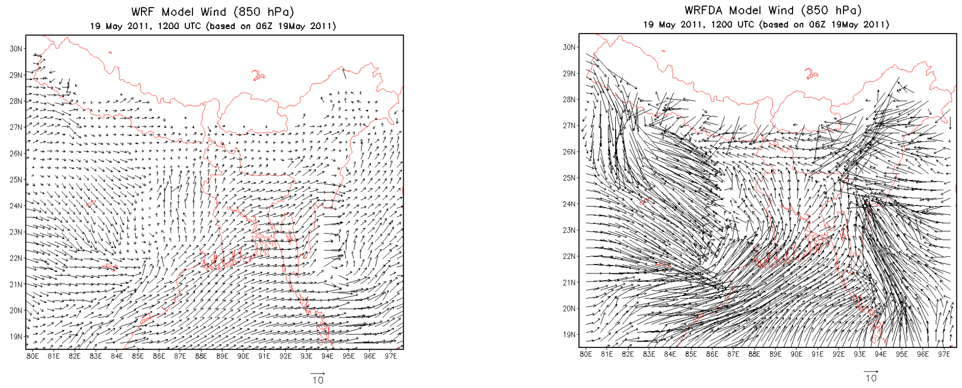

(a) (b)

Fig. 3: 850 hPa wind vector forecasts valid at 1200 UTC of 19 May 2011 (a) CTRL run and (b) DA run.

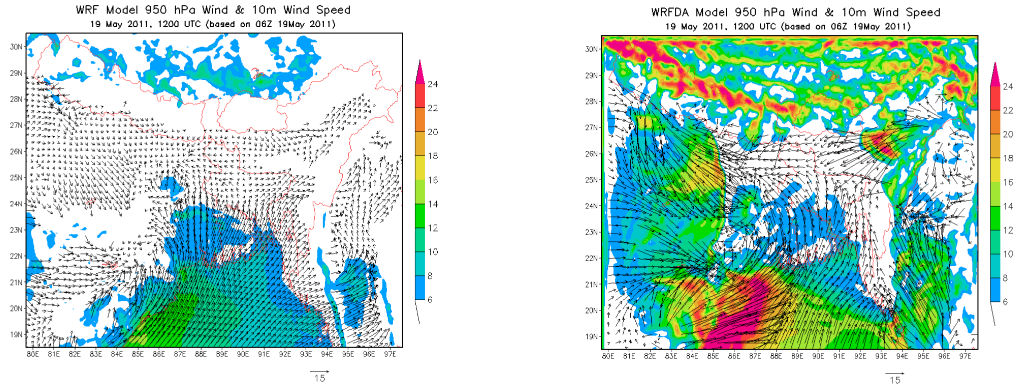

(a) (b)

Fig. 4: Vector Wind at 950 hPa and 10 m wind speed (m/s) forecasts valid at 1200 UTC of 19 May 2011 (a) CTRL run and (b) DA run.

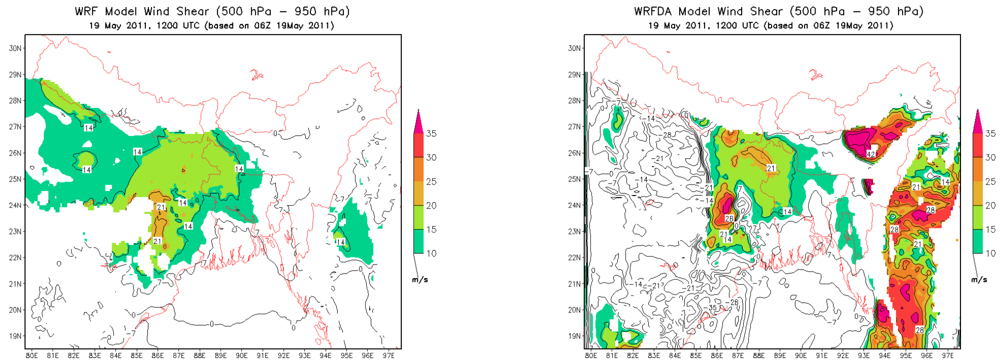

(a) (b)

Fig. 5: Wind Shear of [500 – 950 hPa] (m/s) forecasts valid at 1200 UTC of 19 May 2011 (a) CTRL run and (b) DA run.

Signal of severe thunderstorm activity over the observed region is present in the model simulated Mean CAPE (J/kg) and Mean CINE (J/kg) for forecasts valid at 1100 UTC of 19 May, 2011. Fig. 5 presents the wind shear between 500 and 950 hPa pressure levels for forecasts valid at 1200 UTC of 19 May, 2011.

Regions having the shear values above 10m/s have been shaded. Both the simulations are able to produce maxima in shear (> 10 m/s) in the region of the max. dBZ as simulated by the model. High shear regions are wide spread in the West Bengal, Bihar and northwest of Bangladesh region in the CTRL and DA run.

3.3.3 SLP Time Series

An attempt has been taken to plot time series of sea level pressure (SLP) after Data Assimilation over Chittagong (22.22^{0} N, 91.80^{0} E), Bangladesh, Alipore (22.32^{0} N, 88.20^{0} E), India, Ranchi (23.19^{0} N, 85.19^{0} E), India and Shillong (25.34^{0} N, 91.53^{0} E), India.

Sea Level pressure seems to be less than 1003 hPa over the West Bengal and adjoining regions compared to other areas (Fig. 6), due to existence of heat low during the pre-monsoon.

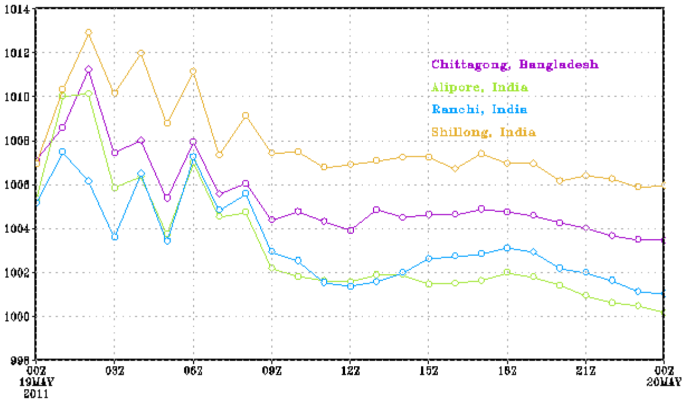

Fig. 6. Time Series of SLP at Chittagong, Alipore and Ranchi and Shillong..

4. Conclusion

The impact of data assimilation is very clearly highlighted as the experimental simulations from the WRF-3DVAR are able to capture the thunderstorm closer to the observations compared to the control run. The position and intensity of the simulated thunderstorms in the experimental runs is close to the observed values, as compared to the DWR images.

The thunderstorm event from the model simulation is best highlighted from the spatial distribution of 10 m wind speed and maximum reflectivity. They are in turn supported by the wind shear within 500 to 850hPa pressure level. It is observed that the signature of the thunderstorm activity is well represented in the model generated CAPE and CINE distributions. The 850 and 700hPa wind fields also reflects the system captured by the model simulations.

The model is still not able to accurately produce the exact location and time of occurrences of the thunderstorms. The genesis and growth of cells, their horizontal distribution, vertical structure, the direction and speed of their movement and time of dissipation are still some of the challenges unresolved by the model.

Acknowledgements

The National Centre for Atmospheric Research (NCAR), USA is gratefully acknowledged for making the WRF model available to the research community. The authors are grateful to the Director, SAARC Meteorological Research Centre (SMRC) for facilitating the study, and encouragements.

References

[1] Barker D. M., W. Huang, Y.-R. Guo and Al Bourgeois, 2003: A Three Dimensional Variational (3DVAR) Data Assimilation System For Use With MM5, *NACR Technical Note, NCAR/TN-453+STR*, February 2003, pp 68.

[2] Barker D. M., W. Huang, Y.-R. Guo and Q. N. Xio (2004): A three dimensional Variational (3DVAR) Data Assimilation Syatem with MM5: Implementation and Initial results. Mon. Wea. Rev., **132**, 897-914.

[3] Das, Someshwar, R. Ashrit and M. W. Moncrieff, "Simulation of a Himalayan Cloudburst Event" *Journal of Earth System Science*, **115** (3), pp. 299-313, 2006.

[4] Dasgupta, M., J. P. George and S. Das, 2005: Performance of MM5-3DVAR system over Indian Sub-continent. International Conf. on MONEX and its legacy, 3-7 Feb 2005, Delhi.

[5] Grell, G. A., and Devenyi, D. 2002 A generalized approach to parameterizing convection combining ensemble and data assimilation techniques. Geophysical Research Letter. 29, Article 1963.

[6] Ide, K., P. Courtier, M. Ghil and A. C. Lorenc, 1997: Unified notation for data assimilation: Operational, sequential and variational. *J. Meteor. Soc. Japan*, **75**, 181-189.

[7] Kain, J. S. 2004. The Kain–Fritsch Convective Parameterization: An Update. Journal of Applied Meteorology. **43** (1), 170–181.

[8] Kain, J. S., and Fritsch, J. M. 1993. Convective parameterization for mesoscale models: The Kain-Fritcsh scheme. The representation of cumulus convection in numerical models, K.A. Emanuel and D.J. Raymond, Eds., Amer. Meteor. Soc. 246.

[9] Litta A. J., and Mohanty U. C. 2008. Simulation of a severe thunderstorm event during the field experiment of STORM programme 2006, using WRF_NMM model, Current Science/Indian Academy of Science. VOL. 95, NO. 2, 204-215.

[10] Parish, D. F. and J.C. Derber, 1992: The National Meteorological Centre's Spectral Statistical Interpolation analysis system. *Mon. Wea. Rev.*,**120**, 1747-1763.

Available online at www.sciencedirect.com

SciVerse ScienceDirect

Procedia Engineering 00 (2012) 000–000

Procedia Engineering

www.elsevier.com/locate/procedia

5th BSME International Conference on Thermal Engineering

Calibration Methodology of Wall Shear Stress Sensor

Akshoy Ranjan Paul[a]*, Shrey Joshi[b], Aman Jindal[b], Vikrant Singh Yadav[b] Ajit Verma[c]

[a]Department of Applied Mechanics, [b]Department of Mechanical Engg., [c]Department of Chemical Engg.
Motilal Nehru National Institute of Technology, Allahabad-211004, India.

Abstract

Shear stress is an important parameter in field of fluid flow, be it external or internal flow, for calculating and anticipating the severity of drag and surface wear. Determination of wall shear stress (τ_w) values and hence the skin friction coefficient (C_f) helps a lot is determining the flow separation and its reattachment. The values of shear stress plays an explicit role in flow analysis and predicting flow stall but determination of shear stress is not that easy as measurements of other flow parameters. The existing techniques are quite complicated and hard to build up. Measuring instruments like Preston tube have been used in the past for this purpose but has a tedious calculation. The paper gives a details regarding calibration of a wall shear stress sensor which works on the principle of constant temperature anemometer.

Keywords: Wall-shear stress sensor (WSS); Flow separation; Calibration;

Nomenclature

A	calibration coefficient
B	calibration coefficient
d	height from the plate surface (m)
E	voltage value, V
Δp	dynamic pressure = $p_t - p_s$ (N/m^2)
R^2	Coefficient of determination
u	local flow velocity (m/s)
U	free stream velocity (m/s)
x	abscissa (m)
y	ordinate (m)
Greek symbols	
β	momentum thickness(m)
δ	boundary layer thicknesses(m)
δ^+	displacement thickness (m)
τ_w	wall shear stress (N/m^2)
ρ	density of air (kg/m^3)
υ	kinematic viscosity (m^2/s)
Subscripts	
p_s	static pressure measured from pressure taping on the flat plate (N/m^2)

---

* Corresponding author. Tel.: +91-532-227 1212.
E-mail address: arpaul2k@yahoo.co.in

p_t	total pressure measured using total pressure probe (N/m^2)

1. Introduction

The wall shear stress measurement often becomes important for prediction of certain phenomenon like separation, turbulent energy dissipation, reattachment etc. But lack of measuring techniques and related equipments make it challenging to measure and quantify the value and at times leads difference between the actual flow conditions and the inferences from the measurements. The existing techniques are quite complicated and hard to build up. This involves measurement from Preston tube or measurements using surface films, at times the objective of shear stress measurement is achieved using surface flow visualization. The sensor was calibrated using a conventional Preston tube. Preston (1954) described a method of measuring skin-friction which promised to be both accurate and convenient. Preston tube is essentially a pitot tube. It is assumed that close to the wall in turbulent shear flow, there exists a region in which flow is substantially determined by the wall shear stress and the relevant properties of fluid, independent of the nature of outer flow field and quantities like pressure gradient and surface curvature. The equation given by Preston is:

$$f\left(\tau_w d^2/4\rho\nu^2\right)=\Delta p d^2/4\rho\nu^2 \qquad (1)$$

Considering the literatures of Preston tube calibration and accuracies (Head and Rechenberg 1962, Patel 1965, Bertelrud 1976, Kassab 1993 and Rhodes 2000), it is decided to calibrate the present flush-mounting Wall Shear Stress (WSS) sensor against a well calibrated Preston tube and to find a suitable validation with values given by Patel (1965).

2. Calibration of Preston Tube

It is assumed that close to the wall in a turbulent shear flow, there exists a region in which flow is substantially determined by the surface shear stress and the relevant properties of fluid, independent of the nature of outer flow field and quantities like pressure gradient and surface curvature. Boundary layer probe, while used along with a single wall static pressure tap is known as Preston tube (Fig. 1).

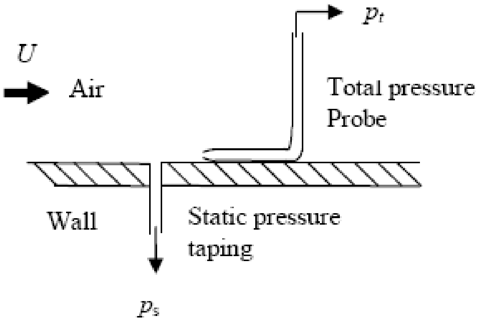

Fig 1. Schematic diagram of a Preston tube

The calibration of Preston tube is performed for the turbulent flow over a flat plate against a pre-calibrated Pitot-static tube, which is placed in front of an air-jet coming from a subsonic wind tunnel. Seven static pressure holes (of dia. 2 mm) equally spaced at 0.1m are drilled along the longitudinal mid-plane of the flat plate. At every hole, the Preston tube is traversed vertically by 0.5 mm height until the boundary layer limit is reached. Karman momentum integral equation is then used to calculate the value of shear stress. According to this equation, the shear stress on a flat plate with zero pressure gradient is given by

$$\tau=U^2\beta\frac{\partial}{\partial x}(\delta)-\delta^*\frac{\partial}{\partial x}(p_s) \qquad (1)$$

The experiment is performed for three free-stream velocities (U = 10, 15 and 20 m/s) measured upstream using a pre-calibrated telescopic Pitot-static tube connected to a digital micromanometer. For every free-stream velocity, velocity profiles at all seven stations are measured and subsequently graphs are plotted with ordinates as $(u/U)(1-u/U)$

and $(1-u/U)$, while the abscissa corresponds to the height measured from the flat plate. Area under these graphs represent momentum thickness (β) and displacement thickness (δ^*) respectively and the values are substituted in Eq. 2 to obtain the shear stress. Fig. 2 shows a calibration curve for the Preston tube as per the calibration Eq. 1. This is pertinent to note in Table 1 that the coefficients of best-fit calibration curve reported in Preston (1954) and NPL standard (1958) are closely matched with the present calibration curve as shown in Fig. 2.

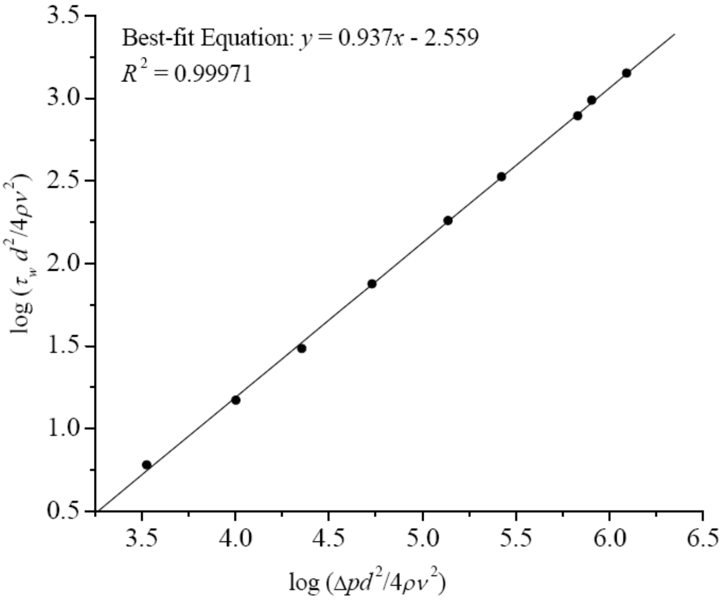

Fig 2. Calibration curve of Preston tube

Table 1 Coefficients for Linear regression: $y = Ax + B$

Author	*A*	*B*
Preston (1954)	0.875	–2.604
NPL (1958)	0.875	–2.647
Present study (2012)	0.937	–2.559

3. Calibration of Wall Shear Stress Sensor

In the present study, wall shear stress on a plat plate placed into the flow stream is measured using a Wall Shear Stress (WSS) sensor probe connected to a Constant Temperature Anemometer (CTA) system. This probe contains a resistive thin film sensor (Model: 55R46, Make: Dantec Dynamics A/S, Denmark) placed at the measuring locations (Fig. 3-a). The sensor is flush-mounted in a rigid boundary which is connected to a two-axis translation stage to adjust the vertical, *y*, and the longitudinal position, *x*, with sufficient accuracy (Fig. 3-b).

The sensor is calibrated using a pre-calibrated Preston tube. With the use of such pre-calibrated Preston tube, shear stress is now become a parameter that explicitly depends upon the value of dynamic pressure (Δp) at a point close to the wall and the height of the point of measurement (d) of dynamic pressure from the wall. For calibration of WSS sensor connected to a CTA system, voltage required to maintain a constant temperature is recorded at every measuring point (i.e. the seven stations on the flat plate) and corresponding values of dynamic pressure very near the wall is measured using the pre-calibrated Preston tube. Using the values of dynamic pressure measured by the Preston tube close to the wall and through its calibration curve (Fig. 2), corresponding shear stress is determined.

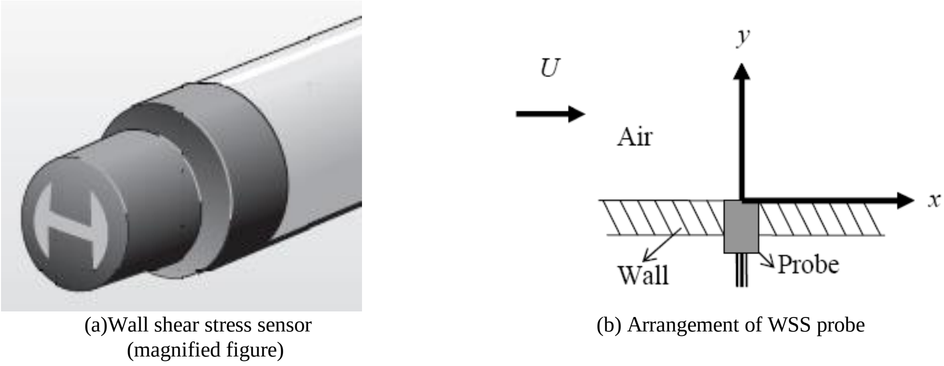

(a)Wall shear stress sensor (magnified figure)

(b) Arrangement of WSS probe

Fig. 3 Wall shear stress (WSS) sensor and its arrangement

Thus, two parameters are now correlated: the voltage required to maintain a constant temperature and the corresponding wall shear stress at that point. The process of deriving a relationship between wall shear stress and the voltage starts with the energy equation associated with the phenomena, and the relation between the voltage and the corresponding wall shear stress (τ_w) is given in Eq. 3:

$$E^2 = A\tau_w^{1/3} + B \tag{1}$$

Fig. 4 shows a plot between E^2 and $\tau_w^{1/3}$, the best-fit curve after regression analysis comes out to be a straight line, well in correlation to the analytically derived calibration equation, the constants *A* and *B* were the slope and the intercept of the best-fit curve respectively.

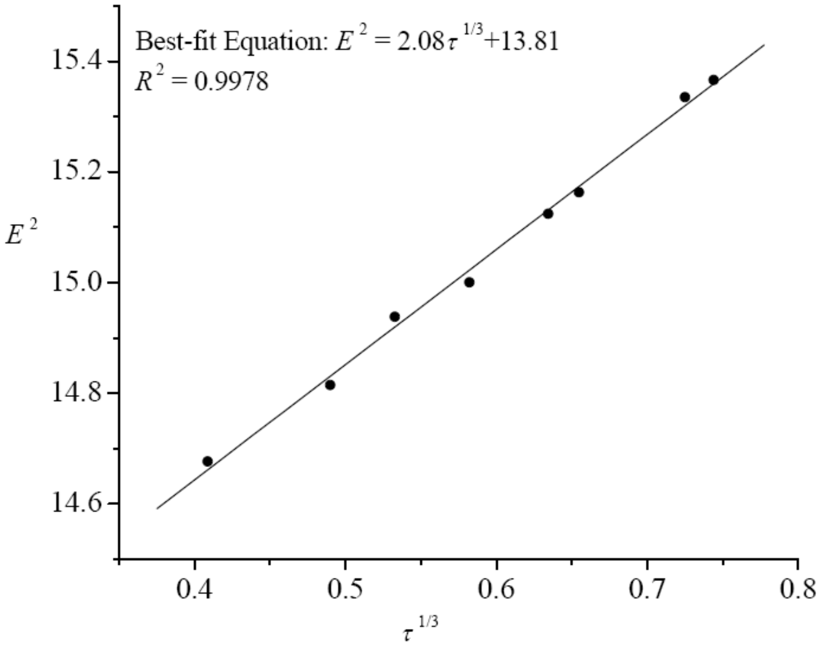

Fig. 4 Calibration curve for Wall shear sensor (WSS) probe

The results obtained are well matched with the expected equation of the calibration and the coefficients *A* and *B* are found as 2.08 and 13.81 respectively.

4. Computational Verification

Computational Fluid Dynamics (CFD) analysis is also carried out to see verify the measured velocity profiles and calculated wall shear stresses. Finite-volume technique based commercial CFD solver ‘Fluent 6.3’ is used for this purpose. Experimental velocity profile measured at the upstream of the flat plate is given as input in the computation. Grid generation is done using commercial mesh generation software ‘Gambit 2.3’, where quadratic elements are used with finer grids near the wall to capture boundary layer growth properly. Enhanced wall functions (Fluent user guide, 2006) include near-wall modelling method that combines a two-layer model with so-called ‘enhanced wall functions’. If the near-wall mesh is fine enough to be able to resolve the viscous sub-layer (typically with the first near-wall node placed at $y^+ = 1$), then the enhanced wall treatment will be identical to the traditional two-layer zonal model. The use of enhanced wall functions with proper grid size (as required in enhanced wall modelling) can give results with high accuracy in boundary layers. Hence an enhanced wall treatment is applied to the problem with grid size adjacent to wall as $y^+ = 1$ as shown in Fig. 5. The epoxy glass material plate is used in the experiment and the value of roughness factor is adjusted according in the computation.

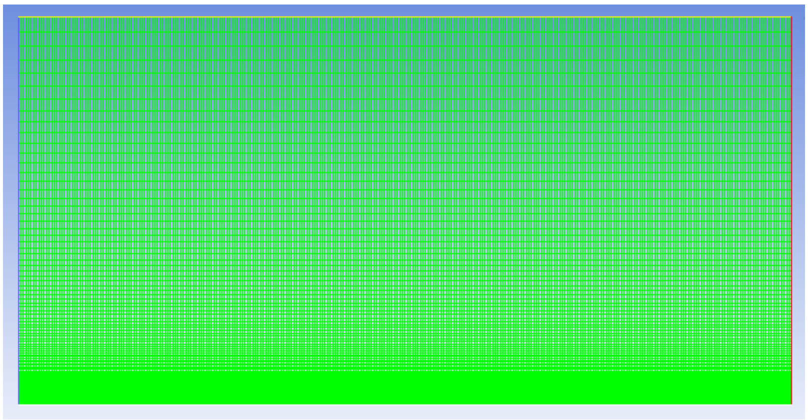

Fig. 5 Computation grid generation over a flat plate

The computation is carried out at all three free-stream velocities (i.e., U = 10, 15 and 20 m/s) and the results of velocity profile taken at the longitudinal mid-plane of the plate are shown in Fig. 6.

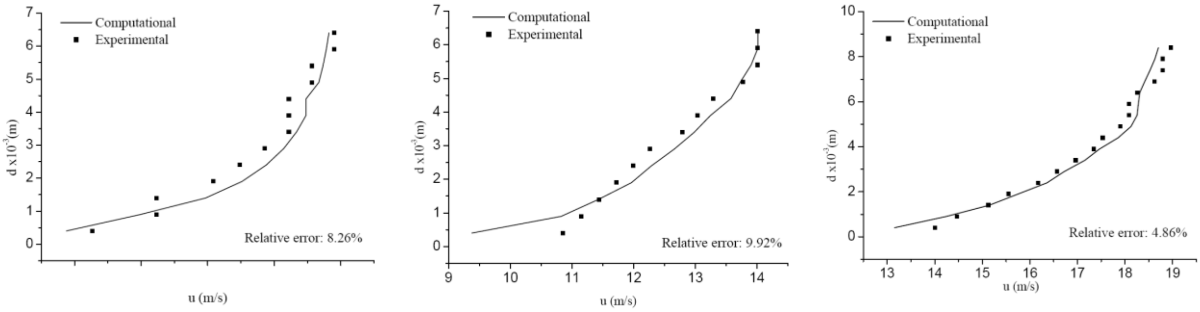

(a) U = 10 m/s (b) U = 15 m/s (c) U = 20 m/s

Fig. 6 Comparison of experimental and computational velocity profile over a flat plate

The values of wall shear stress are found in good correlation with the experimental values as given in Table 2.

Table 2 Comparison of wall shear stress (N/m^2) at different free-stream velocities

Free-stream velocity (U)	10 m/s	15 m/s	20 m/s
Experimental τ_w	0.0426	0.1045	0.2046
Computational τ_w	0.0392	0.0968	0.2108
Error	7.9%	7.3%	3.03%

5. Conclusions

The calibration of both Preston tube and flush-mounting WSS sensor probe is done and verified through computational analysis as well as the past results. The calibration coefficients obtained for the Preston tube is very close as found by Preston (1954) and NPL standard (1958). Hence the Preston tube calibration is verified.

The calibration result of WSS probe is well matched with the theoretical calibration equation and the calibration coefficients A and B are found as 2.082 and 13.81 respectively. Furthermore, the results from the computational analysis also suggest that the calibration obtained is accurate enough, since measurement of velocity profile and shear stress are in good agreement with the computational values. Hence the calibration methodology of WSS sensor probe as described in the study provides accurate and reliable results, and can be effectively used to measure wall shear stress in various flow applications.

References

[1].Bellhouse, B.J. and Schultz, D.L., 1968, Measurement of fluctuating skin friction in air with heated film gauges, Journal of Fluid Mechanics, vol. 32, part 4, pp. 675-680.
[2].Bertelrud, A., 1976, Preston tube calibration accuracy, AIAA Journal, vol. 14, no. 1, pp. 98-100.
[3].Fluent 6.3 User's guide, 2006, Ansys Inc., Lebanon, USA.
[4].Head, M.R., and Rechenberg, I., 1962, The Preston tube as a means of measuring skin friction, J. of Fluid Mechanics, vol. 14, no. 1, pp. 1-17.
[5].Kassab, S.Z., 1993, A Preston tube calibration chart, Review of Scientific Instruments, vol. 64, no. 1, pp. 253-256.
[6].National Physical Laboratory, 1958, On the measurement of local surface friction on a flat plate by means of Preston tubes, Rep. and Mem. No. 3185, Aerodynamics Division, U.K., pp. 1-24.
[7].Patel, V.C., 1965, Calibration of Preston tube and limitations of its use in pressure gradients", J. of Fluid Mechanics, vol. 23, no. 1, pp. 185-208.
[8].Preston, J.H., 1954, The determination of turbulent skin friction by means of pitot tubes, J. of Royal Aeronautical Society, vol. 58, pp. 109.
[9].Rhodes, D.G., and New, A.P., 2000, Preston tube measurements in low Reynolds number turbulent pipe flow, vol. 126, no. 6, pp. 407-415.

Available online at www.sciencedirect.com

SciVerse ScienceDirect

Procedia Engineering 00 (2012) 000–000

Procedia Engineering

www.elsevier.com/locate/procedia

5th BSME International Conference on Thermal Engineering

Experimental Observation of Boundary layer of the Turbulent flow over a Bluff Body inside Rectangular Diffuser

Siddhartha Bandyopadhyay*, Milan Krishna Singha Sarkar, Dr. Debasish Roy, Dr. Arunava Chanda

Jadavpur University, Kolkata, Pin 700032, India
IIT Guwahati, India

Abstract

The turbulent fluid flow with different velocity over a bluff body is important for the analysis and design of structure of high rise buildings as well as flow passage having flow obstruction. The main aim of present work is to investigate experimentally the flow field of air in a rectangular diffuser with different inlet velocity. From experimental results it has been found the displacement thickness and momentum thickness by numerical integration. The flow field considered is the field before and after the bluff body in a rectangular diffuser. The result also contained detailed velocity distributions, which have been investigated thoroughly in the direction normal to the test section at different axial positions. From the experimental results it is concluded that the boundary layer thickness is lower for higher inlet velocity. Displacement thickness is fluctuating at upstream and top of bluff body and at downstream it decreases with increase of inlet velocity. Momentum thickness decreases according to increase inlet velocity. The variation of momentum thickness is higher for high inlet velocity. Near the bluff body, momentum thickness decreases, which denotes maximum momentum transfer and as it becomes negative, it corresponds to recirculation zone. The recirculation length and height increases with increase inlet velocity.

Keywords: Bluff body; Turbulence; Re-circulation; Boundary layer; Displacement thickness; Momentum thickness.

Nomenclature

g	acceleration due to gravity (m/s^2)
h	difference of height of two points (m)
l_{stag}	stagnation pressure readings of the manometer (m)
l_{stat}	static pressure readings of the manometer (m)
n	No. of points
P_1	main scale reading of barometer
R	gas constant (kg-m/kg ^{0} k)
R_{eX}	Reynolds number
T	absolute temperature (^{0} k)
V.C.	vernier constant
V.S.	vernier scale reading
V	velocity of air at a particular height (m/s)
V_∞	maximum velocity of air (m/s)
w	specific weight of mercury (kg/m^3)
x	distance of the stations measured from the blower outlet end (m)
x_0	initial height (m)

---

* Corresponding Author: Email : sid_bandy62@yahoo.co.in

1.1. Experimental Set Up and Procedure

A complete description of the experimental set-up is shown below. The components of the set up are as follows

(i) Rectangular diffuser with 15^0 inclination in axial direction (ii) Blower with controlling system (iii) Bluff body of dimension 0.2×0.1×0.075m (iv) Inclined tube Manometer (v) Bevel Protractor (vi) Stagnation tube (vii) Hose pipe (viii) Sealing material (ix) Static tube (x) Scale (xi) Digital Velocity Meter (xii) DC Variac (xiii) Speed Sensor (xiv) Thermometer. Experiments have been carried out at 1000 RPM, 1500 RPM and 2000 RPM of blower speed.

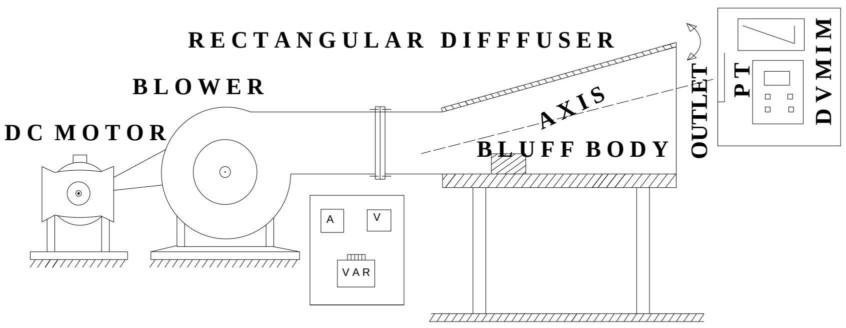

Fig. 1. Schematic diagram of experimental set-up

A blower with controlling system was connected at the inlet of a 15^0 inclined rectangular diffuser. A bluff body of 0.2x0.1x0.075m dimension, 0.24m from the inlet is set within the diffuser. Inclined tube manometer with 5^0 inclinations is connected to stagnation tube and static tube by a long hose pipe. The Manometric fluid used was kerosene and the measurements were taken in middle plane of the diffuser. Stagnation tube has been used to measure stagnation pressure and static tube was for static pressure. The upper wall of diffuser has holes throughout the axial length. The stagnation and static tube are set at different station by this hole. After entering the tube within diffuser through upper wall holes it is properly sealed by using sealing material. The heights at which a pitot tube has been raised are measured with a centimetre calibrated scale. The pressure has been read throughout the station. All the measurements have been taken at 1000 RPM, 1500 RPM and 2000 RPM of blower speed at nine different stations. Distances of stations from the blower end are chosen conveniently as 0.115m, 0.18m, 0.24m, 0.29m, 0.36 m, 0.48m, 0.725m, 1.185m and 1.39m respectively. The experiments were conducted very carefully with measurements taken for short times so that there are no appreciable changes in density of the air flowing through the diffuser.

To measure velocity of flow of air by stagnation tube and static tube we considered the equation

$$P_{stag} = \rho_{oil} \times g \times \sin\theta \times l_{stag} \tag{1}$$

$$P_{stat} = \rho_{oil} \times g \times \sin\theta \times l_{stat} \tag{2}$$

In the above equations P_{stag} and P_{stat} are the stagnation and static pressure respectively. ρ_{oil} is the density of Kerosene which is 800 kg/m^3.

Using Bernoulli’s Theorem, we get the velocity, which is

$$V = \sqrt{\frac{2\rho_{oil} g \sin\theta \left(l_{stag} - l_{stat}\right)}{\rho_{air}}} m/s \tag{3}$$

We found the term ρ_{air} which is density of air and it is found from equation (4)

$$\rho_{air} = \frac{(P + V.C \times V.S)2.54w}{R \times T \times 100} Kg/m^3 \tag{4}$$

Our main aim is to determine Displacement thickness and Momentum thickness. Reynolds no is an important parameter for this calculation and it can be obtained as

$$R_{eX} = \frac{\rho_{air} \times V \times x}{\mu_{air}} \tag{5}$$

Where μ_{air} is the viscosity of air.

For Numerical calculation of Displacement thickness and Momentum thickness we used one third Simpson rule [1].

$$\int_{x_0}^{x_0+nh} y\,dx = \frac{h}{3}(y_0 + 4y_1 + 2y_2 + 4y_3 + 2y_4 + \cdots\cdots + 2y_{n-2} + 4y_{n-1} + y_n) \tag{6}$$

For first six stations h=0.01m and for last three stations h=0.02m, x_0 is the initial height and n is the number of points.

For Displacement thickness $y = \int_0^\infty \left(1 - \frac{V}{V_\propto}\right) dy$

For Momentum thickness $y = \int_0^\infty \frac{V}{V_\propto}\left(1 - \frac{V}{V_\propto}\right) dy$

2. Results and Discussion

The velocity distributions in the rectangular diffuser along the mid plane of different heights are plotted for different stations. The velocity distributions are obtained at three different inlet velocity of the diffuser with 75 mm high bluff body and corresponding speeds of Blower are 1000RPM, 1500 RPM and 2000 RPM.

The following graphs are plotted from the data obtained from the performed experiments and they are shown below.

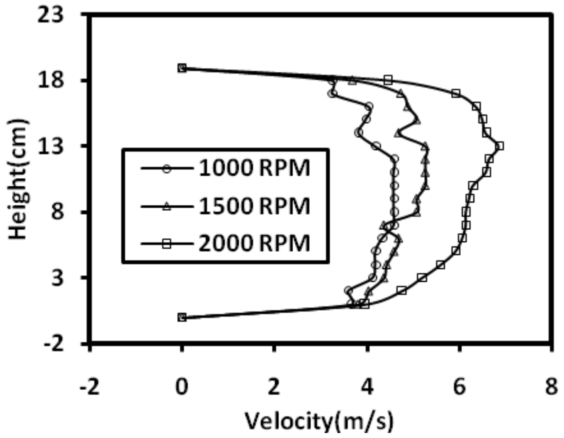

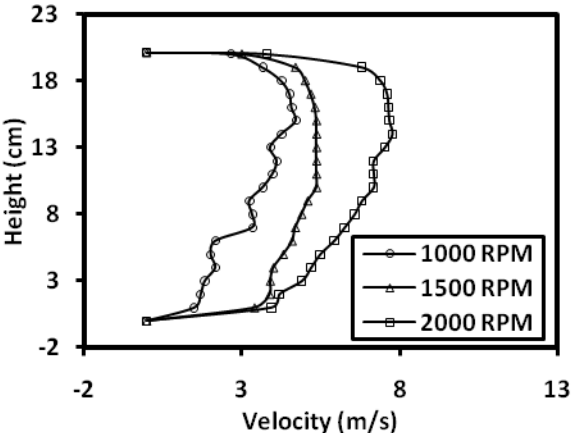

Fig. 2. Comparison of velocity distribution
at x=11.5cm for variable inlet velocity

Fig. 3. Comparison of velocity distribution
at x=18cm for variable inlet velocity

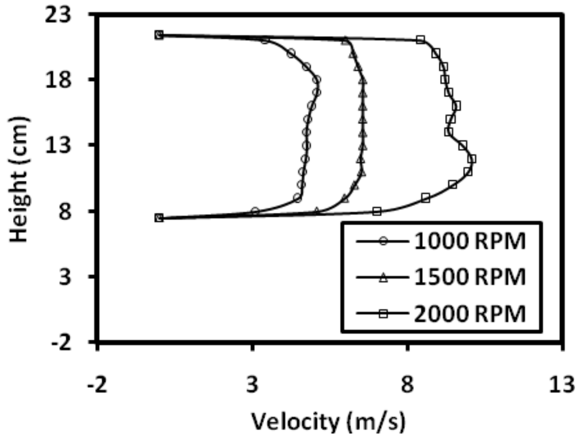

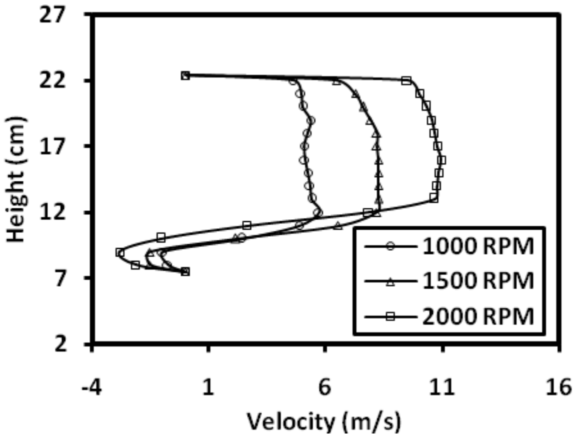

Fig. 4. Comparison of velocity distribution
at x=24cm for variable inlet velocity

Fig. 5. Comparison of velocity distribution
at x=29cm for variable inlet velocity

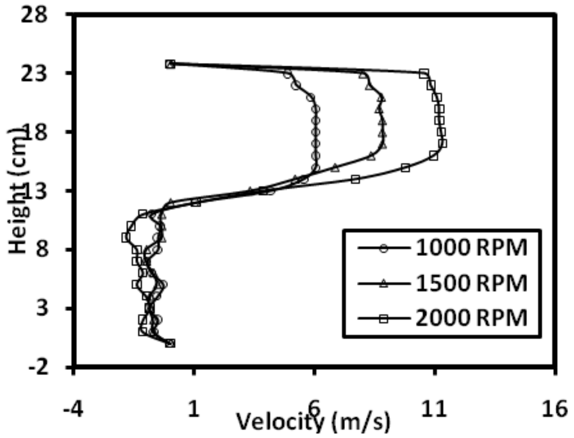

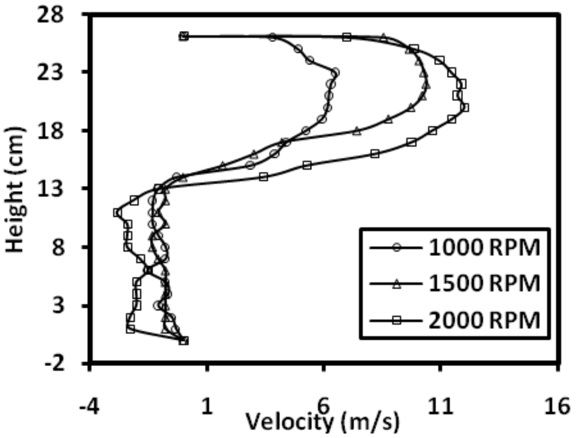

Fig. 6. Comparison of velocity distribution
at x=36cm for variable inlet velocity

Fig. 7. Comparison of velocity distribution
at x=48cm for variable inlet velocity

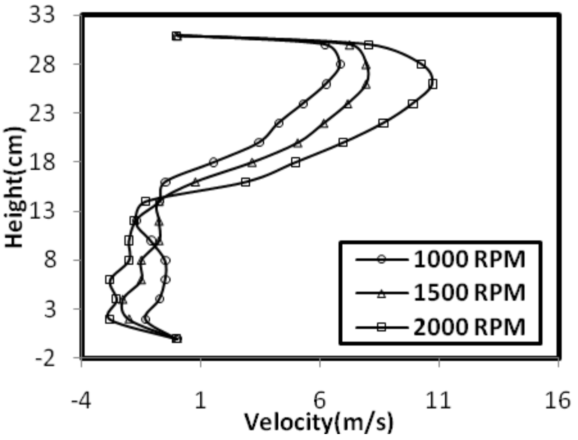

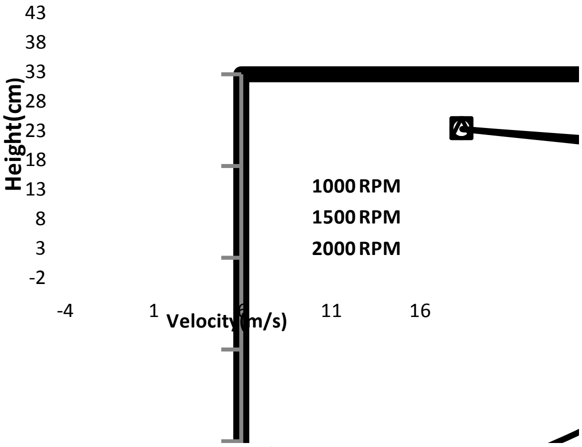

Fig. 8. Comparison of velocity distribution
at x=72.5cm for variable inlet velocity

Fig. 9. Comparison of velocity distribution
at x=118.5cm for variable inlet velocity

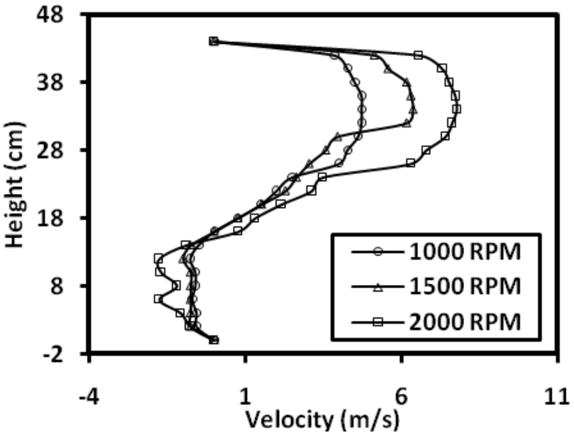

Fig. 10. Comparison of velocity distribution at x=139cm for variable inlet velocity

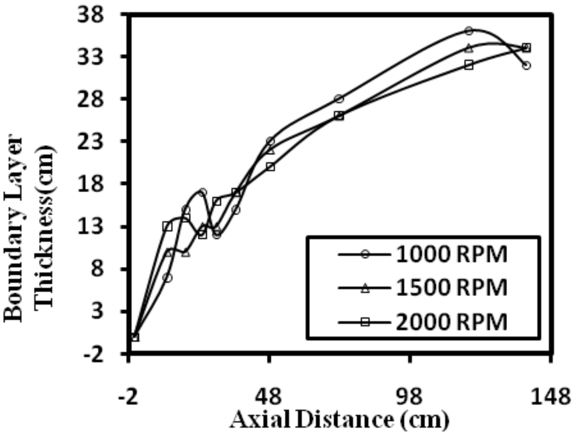

Fig. 11. Comparison of boundary layer thickness for variable inlet velocity

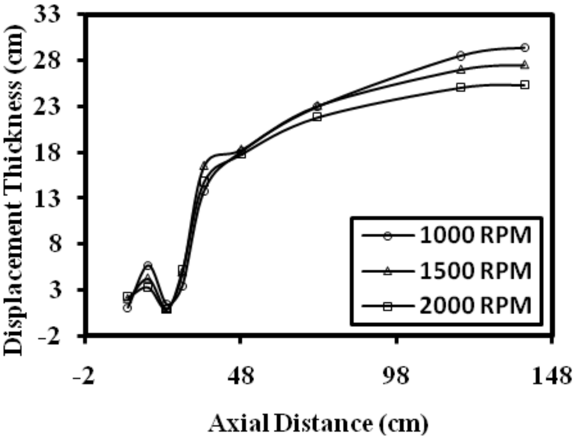

Fig. 12. Comparison of displacement thickness for different axial distances

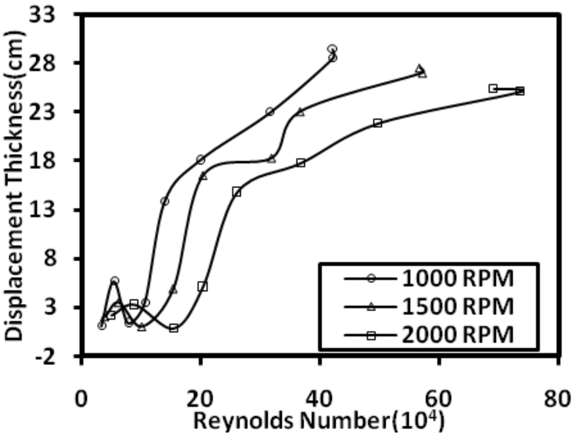

Fig. 13. Comparison of displacement thickness for different Reynolds number

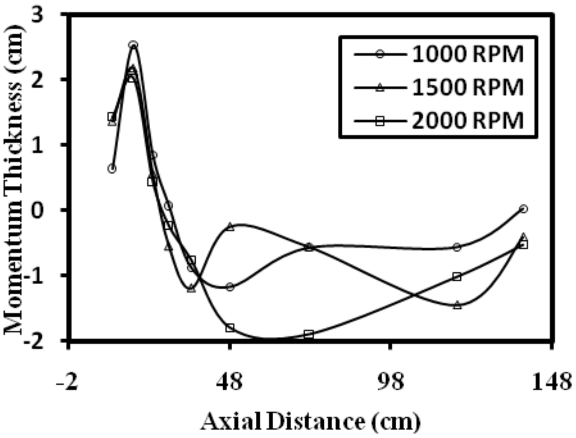

Fig. 14. Comparison of momentum thickness for different axial distances

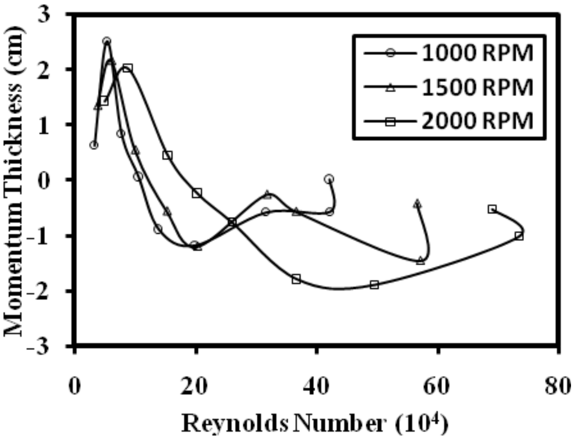

Fig. 15. Comparison of momentum thickness for different Reynolds number

Fig. 2. and Fig. 3. are indicate the comparison of velocity distribution at position x=0.115m and x=0.18m. Both stations are upstream of the bluff body. From the figure it is clear that no recirculation occurs for any speed. Velocity gradually increases according to the inlet velocity.

The station x=0.24m is the leading edge of the bluff body. The comparison of the velocity distribution at leading edge of the bluff body is shown in Fig. 4. In the leading edge of bluff body there is no recirculation.

The station x=0.29m is the midpoint of the bluff body. From Fig. 5. it is clear that the recirculation occurs above the bluff body and there is a recirculation zone. There is a stagnation point also above of the bluff body.

The stations for x=0.36m, x=0.48m, x=0.725m, x=1.185m and x=1.39m are at the downstream of the bluff body and corresponding comparison of velocity distribution shown in the figure 6 to figure 10. The lower portion of the all stations having recirculation of velocity. There is a recirculation zone present behind the bluff body. The recirculation zone is near to the lower wall. From the velocity comparison, the height and length of recirculation zone are higher for high inlet velocity and vice versa.

It is shown from Fig. 11. that upstream of the bluff body boundary layers increases according to inlet velocity of diffuser. At the top of bluff body boundary layer fluctuate more due to recirculation of flow. Downstream of bluff body, boundary layer is lower for higher inlet velocity and at outlet it is fluctuate for high turbulence.

Comparison of displacement thickness for different axial distance and Reynolds number are shown in Fig. 12. and Fig. 13. For both comparisons, displacement thickness fluctuates at upstream and top of the bluff body and at downstream it decreases with increase of inlet velocity.

Momentum thickness also fluctuate at upstream of the bluff body. From Fig. 14. and Fig. 15. it is observed that momentum thickness decreases according to increase inlet velocity. The variation of momentum thickness for 2000 RPM is higher, because of the presence of higher recirculation zone compared to other two speeds.

3. Conclusion

The objective of this study was an experimental investigation of the turbulent flow in a diffuser at the presence of bluff body. In this work the detail velocity distribution in the rectangular diffuser have been investigated thoroughly. The comparison of velocity distributions were made by using different inlet velocity with a fixed height bluff body.

From experimental and numerical results, the major conclusions are drawn as

1. For any inlet velocity, there is no recirculation at upstream of bluff body.
2. Recirculation is begin from top of the bluff body and its hold up to outlet of diffuser.
3. The reverse flow occurs near to the lower wall.
4. The maximum velocity occurs near to the upper wall.
5. Recirculation length and height increases with increase inlet velocity.
6. Boundary layer thickness is fluctuated near the bluff body. Downstream of bluff body boundary layer thickness is lower for higher inlet velocity.
7. Displacement thickness is more fluctuate at upstream and top of the bluff body and at downstream it is decreases with increases inlet velocity. For upstream of bluff body displacement thickness is lower for low height bluff body and for downstream of bluff body it is revised.
8. At the upstream of bluff body momentum thickness increases for all inlet velocity and just before of bluff body it rapidly decreases to zero. Again at downstream of bluff body it increases for all velocity and also increases for higher Reynolds number. The variation of momentum thickness is higher for high inlet velocity.

References

[1] B.S. Grewal, “Higher Engineering Mathematics”. 33rd Edition, Page No 966
[2] J. R. Fontaine et al. “Evaluation of air diffuser flow modelling methods experiments and computational fluid dynamics simulations”, Building and Environment 40 (2005) 377-389.
[3] L.A. M. Endres et al. “Wall Pressure Field in a tube bank after a baffle Plate”, Transactions of SMiRT 15-1 5th International Conference on Structural Mechanics in Reactor Technology, Seoul, 1999, Vol.7, pp262-275 .
[4] A. Mandal et al. “Experimental Investigation of Recirculatory Turbulent Flow Past Twin Obstructions of Different Height Placed at Different Stations of a Rectangular Diffuser”. December 16-18, 2010, IIT Madras, Chennai, IndiaFMFP2010 Paper ID 440
[5] P. W. Bearman et al. “Effect of Free Stream Turbulence on The Flow Around Bluff Bodies”, Department of Aeronautics, Imperial College, London. Volume 20, Issues 2–3, 1983, Pages 97–123
[6] A. Mandal et al. “Experimental Analysis of the Turbulent Fluid Flow through a Rectangular Diffuser using Baffles”, Proceedings of National Conference on Recent Advances in Fluid & Solid Mechanics(RAF&SM-10), Dept. of Civil Engg., NIT, Rourkela, India, pp 238-242.

[7] M. N. Noui-Mehidi et al. “Velocity Distribution in an Asymmetric Diffuser with Perforated Plates”, Proceedings of 15th Australasian Fluid Mechanics Conference, the University of Sydney,Australia, 13–17 December 2004

[8] G.M.R. Van Raemdonck et.al.,”Time-Averaged Phenomenological Investigation of a Wake Behind A Bluff Body “, BBAA VI International Colloquium on: Bluff Bodies Aerodynamics & Applications Milano, Italy, July, 20–24 2008

[9] B. S. Massey. Mechanics of Fluids.Fourth edition.

Available online at www.sciencedirect.com

SciVerse ScienceDirect

Procedia Engineering 00 (2012) 000–000

Procedia Engineering

www.elsevier.com/locate/procedia

5th BSME International Conference on Thermal Engineering

Steady Laminar Boundary Layer Flow Over An Impulsively Stretching Surface Enclosed By Strong Magnetic Field

M. ferdows[a*]

[a]Department of Mathematics, University of Dhaka, Dhaka-1000, Bangladesh.

Abstract

The problem of steady incompressible and laminar boundary layer flow over an impulsively stretching surface embedded a strong magnetic field of an electrically conducting Newtonian fluid in the presence of induced magnetic field has been studied. The resulting nonlinear coupled ODE's are solved numerically through the use of Maple software. The solutions is found to be dependent on three governing parameters including the magnetic field parameter M, the magnetic force number β, and the receiprocal of the magnetic prandtl number λ. Representative velocity and induced magnetic field function profiles within the boundary conditions are presented at selected values of the parameters. To our best knowledge there has been no study and for this we cannot compare our method with any other numerical or experimental work.

Keywords: boundary layer, stretching surface, strong magnetic field, magnetic induction, similarity analysis

---

[a]* Corresponding author. Tel.: +8801720809796; fax: +0-000-000-0000 .
E-mail address: ferdows@du.ac.bd

Nomenclature

u, v	Velocity components along x and y directions
H_1, H_2	Induced magnetic field components along x, y directions
H_0	Uniform magnetic field
B	Magnetic induction
f'	Dimensionless velocity
g'	Induced magnetic field function
M	Magnetic field parameter
U	Surface velocity along the wall
ρ	Density of the fluid
η	Similarity variable
μ_0	Magnetic permeability
ν	Kinematic viscosity
σ	Electric conductivity
Ψ	Stream function
ϕ	Magnetic Stream function
α_1	Magnetic diffusivity
β	Magnetic force number
λ	Reciprocal of the Magnetic prandtl number

1. Introduction

In recent years, MHD flow problems have become more important industrially. As many natural phenomena and engineering problems are worth being subjected to MHD analysis for instance the effects of radiation and hall current on a MHD free convection flow past a semi-infinite flat plate with an aligned magnetic field has been reported in [1]. Induced magnetic field effects intransient laminar hydromagnetic boundary layer convection along an impulsively-started semi infinite flat plate with aligned magnetic field was reported in [2]. The steady boundary layer flow of a conducting fluid past a body in an aligned magnetic field was made by [3]. Non similar, laminar, steady, electrically conducting forced convection liquid metal boundary layer flow with induced magnetic field effects has been studied by [4].

In light of the above studies, our aim of this paper is to study the steady fluid flow in the presence of a induced magnetic field by similarity solution and is solved by MAPLE-13 [5]. A solution for the velocity and induced magnetic field profiles are obtained.

2. Governing Equations and similarity solution

Let us consider a steady, laminar, incompressible, viscous electrically conducting fluid over a linearly stretched surface assuming to be electrically non- conducting. The surface is at rest in an unbounded quiescent fluid and suddenly stretched with velocity $U = ax$ along the leading edge of the surface. The magnetic field H_0 is applied perpendicular to the stretching surface and the effect of the induced magnetic field is taken into account. The magnetic Reynolds number is taken large enough so that we can consider induced magnetic field effects. Following the induced magnetic field vector$\vec{H}=(H_1,H_2)$. The normal component of the induced magnetic field, H_2 vanishes at the surface with the parallel Components, H_1approaching the imposed magnetic field value , H_1 at the edge of the boundary condition. Governing equations for flow in the stretching surface with the momentum equation & magnetic equation are given as:

$$\frac{\partial u}{\partial x}+\frac{\partial v}{\partial y}=0\ ,\ \frac{\partial H_1}{\partial x}+\frac{\partial H_2}{\partial y}=0 \qquad (1)$$

$$u\frac{\partial u}{\partial x}+v\frac{\partial u}{\partial y}=\upsilon\frac{\partial^2 u}{\partial y^2}+\frac{\mu_0}{\rho}\left[H_1\frac{\partial H_1}{\partial x}+H_2\frac{\partial H_1}{\partial y}\right]-\frac{\sigma B^2(x)}{\rho}u \qquad (2)$$

$$u\frac{\partial H_1}{\partial x}+v\frac{\partial H_1}{\partial y}-H_1\frac{\partial u}{\partial x}-H_2\frac{\partial u}{\partial y}=\alpha_1\frac{\partial^2 H_1}{\partial y^2} \qquad (3)$$

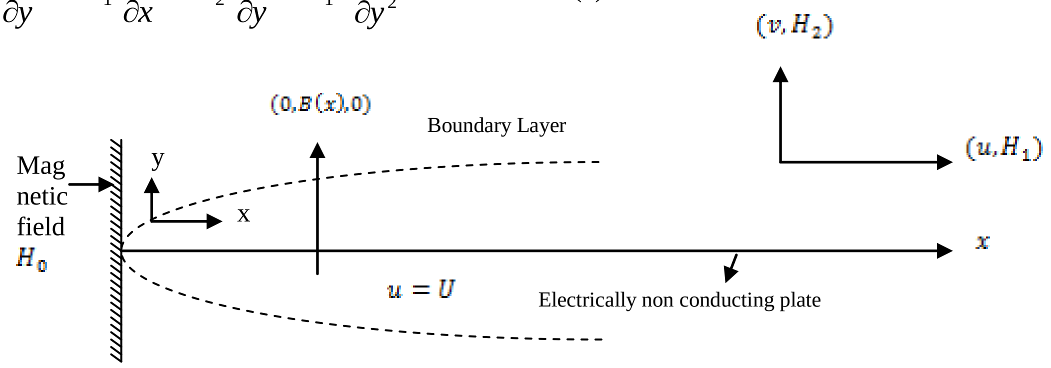

Physical model and coordinate system

Subject to the boundary conditions

$$y=0: u(x,y)=U=ax,\ v(x,y)=0,\ \frac{\partial H_1}{\partial y}=H_2=0$$

$$y\to\infty:\ u(x,y)\to 0,\ H_1\to H$$

To solve the equations (1-3) subject to boundary conditions (4) we introduce the following boundary layer similarity variables

$$\eta=\left(\frac{a}{v}\right)^{\frac{1}{2}}y,\ \psi(x,y)=\left(\frac{a}{v}\right)^{\frac{1}{2}}xf(\eta),\ \phi(x,y)=H_0\left(\frac{v}{a}\right)^{\frac{1}{2}}xg(\eta),\ \text{H}=H_0x \qquad (5)$$

Where $u=\frac{\partial\psi}{\partial y},\ v=-\frac{\partial\psi}{\partial x},\quad H_1=\frac{\partial\phi}{\partial y},\ H_2=-\frac{\partial\phi}{\partial x}$

Substituting equation (6) into (3-4) and after manipulation, we get

$$f'''+ff''-(f')^2-Mf'+\beta\left[g'^2-gg''\right]=0 \quad (6); \qquad \lambda g'''+fg''-gf''=0 \quad (7)$$

Where M=$\frac{\sigma B^2(x)}{\rho a}$ is the magnetic parameter, $\beta=\frac{\mu_0}{\rho}\frac{H_0{}^2}{a^2}$ is the magnetic force parameter, $\lambda=\frac{\alpha_1}{v}$,is the receiprocal of the magnetic prandtl number . Now the boundary conditions (4) becomes

$$\eta=0:\ f=0,\ f'=1,\ g=0,\ g''=0$$
$$\eta\to\infty:\ f'=0,\ g'=1 \qquad (8)$$

3. Result and discussions

The solution to the system of transformed governing equations and boundary conditions (6-8) was accomplished through the use of Maple-13. Over a range of magnetic field parameter M=5 to 50, due to strong magnetic field, note that there we do not consider any certain range of strong and weak magnetic field , magnetic force number β =0.01,0.3,0.9 and receiprocal of the magnetic prandtl number λ =0.1,0.5,5 as in [1] .Velocity profiles f' and magnetic field profiles g' are shown in figures (1-6) vary with the above parameters.

Figure (1) shows the resulting dimensionless velocity profiles $f'(\eta)$ as a function of similarity variable η for different values of the magnetic force number β. Considering strong magnetic field it is seen that the presence of β causes higher induction to the fluid which enchanced the velocity. It is evident from this simulation that the B.C. $f'(0) = 1$ is satisfied.

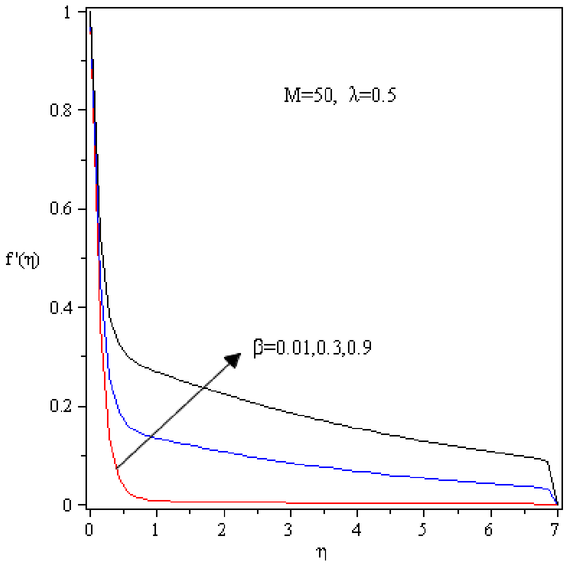

Fig 1: velocity profiles for various β

The induced magnetic field profiles $g'(\eta)$ for various value of the magnetic force number β is shown in fig.(2) with strong magnetic field. It is observe that $g'(\eta)$ decreases with η and starts increasing at $\eta_{app} = 6$ from the leading edge and become zero far away from the surface. This is because the highest Lorentz force which opposes the fluid motion.

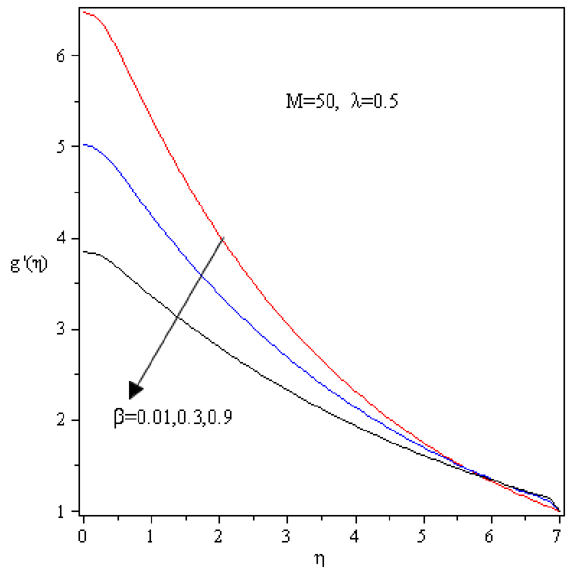

Fig 2: Induced magnetic field various β

The velocity profiles for different values of the receiprocal of the magnetic prandtl number λ presented in Fig.(3). It is observed that the velocity continuously decreases with η and become zero far away from the surface. With increasing λ which results in decreasing manner of the momentum boundary layer thickness is also observe that lower λ leads to induced more flow than higher λ.

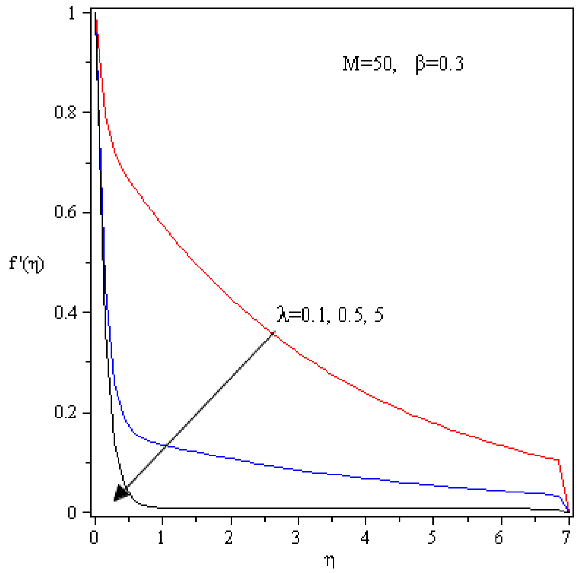

Fig 3: velocity profiles for various λ

Figure(4) show the effect of different values of the receiprocal of the magnetic prandtl number λ on the induced magnetic field profiles $g'(\eta)$for the values of the magnetic field parameter M=50 and values of magnetic force number β=0.3 . The induced magnetic field profiles $g'(\eta)$ deccreases with the increasing of the values of the receiprocal of the magnetic prandtl number λ. With an increase of the receiprocal of the magnetic prandtl number λ, a pattern which is intensified with decreasing distance along the plate, i.e. η-coordinate.It is observed from this profiles that the effect of λ is more pronounced on $g'(\eta)$ because λ occurs in the equation for the induced magnetic field. At higher λ, the flow has almost constant behavior satisfy the B.C.'s. It is interesting to note that the system is found to be unstable at higher λ. i.e. the boundary layer thickness $\delta_{app} \to 0$.

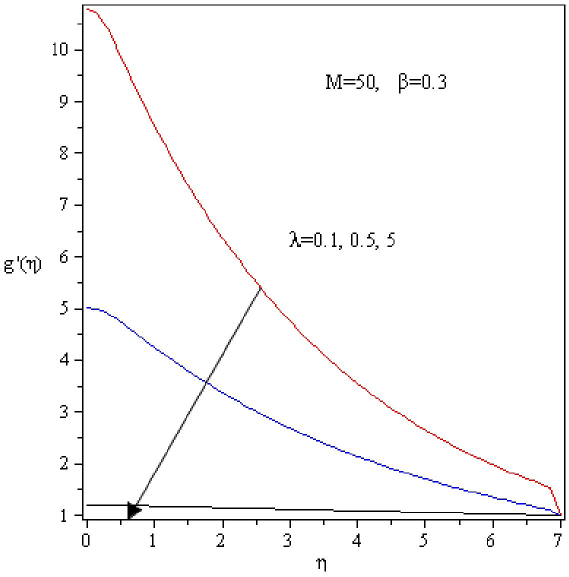

Fig 4: Induced magnetic field various λ

Figure(5) depicts the velocity profiles $f'(\eta)$ against η taking different values of magnetic parameter. It is seen that the effect of increasing magnetic parameter decrease the velocity.

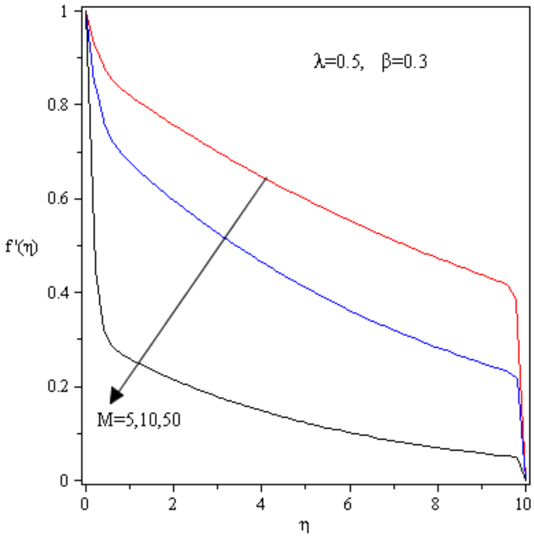

Fig 5: velocity profiles for various M

Figure(6) depicts the induced magnetic field profiles $g'(\eta)$ against η taking different values of magnetic parameter. It is reported that the effect of increasing magnetic parameter is to increase the induced magnetic profiles which signifies that the velocity is higher for strong magnetic field. Furthermore, it is observed that the Lorentz force becoming higher. i.e. decrease the magnetic profiles. Separation of flow is detected near $\eta_{app} = 5.$ This may be due to higher Lorentz force effects.

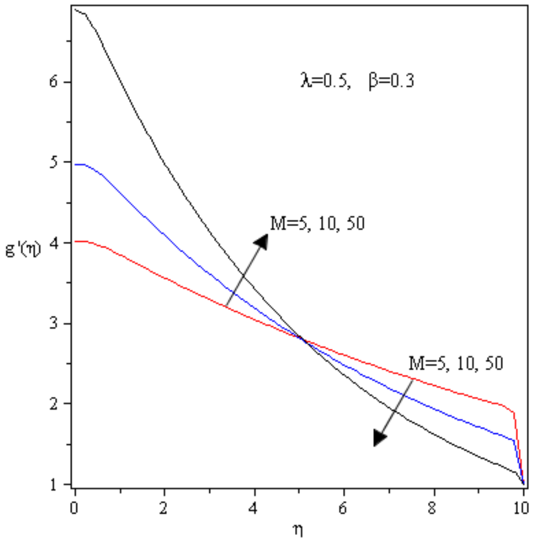

Fig 6: Induced magnetic field various M

4. Conclusions

It has been shown that

(1) The velocity profiles $f'(\eta)$ increases and the induced magnetic field profiles $g'(\eta)$ decreases as the magnetic force number β increases.
(2)Both the velocity profiles $f'(\eta)$ and the induced magnetic field profiles $g'(\eta)$ decreases as the receiprocal of the magnetic prandtl number λ increases.
(3) The velocity profiles $f'(\eta)$ decreases with the the increasing of the magnetic field parameter M . but the induced magnetic field profiles $g'(\eta)$ first increases and then decreases with the the increasing of the magnetic field parameter M. We have found cross flow at certain similarity variable $\eta_{app} = 5.$

References

[1]Seddeek MA., 2001. Effects of Radiation and Hall Current on a MHD Free Convection Flow Past a Semi –Infinite Flat Plate With an Aligned Magnetic Field. Proceedings of the Mathematical Society of Egypt, 76 p. 143.

[2] Takhar HS, Chamkh AJ and Nath G., 1999. Unsteady flow and heat transfer on a semi-infinite flat plate with an aligned magnetic field. International Journal of Engineering Science 37 p.1723.

[3] Glauert MB., 1964. On magnetohydrodynamic flows with aligned magnetic fields. Journal of fluid mechanics 19 p. 49.

[4]Anwar Beg, Bakir AY, Prasad VR and Ghosh SK., 2009. Non-similar laminar steady electrically-conducting forced convection liquid metal boundary layer flow with induced magnetic field effects. International Journal of Thermal Sciences 48 p. 1596.

[5] A. Aziz, 2006. Heat conduction with Maple, Edwards Inc, USA.

Available online at www.sciencedirect.com

SciVerse ScienceDirect

Procedia Engineering 00 (2012) 000–000

Procedia Engineering

www.elsevier.com/locate/procedia

5th BSME International Conference on Thermal Engineering

Numerical Prediction of Wave-making Resistance of Pentamaran in Unbounded Water Using a Surface Panel method

Md. Shahjada Tarafder[a], Mir Tareque Ali[a], Md. Shahriar Nizam[b],

[a]*BUET, Dhaka-1000, Bangladesh*
[b]*Three Angle Marine Limited, Dhaka-1000, Bangladesh*

Abstract

This paper investigates the analysis of potential flow around the pentamaran hull moving with a uniform velocity in unbounded water using a surface panel method. The free surface boundary condition is linearized by the systematic method of perturbation in terms of a small parameter. The surfaces are discretized into flat quadrilateral elements and the influence coefficients are calculated by Morino's analytical formula. Dawson's upstream finite difference operator is used in order to satisfy the radiation condition. The pressure Kutta condition is imposed at the trailing edge of the lifting body to determine the dipole distribution, which generates required circulation on the lifting part. The effect of the hull stagger on the wave making resistance of the pentamaran hull is analyzed.

Keywords: Resistance, Panel method, Kelvin free surface condition, Pressure kutta condition, Pentamaran

---

Nomenclature

C_W	wave- making coefficient
g	acceleration due to gravity
K_0	wave number
n	unit normal vector on the surface
S_F	free surface
S_H	hull surface
S_∞	surface of a hemisphere
U	uniform velocity in the positive x-direction
Greek symbols	
Φ	total velocity potential
ε	perturbation parameter
ϕ	perturbation velocity potential due to uniform flow
ϕ_1	first order perturbation velocity potential
ϕ_2	second order contributory part for perturbation velocity potential
ζ	wave elevation
ζ_1	first order wave elevation
ζ_2	second order contributory part for wave elevation

1. Introduction

The increasing demand for fast sea transportation has led till now to a significant growth of interest in multi-hull ships for coastal areas, where at present the catamaran seems the leading commercial type. Recently new unconventional larger multi hull crafts have been proposed, the study and the development of such hull-forms is aimed both at reducing the high fuel consumption inevitably linked to the higher speeds of monohull ships and at achieving the advantages of larger deck areas.

The pentamaran seems interesting possibilities due to the benefits given by their very slender hull forms compared to the conventional multi hull ships at various medium-high speeds. However, except catamaran, trimaran ships have had a limited use till now and there is very little information about pentamaran hull forms and configurations. Besides, it is necessary a comparison of the hydrodynamic characteristic for the various configurations of pentamaran hull as well as the other different high speed vessels.

The multihull vessel is composed of main hull with two or more small outriggers and has a wide range of choices for reducing the wave-making resistance by exploiting arrangements of the hull elements and varying hull forms. This multihull resistance presents a complex phenomenon for the ship designer as the interference effects must be considered in addition to the resistance of the demihulls in isolation.

In the field of ship hydrodynamics, the first theoretical solution for the problem of wave resistance was given by Michell [1] for a thin ship moving on the surface of an inviscid fluid. The solution is the well-known Michell Integral based on the double Fourier transformation of the velocity potential. Later on Kelvin [2] established the fundamental theory of ship waves. Since then many theoretical studies in ship hydrodynamics have been undertaken. Havelock [3] studied the effects of shallow water on the wave resistance and wave pattern for a point pressure impulse traveling over a free surface.

Peng [4] presented a numerical method based on Michell’s theory for the resistance in calm water and for the sea keeping performance in waves of multihull of various configurations at an infinite depth of water. The problem is solved by the boundary element method in terms of the Green function.

Moraes et al [5] investigated the wave resistance component of high speed catamarans and the effects of shallow water on these wave resistance components. Two methods were applied: the slender body theory proposed by Michell and a 3D method used by Shipflow software. Results were obtained for different types of twin hulls and attention was given to the effects of catamaran hull spacing.

Yeung [6] provided a general expression for calculating the interference resistance of multihull in a simple integral. This expression contains the explicit effects of stagger and separation in where it requires only the knowledge of the Kochin functions of each of the interacting hulls.

Begovic et al. [7] carried out an experimental research at Naples University towing tank by model test of a pentamaran hull for a ship to be used on medium distance Mediterranean routes. The main hull was slender round bilge hull forms from Series 64 and the very slender outrigger hull forms are also from Series 64. The isolated main hull, the isolated outriggers and the whole pentamaran hull in different configurations were tested in calm water in order to evaluate the hydrodynamic characteristics and powering performances.

Tarafder and Suzuki [8] investigated the influence of the water depth and the wave interference effects on the first and second order wave making resistance of the catamaran hull using a potential based boundary element method. The effects of hull separation and water depth on the hydrodynamic characteristics of the catamaran hull were analyzed and the validity of the computer scheme was examined by comparing the wave resistance with others’ numerical results.

Wang [9] developed a 3D Rankine source panel method for calculating the linear wave-making resistance of a trimaran with Wigley hulls. Non uniform rational B-spline (NURBS) was adopted to represent body surface and to calculate the normal vector and derivative vectors of the NURBS surface. The radiation condition was satisfied using the numerical technique of staggered grids.

Aubault and Yeung [10] provided a brief description of a formulation for the interference wave resistance between two or more hulls in finite-depth waters, using a distribution of Havelock sources over the hulls. The formulation was based on thin ship approximation.

The aim of the present paper is to draw a mathematical model for computing the potential flow around pentamaran hulls moving with a uniform speed in unbounded water and to compute the wave-making resistance, wave profile and wave pattern at various speeds.

2. Mathematical Modeling of the Problem

Consider a ship moving with a constant speed U in the direction of the negative x-axis. The z-axis is vertically upwards and the y-axis extends to starboard. The origin of the co-ordinate system is located in an undisturbed free surface at amidship, so that the undisturbed incident flow appears to be a streaming flow in the positive-x direction. The fluid is assumed to be incompressible and inviscid where the flow is irrotational. The velocity potential Φ and wave elevation ζ can be expressed as

$$\begin{aligned} \Phi &= Ux + \phi = Ux + \sum_{n=1}^{\infty} \varepsilon^n \phi_n \\ \zeta &= \sum_{n=1}^{\infty} \varepsilon^n \zeta_n \end{aligned} \tag{1}$$

where, ε (ε<<1) is a perturbation parameter and is defined by B/L. B and L are the breadth and the length of the ship respectively. ϕ is the perturbation velocity potential due to the existence of the hull. The velocity potential Φ satisfies the Laplace equation

$$\begin{aligned} &\nabla^2 \Phi = 0 \\ &\nabla^2 (Ux + \phi) = 0 \text{ in the fluid domain V} \\ &\nabla^2 \phi = 0 \end{aligned} \tag{2}$$

The fluid domain V is bounded by the hull surface S_H, free surface S_F and the surface of a hemisphere S_∞ of infinite radius. Now the problem can be constructed by specifying the following boundary conditions as follows:

(i) *Hull boundary condition* : The normal component of the velocity on the hull surface must be zero. So the boundary conditions for the first and second order approximations can be written from Equation (1) as

$$\begin{aligned} &\varepsilon: \ \nabla\phi_1 \cdot n = -Un_x \\ &\varepsilon^2: \nabla\phi_2 \cdot n = 0 \end{aligned} \tag{3}$$

in which $n = n_x i + n_y j + n_z k$ denotes the unit normal vector on the surface and is positive into the fluid.

(ii) *Free surface condition*: The kinematic and dynamic boundary conditions on the free surface can be written as:

$$\Phi_x \zeta_x + \Phi_y \zeta_y - \Phi_z = 0 \qquad \text{at} \quad z = \zeta \tag{4}$$

$$g\zeta + \frac{1}{2}(\nabla\Phi \cdot \nabla\Phi - U^2) = 0 \qquad \text{at} \quad z = \zeta \tag{5}$$

Combining Equations (4) and (5) we get

$$\nabla\Phi.\nabla\left[\frac{1}{2}(\nabla\Phi \cdot \nabla\Phi)\right] + g\Phi_z = 0 \ \text{ at } \ z = \zeta \tag{6}$$

The free surface boundary condition (6) is nonlinear in nature and should be satisfied on the actual surface, which is unknown and can be linearized as a part of the solution using the perturbation method. Substituting Equation (1) into Equation (6) and expanding the potential ϕ in a Taylor series about the mean free surface z = 0 the following first and second order free surface boundary conditions can be obtained as

$$\left.\begin{aligned} &\varepsilon \ : \ \ \phi_{1xx} + K_0 \phi_{1z} = 0 \\ &\varepsilon^2 : \ \ \phi_{2xx} + K_0 \phi_{2z} = R_2 \end{aligned}\right\} \quad \text{at} \quad z = 0 \tag{7}$$

where, K_0 (= g/U^2) is the wave number and

$$R_2 = -\frac{1}{U}\frac{\partial}{\partial x}\left(\phi_{1x}^2 + \phi_{1y}^2 + \phi_{1z}^2\right) - \zeta_1 \frac{\partial}{\partial z}\left(\phi_{1xx} + K_0 \phi_{1z}\right)$$

(iii) The wake surface S_w is assumed to have zero thickness. The pressure jump across S_w is zero, while a jump in the potential is allowed.

$$(\Delta p)_{\text{on } S_w} = p^+ - p^- = 0$$

$$\Delta\left(\frac{\partial\phi}{\partial n}\right)_{\text{on } S_W} = \left(\frac{\partial\phi}{\partial n}\right)^{+} - \left(\frac{\partial\phi}{\partial n}\right)^{-} = 0$$

(iv) For the steady lifting problem, the potential jump across the wake surface is the same as the circulation around the body and is constant in the stream wise direction.

$$(\Delta\phi)_{\text{on } S_W} = \phi^{+} - \phi^{-} = \Gamma$$

A Kutta condition is required at the trailing edge to uniquely specify the circulation. In its most general form, it states that the flow velocity at the trailing edge remains bounded.

$$|\nabla\phi|_{TE} < \infty$$

(v) Radiation condition: It is necessary to impose a condition to ensure that the free surface waves vanish upstream of the disturbance.

3. Wave profile and Resistance

The first and second order contribution to the linearized equation of wave profile can be obtained by Taylor's series expansion from Equations (1) and (5) as

$$\zeta_1 = -\frac{U}{g}\phi_{1x} \tag{8}$$

$$\zeta_2 = -\frac{U}{g}\phi_{2x} - \frac{U}{g}\zeta_1\phi_{1xz} - \frac{1}{2g}\left(\phi_{1x}^2 + \phi_{1y}^2 + \phi_{1z}^2\right) \tag{9}$$

Now the linearized equation of the second order wave profile can be written as

$$\zeta = \zeta_1 + \zeta_2 \tag{10}$$

After calculating the fluid velocity $\nabla\Phi$ on the control points on the hull surface the pressure co-efficient can be evaluated as:

$$C_p = 1 - \left(\frac{\nabla\Phi}{U}\right)^2$$

$\nabla\Phi = U + \nabla\phi_1$ for first order approximation

$\nabla\Phi = U + \nabla\phi_1 + \nabla\phi_2$ for second order approximation

Now including the waterline integral the wave- making coefficient can be obtained as

$$C_w = -\frac{\sum_{i=1}^{N_H} C_p n_x \Delta S}{\sum_{i=1}^{N_H} \Delta S} - \frac{\rho g \oint_{WL} \zeta^2 n_x dl}{\rho S U^2} \tag{11}$$

where, ΔS denotes the area of a panel on the hull surface.

4. Result and Discussion

The numerical algorithms outlined in the preceding section have been applied to various configurations of pentamaran in order to analyze the hydrodynamic characteristics at various speeds. The selected multihull ships are composed of Wigley hull and the equation of this mathematical hull surface is as follows:

$$y = \frac{1}{2}B\left(1-\frac{4x^2}{L^2}\right)\left(1-\frac{z^2}{T^2}\right)$$

where , L, B and T are the vessel length, width and draft respectively. A pentamaran is composed of the central main hull being two times longer than the outriggers. They all have the dimensions of L/B = 10 and B/T = 1.6. The stagger L_x is defined as the longitudinal distance between midsection of the central main hull and the outriggers, positive for outriggers towards the stern. The spacing L_y is defined as the lateral distance between the center plane of the main hull and that of the outriggers. These two parameters are symmetrically varied which is defined in Table 1.

Table 1. Various configurations of Wigley pentamaran

	Case 1		Case 2		Case 3		Case 4		Case 5	
	L_X	L_Y	L_X	L_Y	L_X	L_Y	L_X	L_Y	L_X	L_Y
Main hull	0.0	0.0	0.0	0.0	0.0	0.0	0.0	0.0	0.0	0.0
Outrigger 1	-0.25	-0.2	-0.125	-0.2	-0.25	-0.2	0.0	-0.2	0.0	-0.2
Outrigger 2	-0.25	0.2	-0.125	0.2	-0.25	0.2	0.0	0.2	0.0	0.2
Outrigger 3	0.25	-0.4	0.125	-0.4	0.0	-0.4	0.125	-0.4	0.0	-0.4
Outrigger 4	0.25	0.4	0.125	0.4	0.0	0.4	0.125	0.4	0.0	0.4

The paneled region of the free surface is extended about 1.5 of the ship length upstream, 3.0 of the ship length downstream from the body and 1.8 of the ship length sideward of the ship. Due to the symmetry, only a half of the pentamaran and free surface is taken into account in the computation scheme. The effect of the remaining half of the computational domain is incorporated while calculating the influence coefficient by the reflection of the discretized elements. The pentamaran hull is discretized by 450 (30×5+4×15×5) panels and the free surface by 1050 (70×15) panels. The wake surface behind the hulls is discretized by 5×5 panels. The panel arrangement for the pentamaran model is given in Fig. 1. To better resolve complex flow features around the multihull the grid is stretched in all directions with a concentration of grid points near the hull and in the stern region where the flow changes rapidly.

Dawson [11] points out that a two-point finite difference operator used in the free surface condition results in waves that are strongly damped downstream from a disturbance and three-point operator is better than two-point operator. In the present numerical scheme two-point upstream finite difference operator is used in a portion of the free surface having concentrated grid and three-point is used in the rest part of the free surface in order to satisfy the radiation condition.

The computed first and second order wave-making resistance coefficients C_w of pentamaran hull of different configurations are compared in Figs. 2 to 5 respectively. At low speeds the waves made by the ship very small and the resistance is almost frictional. With further increase in speed, the value of C_w begins increase more and rapidly up to a certain Froude number. In case of pentamaran (case 1 & 2 configurations) the humps and hollows of C_w curves in Figs. 2 & 3 appears to be the same locations but some discrepancies are found for the pentamaran of case 5 configurations. From these it can also be observed that the wave resistance coefficients of pentamaran are very sensitive to the longitudinal position of the outriggers.

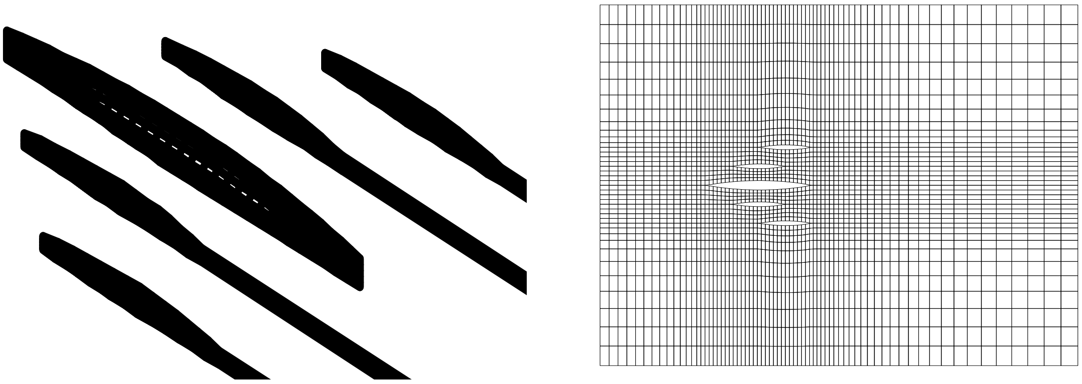

(a) Body and wake surface

(b) Free surface

Fig 1. Panel arrangement of the pentamaran model (Case 4)

Figs. 6 and 7 show the first and second order wave profile on the main hull of the pentamaran of various configurations at different Froude numbers.

The wave pattern generated by a pentamaran that is moving at a constant speed in deep water is depicted in Fig. 8. Generally, there is a symmetrical set of diverging waves that moves obliquely out from the vessel’s sailing line and a set of transverse waves that propagate along the sailing line. The transverse and diverging waves meet along the cusp locus lines that form an angle of $19^0 28'$ with the sailing line. The largest wave height is found where the transverse and diverging waves meet. If the speed of the vessel is increased, this wave crest pattern retains the same geometric form, but expands in size as the individual wave lengths increase.

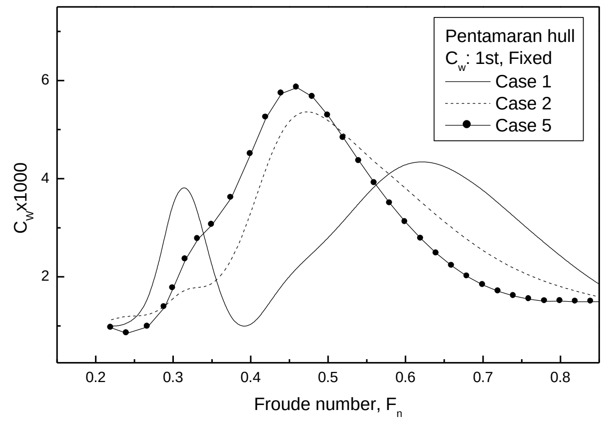

Fig. 2 Stagger effect on the first order wave making resistance on the pentamaran hull

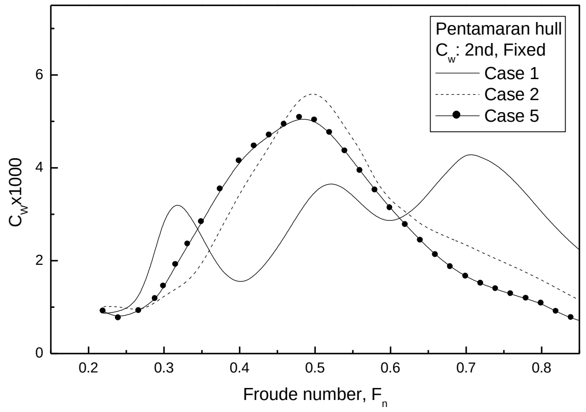

Fig. 3 Stagger effect on the second order wave making resistance on the pentamaran hull

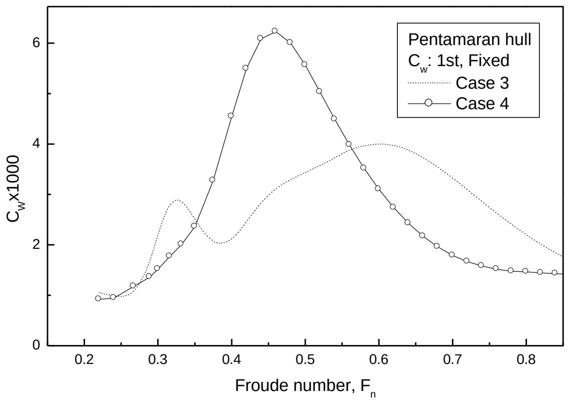

Fig. 4 Stagger effect on the first order wave making resistance on the pentamaran hull

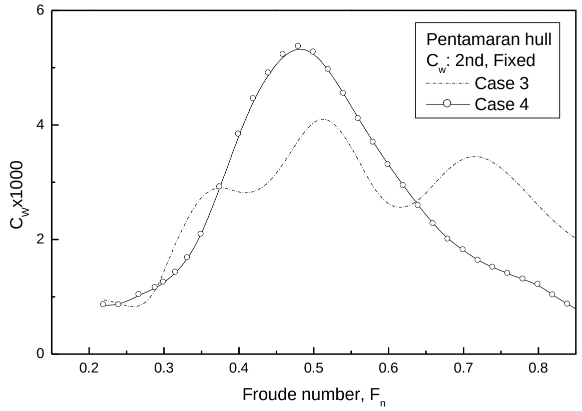

Fig. 5 Stagger effect on the second order wave making resistance on the pentamaran hull

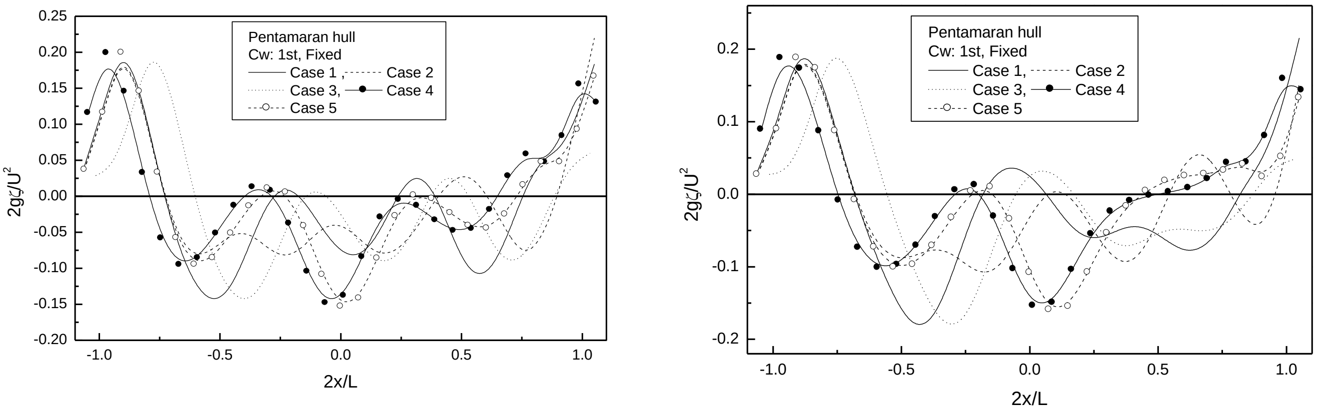

(a) Wave Elevation at $F_n = 0.240$

(b) Wave Elevation at Fn = 0.267

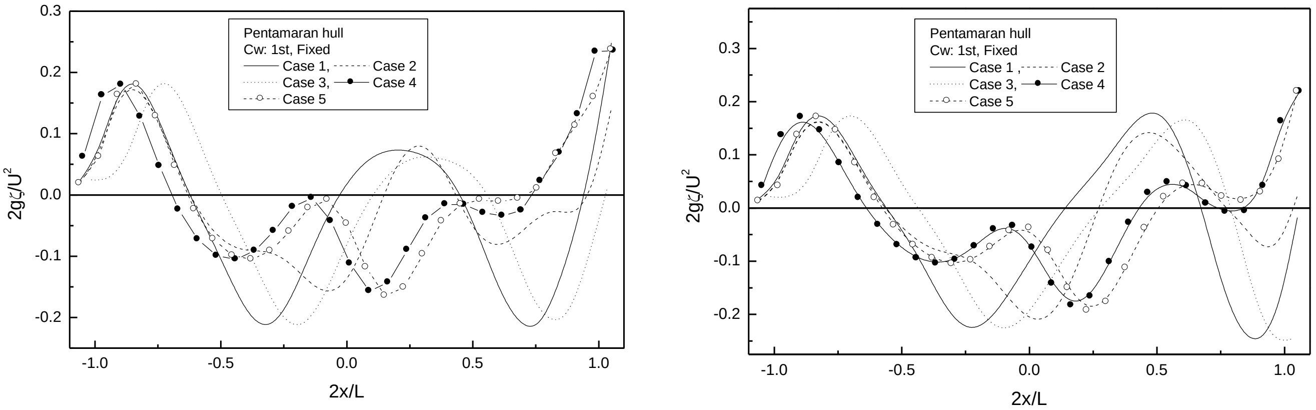

(c) Wave Elevation at $F_n = 0.300$

(d) Wave Elevation at $F_n = 0.332$

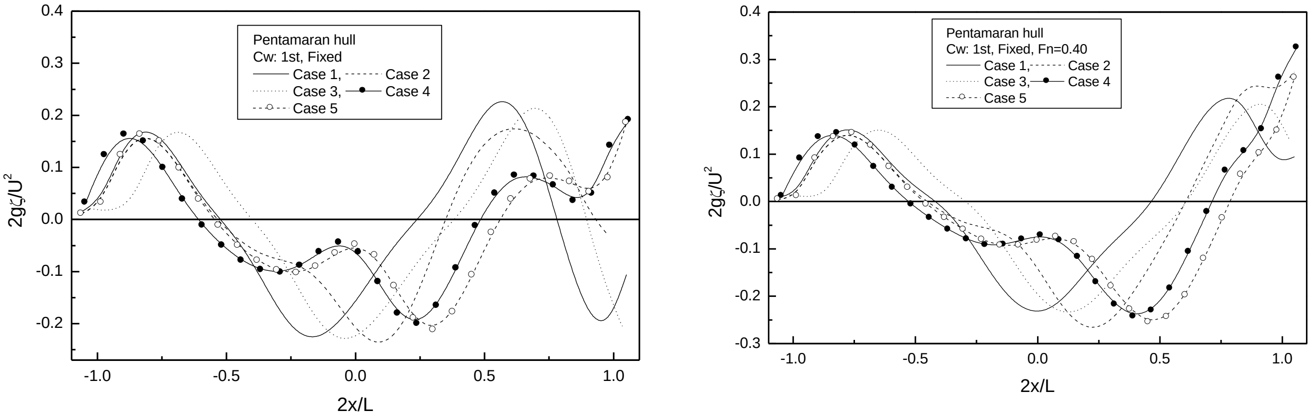

(e) Wave Elevation at $F_n = 0.350$

(f) Wave Elevation at $F_n = 0.400$

Fig. 6 Wave pattern (1st order, Fixed) at various Froude numbers for the pentamaran of different configurations

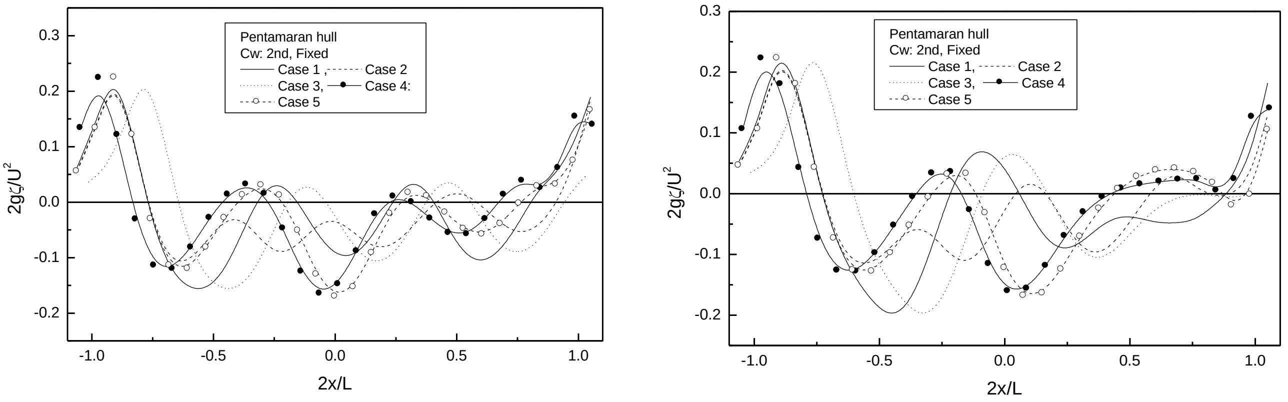

a) Wave Elevation at $F_n = 0.240$

(b) Wave Elevation at $F_n = 0.267$

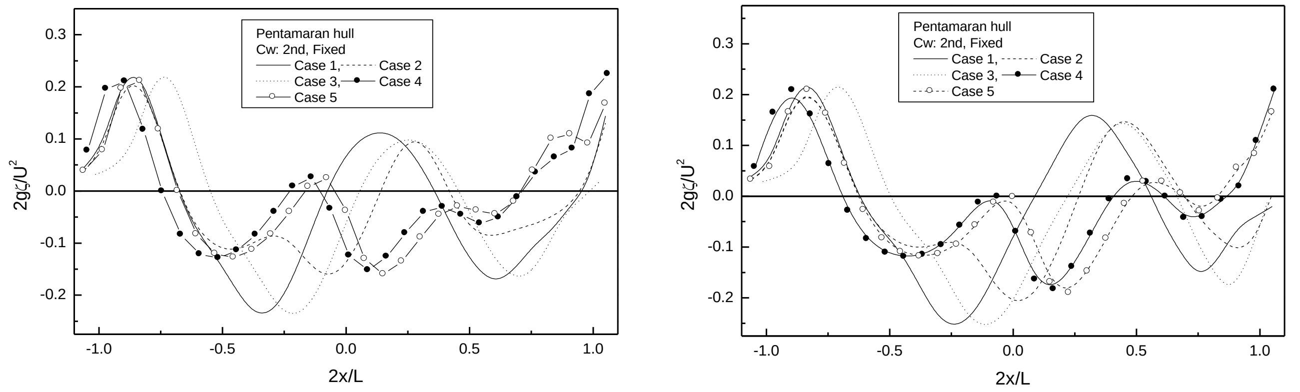

(c) Wave Elevation at $F_n = 0.300$

(d) Wave Elevation at $F_n = 0.332$

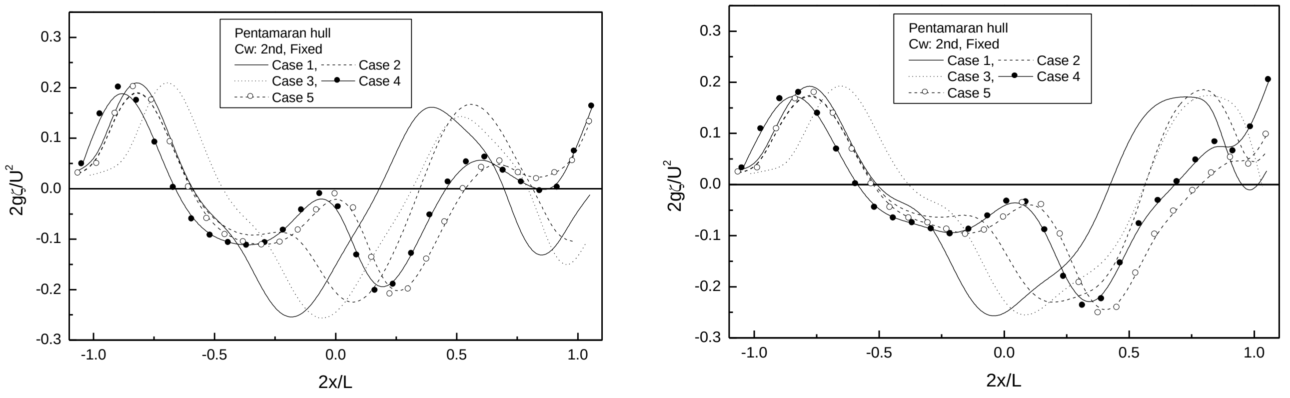

(e) Wave Elevation at $F_n = 0.350$

(f) Wave Elevation at $F_n = 0.400$

Fig. 7 Wave pattern (2^{nd} order, Fixed) at various Froude numbers for the pentamaran of different configurations

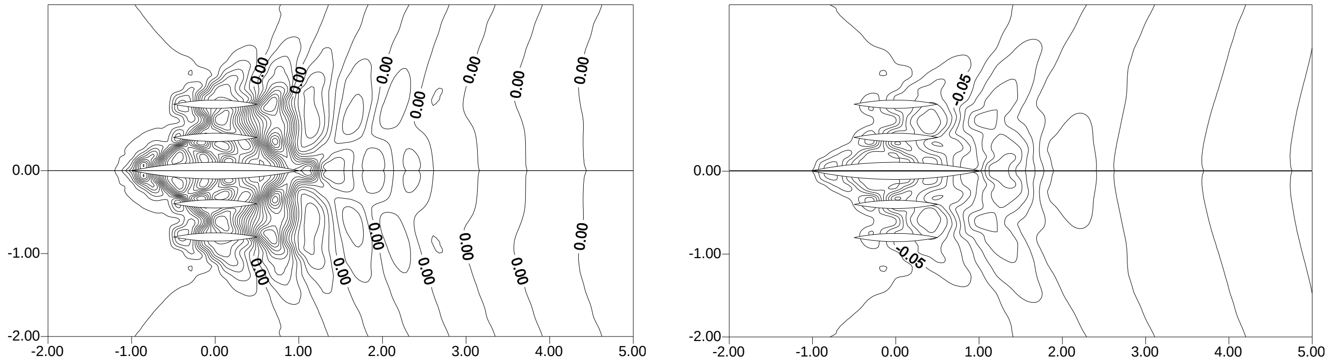

(a) Wave pattern $F_n = 0.3$

(b) Wave pattern $F_n = 0.4$

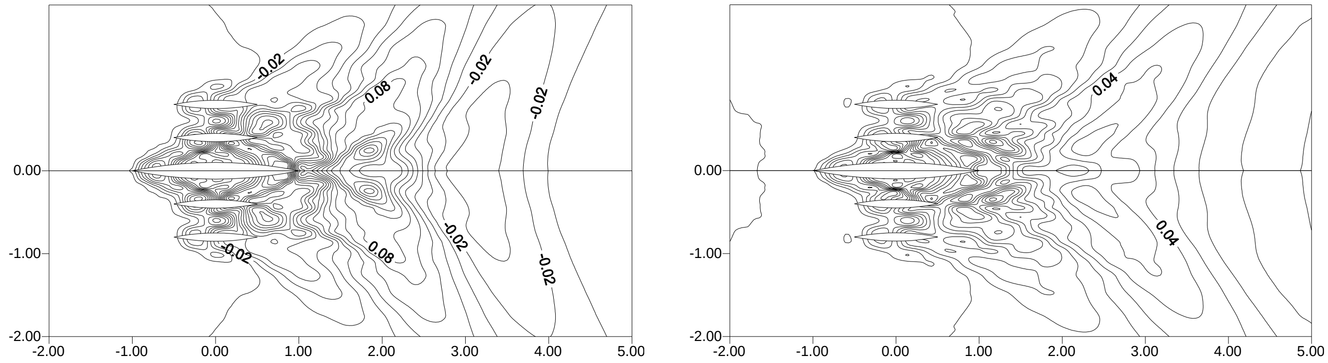

(c) Wave pattern $F_n = 0.5$

(d) Wave pattern $F_n = 0.6$

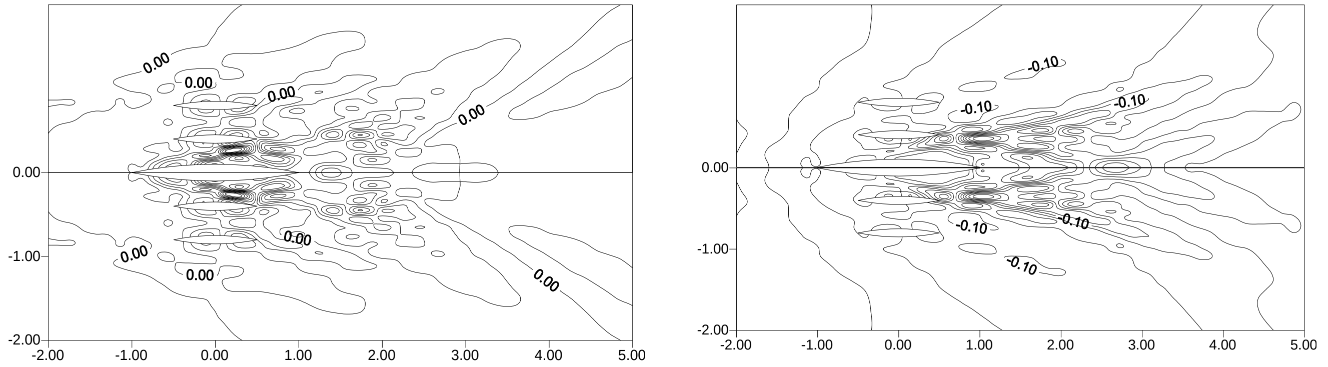

(e) Wave pattern $F_n = 0.8$

(f) Wave pattern $F_n = 1.0$

Fig 8 Wave pattern (2^{nd}, Fixed) of the pentamaran hull at various Froude number for case 5

5. Conclusions

This paper successfully presents a potential based boundary element method in connection with Kelvin classical linearized free surface condition for predicting the hydrodynamic characteristics of pentamaran hull moving in unbounded water with a constant speed. The following conclusions can be drawn from the present numerical analysis:

(i) The present method could be a useful tool for the hydrodynamic analysis of the potential flow around the multihull at an infinite depth of water and may also achieve a high precision by taking smaller panels on some regions of the free surface where the flow changes rapidly.

(ii) At higher speeds having Froude number greater than 0.8 the interference among the monohulls of the pentamaran are very small and the wave-making resistance can be reduced significantly.

(iii) Each computational method is dependent on the grid and on various other parameters. So, the present technique must be validated before it may be applied to the complicated flow around such hull shapes.

6. References

[1] Michell, J. H., 1898. The wave resistance of a ship, Philosophical Magazine, Series 5, Vol. 45, No. 272, London, pp 105-123.
[2] Kelvin, L., 1905. Deep sea ship waves, Proceedings of Royal Society Edinburgh, No. 5, pp. 1060-1084.
[3] Havelock, T. H., 1908. The propagation of groups of waves in dispersive media with application to waves on water produced by a traveling disturbance, *Proceedings of the Royal Society*, London, Vol. 81.
[4] Peng, H., 2001. Numerical Computation of Multi-hull Ship Resistance and Motion, Ph. D. Thesis, Dalhousie University, Halifax, Nova Scotia.
[5] Moraes, H. B., Vasconcellos, J. M. & Latorre, R. G., 2004. Wave resistance for high-speed catamarans, Ocean Engineering, Vol. 31, pp. 2253-2282.
[6] Yeung, R. W., 2005. Interference Resistance of Multi-hulls per thin-ship theory, 20th International Workshop on Water Waves and Floating Bodies, Longyearbyen, Spitsbergen.
[7] Begovic, E., Bertorello, C., Caldarella, S & Cassella, P., 2005. Pentamaran hull for medium size fast ferries, Hydrodynamics VI-Theory and Applications, Chang and Yeow (editors), pp. 23-27.
[8] Tarafder, M. S. and Suzuki, K., 2008. Wave-making resistance of catamaran hull in shallow water using a potential based panel method, The Journal of Ship Research, Vol.52, No. 1, pp.16-29.
[9] Wang, H. and Zao-jian, Z., 2008. Numerical research on wave-making resistance of trimaran, Journal of Shanghai Jiaotong University (Science), Vol. 13(3), pp. 348-351.
[10] Aubault, A. and Yeung, R. W., 2009. Multi-hull interference wave resistance in finite-depth waters, 24th International Workshop on Water Waves and Floating Bodies, Zelenogorsk, Russia, pp. 1-4.
[11] Dawson, C. W., 1977. A practical computer method for solving ship-wave problems, Proceedings of Second International Conference on Numerical Ship Hydrodynamics, pp.30-38.

Available online at www.sciencedirect.com

SciVerse ScienceDirect

Procedia Engineering 00 (2012) 000–000

Procedia Engineering

www.elsevier.com/locate/procedia

5th BSME International Conference on Thermal Engineering

A cylindrical methodology for the study of fabric aerodynamics

Hazim Moria[a,b]*, Harun Chowdhury[a], Fayez Aldawi[a] and Firoz Alam[a]

[a]School of Aerospace, Mechanical and Manufacturing Engineering, RMIT University, Melbourne, VIC 3083, Australia
[b]Department of Mechanical Engineering, Yanbu Industrial College, Kingdom of Saudi Arabia

Abstract

The understanding of aerodynamic behavior of sports garments in high speed sports can lead to achieve higher efficiency and performance.in order to understand the aerodynamic behavior of fabrics used in speed sports garments, prior studies have mainly used the vertical cylindrical methodology in wind tunnel environments. However, using the vertical cylindrical methodology, the aerodynamic behavior of sports garments cannot be fully realistic as athlete's all body parts are not positioned vertically all the time. Limited information is available on cylindrical methodology that can provide aerodynamic characteristics of fabrics under inclined positions. Therefore, the primary objective of this study is to develop a cylindrical methodology that can be used for both vertical and inclined positions. The suitability of the developed method for the fabrics is investigated using a wind tunnel. The results indicated that the developed methodology suited well and provided detail aerodynamic information about the fabric used.

Keywords: Aerodynamics, drag, lift, sports; fabric, angle of attack, wind tunnel.

1. Introduction

Aerodynamic behavior of sport fabrics can play a significant role in a wide range of speed sports including cycling, downhill-skiing, speed-skating, ski-jumping, sprinting and swimming. The winning time margins are progressively being reduced with the integration of advanced technologies as well as vigorous training regimes. The winning margin can be further decreased by understanding such aerodynamic behavior especially the drag and lift properties of athlete's physical body positions and their outfits (garments) [1-4]. Elaborate understanding of the aerodynamic behavior of physiological parameters (such as athlete body position and geometric shape of body parts) as well as fabric parameters (surface roughness, course/wale orientation in knitted fabric, and weft/warp orientation in woven fabric, seam configuration and placement) in high speed sports can lead to higher efficiency and achievement.

The human body shape is complex and can be considered as a bluff body. Researchers such as Hanavan [5], Hatze [6] and Yeadon [7] studied the human body anthropometric behavior and subdivided the human body into multiple cylindrical, conical and other shapes in order to represent the body with simplified anthropometric dimensions. Although this human body representation is well studied for biomechanics applications, several other researchers such as Hoerner [8], Pugh [9] and Brownlie [10] studied the aerodynamic characteristics of human bodies based on simplified human body. Kyle et al. [11, 12], Oggiano et al. [13], Strangwood [14] and Moria et al. [15] have mainly focused on the aerodynamic behavior of fabrics using vertical cylindrical methodology in wind tunnel environments. Chowdhury et al. [16] evaluated aerodynamic properties (drag and lift simultaneously) of the simplified human body parts under a range of angles of attack (α) to simulate athlete's body positions. Hence, the experimental setup used by Chowdhury and others can only measure the drag and lift of

---

* Corresponding author. Tel.: +61 3 99256103; fax: +61 3 99256108.
E-mail address: hazim.moria@rmit.edu.au

cylindrical within a limited range of angles of attack (30° to 90°). However, in many sports the body parts' position can lie below the 30° angle of attack and beyond the 90° angle of attack. Therefore, it is necessary to develop an experimental arrangement that can evaluate aerodynamic behavior of the cylinder. In this study, a new cylindrical arrangement has been designed and developed to measure the aerodynamic parameters (lift and drag) from $\alpha = 0°$ to 90°.

2. Methodology

With a view to investigate aerodynamic behavior of fabrics experimentally under a range of angles of attack (0° to 90°), a 90 mm diameter (d) and 220 mm length (l) cylinder was developed. The cylindrical arrangement consists of cylinder, rotating mechanism, strut with airfoil canopy. The cylinder was made of PVC material and used filler to make it structurally rigid. The test cylinder was connected to the hinge that was supported by the strut. The hinge was designed in such a way that the angle of attack of the test cylinder can be varied. The airfoil canopy was also covered the strut during the test to minimize the aerodynamic interference. The strut was vertically mounted on a six components load sensor (type JR-3) which has a sensitivity of 0.05% over a range of 0 to 200 N. The Model of inclined cylinder experimental arrangement is shown in Fig. 1(a). The aerodynamic forces and their moments were measured for a range of Reynolds numbers based on cylinder diameter and wind speeds (30 to 140 km/h). As shown in Fig. 1(b), each test was conducted as a function of angles of attack from stream-wise ($\alpha = 0°$) to span-wise ($\alpha = 90°$). The tunnel was calibrated prior conducting the experiments and air speeds inside the wind tunnel were measured with a modified National Physical Laboratory (NPL) ellipsoidal head Pitot-static tube (located at the entry of the test section) which was connected through flexible tubing with the Baratron® pressure sensor (manufactured by MKS Instruments, USA). The sensor was used to measure all three forces (drag, lift and side forces) and three moments (yaw, pitch and roll) at a time. Each set of data was recorded three times for 30 seconds time average with a frequency of 20 Hz ensuring electrical interference is minimized. Multiple data sets were collected at each speed tested and the results were averaged for minimizing the further possible errors in the raw experimental data.

In order to validate the results, initially the cylinder without fabric was tested. Then a knitted fabric used in sports garment fitted around the test cylinder without tension (e.g., normal fit) was investigated. The fabric sample was joined together by a seam which was placed at the rear of the cylinder to minimize the effect of seam [15].

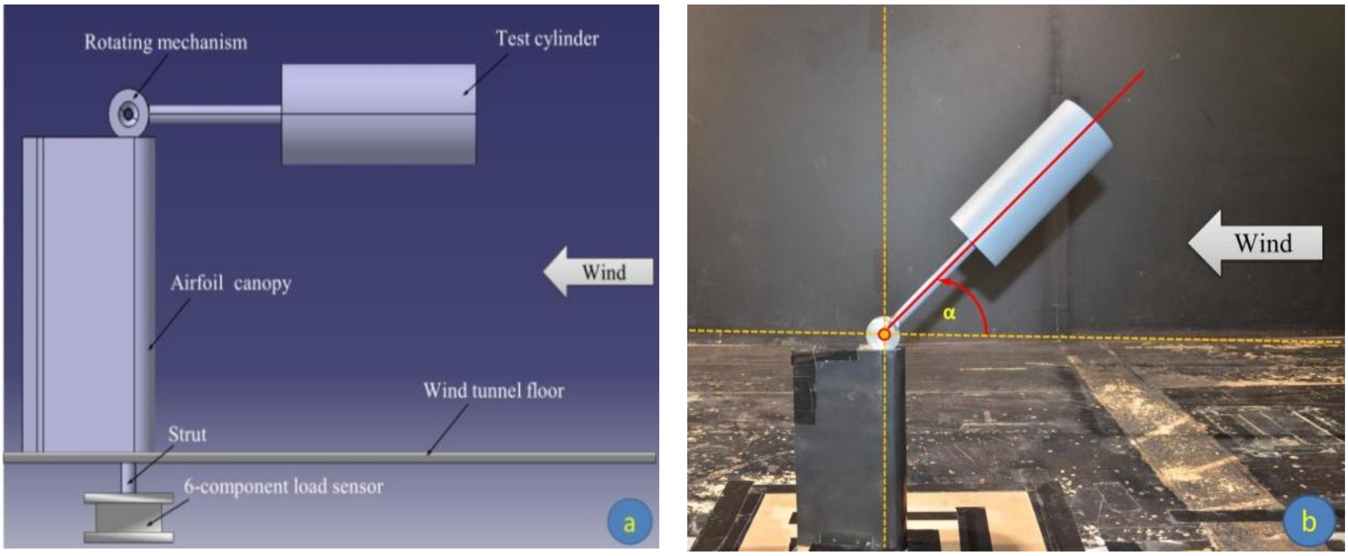

Fig. 1. Design and experimental arrangement of the cylinder geometry to measure the aerodynamic properties (lift and drag) at different angles of attack from 0° to 90° relative to wind direction. (a) Schematic CAD model; (b) cylinder in wind tunnel.

The knitted fabric sample was composed of 80 % Polyester and 20 % Spandex. The thickness of the fabric is 0.55 mm. Fig. 2 shows the fabric microstructure which was captured using a scanning electron microscope (SEM) at different magnifications. It can be seen that surface topology consists of approximately 21.10 and 167.00 μm fiber diameter and yarn size respectively. The stitch pattern was observed as V-shape. Also, the number of courses and wales per cm was found 22 and 25 respectively.

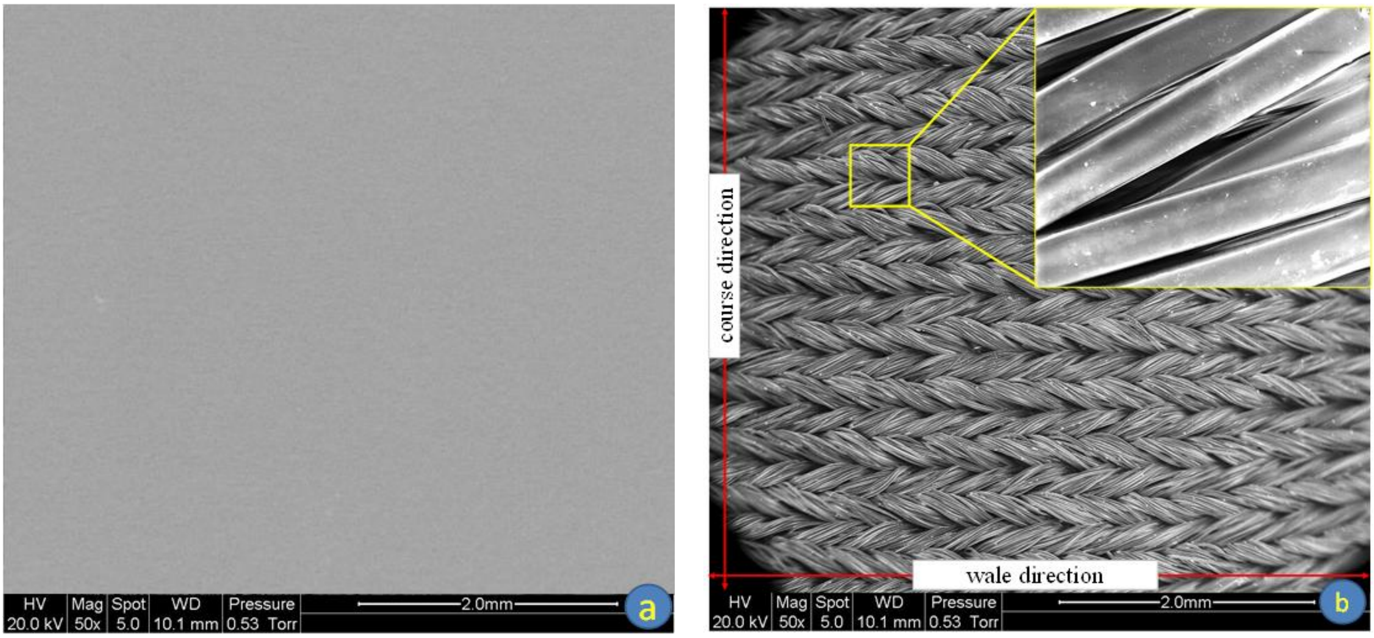

Fig. 2. Scanning electron microscope (SEM) images at 50 and 2000X magnification: (a) smooth cylinder surface; (b) fabric surface.

3. Results and discussion

All three aerodynamic forces (drag, lift and side force) and three moments (yaw, pitch and roll) were measured simultaneously. The aerodynamic force converted to their non-dimensional coefficients of C_D, C_L and C_S as a function of Reynolds number (*Re*). However, only coefficients C_D and C_L are included in this paper. The C_D, C_L and Re were calculated using equations 1, 2 and 3:

$$C_D = F_D / 0.5 \rho V^2 A \tag{1}$$
$$C_L = F_L / 0.5 \rho V^2 A \tag{2}$$
$$Re = \rho V d / \mu \tag{3}$$

where, ρ, V, A, d, and μ are the air density, wind speed, projected frontal area of the cylinder, diameter of the cylinder and absolute air viscosity respectively.

The drag coefficient (C_D) and lift coefficient (C_L) variation with Reynolds number (*Re*) (varied by wind speed ranging from 30 km/h to 140 km/h with an increment of 10 km/h) at different angles of attack (α) (0° to 90° with an increment of 15°) are shown in Fig. 3. The variations of C_D and C_L with *Re* for the smooth cylinder are shown in Fig. 3(a). The C_D and C_L for the fabric under the same *Re* are illustrated in Fig. 3(b). For the smooth cylinder, the maximum value of C_D was obtained at $\alpha = 0°$ whereas the lowest C_D value was found at $\alpha = 30°$. The magnitude of C_D values reduces with the decrease of angle of attack. The C_D variation with *Re* as a function of α indicates that with the increase of α, the C_D value increases. It may be noted that in the calculation of C_D value for the various α, the projected frontal area was considered as: $A = (l \times d \times \sin \alpha) + (\pi r^2 \times \cos \alpha)$. However, for zero angle of attack, the projected frontal area was considered as cross sectional area of the cylinder (i.e., πr^2). Therefore, despite having lowest drag experienced by the cylinder at $\alpha = 0°$, the C_D value is highest. There is no apparent flow transition occurred for the smooth cylinder under the range of *Re* tested. Generally, flow transition (from the laminar to turbulent regimes) for the smooth cylinder occurs at $Re \geq 3\times10^5$. In this study, the maximum $Re = 2.3\times10^5$ which covers with for most speed sports and also the maximum speed limit for RMIT industrial wind tunnel. It is interesting to note that an early flow transition has been noted for the smooth cylinder at angle of attack between 60° to 75°. However, it is not clear what triggered this flow transition. It is believed that the oblique flow generated by the inclined cylinder might cause this early transition. Further studies are required to understand this behavior. The similar behavior of the smooth cylinder for the C_L was noted as shown in Fig. 3 (a). The C_L behavior at low *Re* is believed to be experimental error. The C_D value at stream-wise ($\alpha = 0°$) and span-wise ($\alpha = 90°$) was agreed with published data (Hoerner [8], Chowdhury et al. [16], Achenbach [17] and White [18]). However, the maximum C_L value was found at $\alpha = 45°$ and values decrease with the further increase or decrease of angles of attack. Furthermore, the C_L values at $\alpha = 15°$ and 30°, the direction is negative at low *Re*, however, the C_L values increases with the increase of up to 70 km/h ($Re = 1.18\times10^5$).

On the other hand, Fig. 3(b) shows the C_D and C_L as a function of *Re* with fabric at different angles of attack from 0° to 90°. The data clearly indicate that there is a significant effect in the aerodynamic behavior on the cylinder at different angles of attack. However, the transitional effects occur at 70 km/h for α = 30°, 45°, 60°, 75° and 90°. Nevertheless, no flow transitional effect was noted at α = 0° and 15°. The minimum C_D value (0.399) is obtained at α = 75° and 90 km/h ($Re = 1.51\times10^5$).

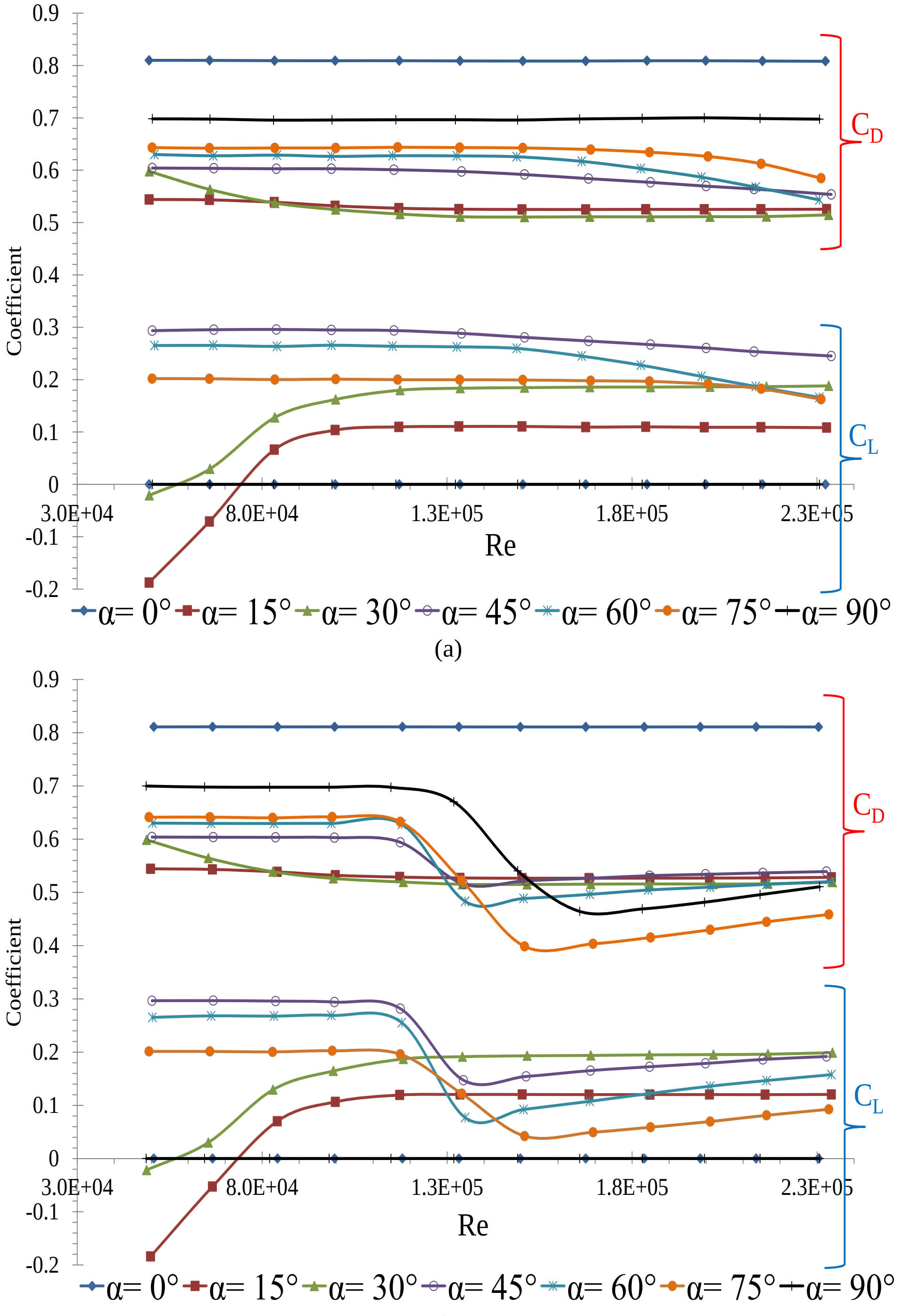

(a)

(b)

Fig. 3. Drag and lift coefficient (C_D and C_L) as a function of Reynolds number (*Re*) at different angles of attack from 0° to 90° relative to wind direction for cylinder: (a) without fabric; (b) with fabric.

As mentioned earlier, the majority of the aerodynamic drag is generated by the body shape which is predominantly pressure drag. The projected frontal area represents a significant factor in aerodynamic drag generation. In aeronautical and many speed sports applications, the lift to drag ratio is considered fundamental. Here, lift to drag ratio relationships have plotted for the smooth cylinder as well as cylinder with the fabric under the same test conditions as mentioned earlier. The graphs are shown in Figs. 4(a) and (b). The maximum value of *L/D* was obtained at α = 45° for both cases whereas the lowest C_D value was found at α = 15° and 75° for the smooth cylinder and cylinder with the fabric respectively. It also shows that the fabric surface morphology (surface structure and roughness) and the angle of attack changes the flow behavior (e.g., effect of flow regimes).

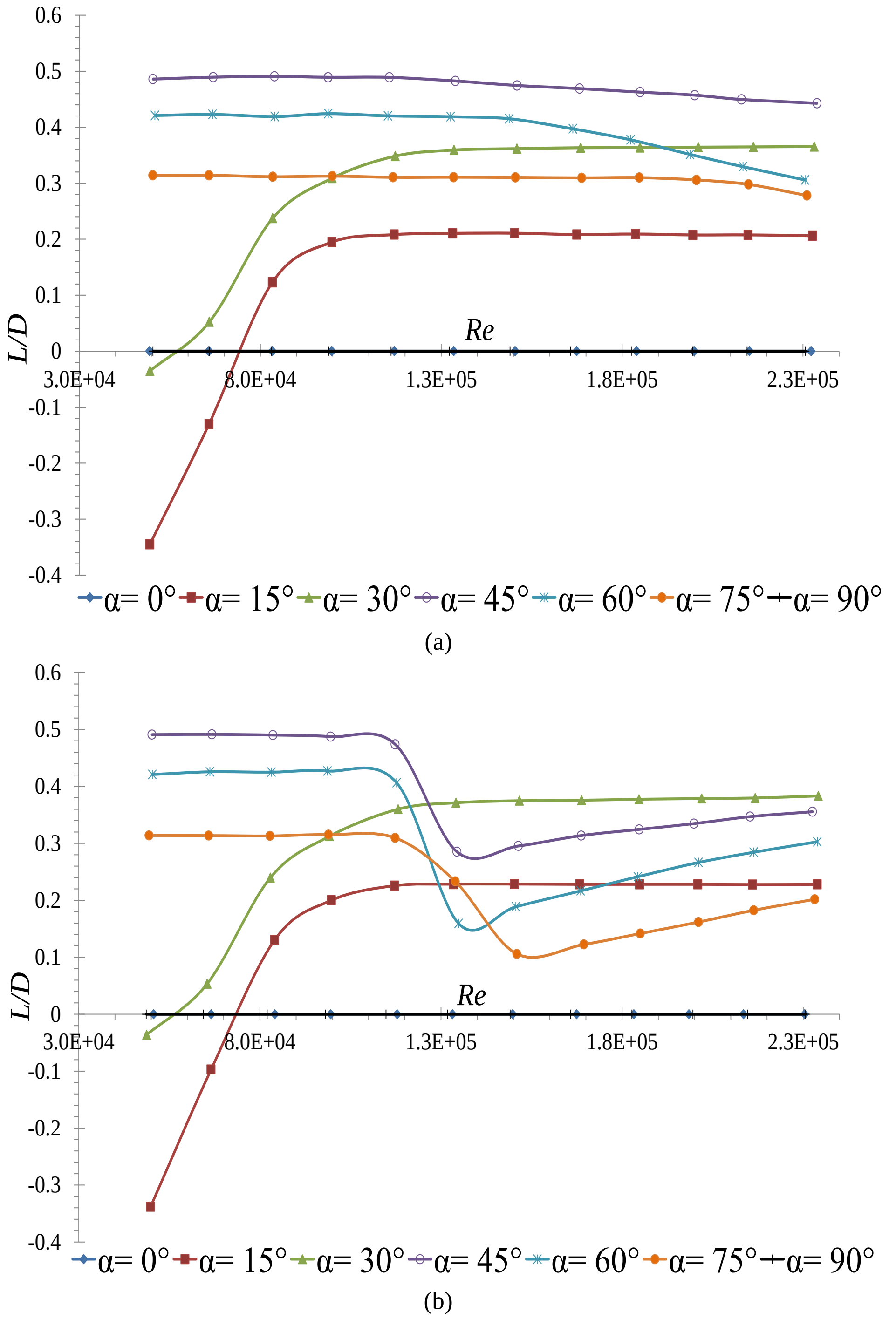

Fig. 4. The variation of *L/D* with Re at different angles of attack from 0° to 90°: (a) without fabric; (b) with fabric.

4. Conclusions

The following conclusions have been made based on the experimental study presented here:

- Using a standard cylindrical geometry, an experimental methodology has been developed to study the aerodynamic behavior of fabrics over a wide range of angles of attack (0° to 180°). The methodology is simple, easy to setup, and aerodynamically less intrusive.
- The analyzed results indicated that the highest lift-to-drag ratio (*L/D*) was generated at an angle of attack (α) of 45° for both the smooth surfaced and fabric covered cylinders.
- The minimum lift-to-drag ratio was obtained at higher angle of attack ($\alpha = 75°$) for the fabric covered cylinder, while the minimum value of *L/D* was found at lower angle of attack ($\alpha = 15°$) for a smooth surfaced cylinder.

Acknowledgements

We express our sincere gratitude and thanks to the Government of Kingdom of Saudi Arabia for providing the PhD Scholarships to the first author. We acknowledge the facilities, and the scientific and technical assistance, of the Australian Microscopy & Microanalysis Research Facility at the RMIT Microscopy & Microanalysis Facility, at RMIT University.

References

[1] Barelle, C., Ruby, A., Tavernier, M., 2004. Experimental model of the aerodynamic drag coefficient in alpine skiing, Journal of Applied Biomechanics 20(2), p. 35.
[2] Grappe, F., Candau, R., Belli, A., Rouillon, J. D., 1997. Aerodynamic drag in field cycling with special references to the Obree’s position, Ergonomics 40(12), p. 1299.
[3] Lukes, R. A., Chin, S. B., Haake, S. J., 2005. The understanding and development of cycling aerodynamics, Sports Engineering 8(2), p. 59.
[4] Laing, R. M., 2002. Clothing, textiles and human performance: a critical review of the effect on human performance of clothing and textiles. The Textile Institute, Manchester.
[5] Hanavan, E. P., 1964. A mathematical model of the human body, AMRL-TR-64-102, AD-608-463, Aerospace Medical Research Laboratories, Wright-Patterson Air Force Base, Ohio, USA.
[6] Hatze, H. A., 1980. Mathematical model for the computational determination of parameter values of anthropomorphic segments, Journal of Biomechanics 13(10), p. 833.
[7] Yeadon, M. R., 1990. The simulation of aerial movement—II. A mathematical inertia model of the human body, Journal of Biomechanics 23(1), p. 67.
[8] Hoerner, S. F., 1952. Aerodynamic Properties of Screens and Fabrics, Textile Research Journal, 1(22), p. 274.
[9] Pugh, L. G. C. E., 1974. The relation of oxygen intake and speed in competition cycling and comparative observations on the bicycle ergometer, Journal of Physiology 241(1), p. 795.
[10] Brownlie, L. W., 1992. Aerodynamic characteristics of sports apparel. (PhD Thesis). University of British Columbia, Canada.
[11] Kyle, C. R., Brownlie, L. W., Harber, E., MacDonald, R., Shorten, M., 2004. The Mike Swift Spin Cycling Project: Reducing the Aerodynamic Drag of Bicycle Racing Clothing by Using Zoned Fabrics. UK: International Sports Engineering Association, p. 118.
[12] Kyle, C. R., Caiozzo, V. J., 1986. The Effect of Athletic Clothing Aerodynamics upon Running Speed, Medicine and Science in Sports and Exercise 18, p. 509.
[13] Oggiano, L., Troynikov, O., Konopov, I., Subic, A., Alam, F., 2009. Aerodynamic behaviour of single sport jersey fabrics with different roughness and cover factors, Sports Engineering 12(1), p. 1.
[14] Strangwood, M., 2007. Modelling of Materials for Sports Equipment, in “*Materials in Sports Equipment*”. Woodhead Publishing Ltd., Cambridge.
[15] Moria, H., Chowdhury, H., Alam, F., Subic, A., 2010. Comparative aerodynamic analysis of commercial swimsuits, Journal of Sports Technology 3(4), p. 261.
[16] Chowdhury, H., Alam, F., Mainwaring, D., Subic, A., Tate, M., Forster, D., Beneyto-Ferre, J., 2009. Design and methodology for evaluating aerodynamic characteristics of sports textiles, Sports Technology 2(3-4), p. 81.
[17] Achenbach, E., 1974. The effects of surface roughness and tunnel blockage on the flow past spheres, Journal of Fluid Mechanics 65, p. 113.
[18] White, F. M., 2003. Fluid Mechanics (5th ed.). McGrow-Hill, New York.

Available online at www.sciencedirect.com

SciVerse ScienceDirect

Procedia Engineering 00 (2012) 000–000

Procedia Engineering

www.elsevier.com/locate/procedia

5th BSME International Conference on Thermal Engineering

Effect of Wall Surface Roughness on Shock Boundary Layer Interaction

Arun Kumar R[a] , Heuy Dong Kim[a*] and Toshiaki Setoguchi[b]

[a] *School of Mechanical Engineering, Andong National University, Andong, 760-749,South Korea*

[b]*Department of Mechanical Engineering, Saga University, Saga, Japan*

Abstract

Shock wave boundary layer interaction appears ubiquitous in high-speed flows and exhibits many salient features on the local as well as the whole flow field. Much has been learned on the major characteristics of the shock wave boundary layer interaction like boundary layer separation, reattachment, shock unsteadiness, the interaction length, etc. The local flow state where shock wave interacts with wall boundary layer affects the entire interaction flow field. Recently, several investigations have been performed to change the local flow state, thereby controlling the shock wave boundary layer interaction. It is, however, difficult to generalize the interaction flow characteristics as the data obtained to date. In the present study, the effects of wall surface roughness on the shock wave boundary layer interaction have been investigated with the help of computational fluid dynamics methods. A turbulent transonic circular arc bump was chosen for the present work. The surface roughness was varied by means of changing the roughness height parameter in the wall functions used to model the wall effects. The performance of different turbulence model on predicting the roughness effects on shock flow field were compared. The results show that the shock front moves upstream to the bump surface as wall roughness increases.

Keywords: Flow Separation, Shock Boundary Layer Interaction, Surface Roughness, Transonic Bump

Nomenclature

C_p	pressure coefficient, $2(p-p_{in})/\rho_{in} U^2_{in}$
k_s	equivalent sand grain roughness height
k_s^+	non- dimensional roughness height
S_R	roughness parameter
u^+	non-dimensional velocity in x- direction
u^+	non-dimensional velocity in x- direction
u_τ	shear velocity
y^+	non-dimensional distance from the wall

Greek symbols

ω	specific dissipation rate of k
ε	time rate of dissipation of k
ρ_{in}	inlet density
τ_w	wall shear stress

---

[*] H.D Kim. Tel.: +010-6846-2278; fax: +054-820-6127.
E-mail address: kimhd@andong.ac.kr

1. Introduction

Many high speed engineering devices such as turbines, compressors, flow over missiles, airfoils and turbine blades etc. are often encountered with the generation of shock waves. The formation of shock front produces a steep adverse pressure gradient which when interacts with the boundary layer causes flow separation. In general, the flow field characteristics under such circumstances are termed as shock boundary layer interactions (STBL). The shock boundary layer interaction alters the flow characteristics and produce additional effects such as flow separation, re- attachment, shock unsteadiness etc. This phenomenon’s affect the global flow features and cause much degradation in the performance of many aerodynamic devices. Hence the shock boundary layer interaction research got much attention in the past and a greater technical advancement in this field has been achieved.

The initial researches to comprehend the shock boundary layer interaction flow characteristics started in late 1940’s [1-2]. The early studies given insight into many important flow features involved in shock boundary layer interaction flows such as flow separation, flow reattachment, shock unsteadiness etc. The upstream influence such as the Mach no. and Reynolds number on the shock boundary layer interaction characteristics have been widely studied by Settles [3]. They chosen a compression ramp model and observed that the interaction is more severe when the ramp angle increases. Recently, Bookey [4] studied the effect of comparatively low Reynolds number flow on the STBL interaction flows. He observed that with decrease in Reynolds number the separation point from the ramp initiation increases.

Another common physical problem in which shock interaction happens with the boundary layer is the flow through aerofoils. Aerofoil flows are often encountered with a transonic flow. As the flow approaches the bumps, the subsonic flow turns to supersonic and produces shock wave. An experimental study on the shock boundary layer interaction in an aerofoil was carried out by Liu. He assumed the aerofoil to be a circular bump and was attached to the top wall of the test section. Their experiment given greater insight regarding the flow separation characteristics. As the shock strength increases the flow separation and reattachment effects also increases. Several researches were also carried out to reduce the flow separation effect on transonic bump flows. One significant work among them was the study conducted by Regunathan [5], in which he proposed the introduction of several holes for the passive shock/boundary layer control.

Recently, with the development of computational methods, a much insight in shock/boundary layer interaction flow physics have been drawn using numerical visualization techniques which would have been difficult with conventional experimental techniques. The accuracy of different turbulence model in predicting the shock boundary layer interaction flow field was investigated by Kim [6].The unsteady shock oscillation characteristics over a super critical airfoil with transonic flow was investigated by Deck[7] using Large Eddy Simulation. A Large Eddy Simulation of the shock turbulent boundary layer interaction over a two dimensional bump with transonic turbulent flow was also carried out by Wollblad [8]. Later Koing [9] performed computational and experimental studies for the drag reduction studies in a transonic airfoil using an array of three dimensional circular bumps.

From these past studies much advancement has been achieved for the shock boundary layer problems subjected to smooth wall. But for a rough wall the shock boundary layer interaction problems becomes more complex. Babinsky [10] studied the effect of supersonic flow over a rough flat plate and investigated the flow features. They observed that the wall surface have a prolonged influence to the far downstream flow also.Inger [11] did an experimental analysis on a transonic circular bump with different roughness values to study the effect of roughness parameter on shock boundary layer interaction flow field. They observed that an increase in wall surface roughness enhances the onset of separation point.

Even though much advancement has been made in shock turbulent boundary layer interaction problems, the effect of surface roughness on such flow fields have been very less investigated. In this paper a 2-D CFD method was used to study the effect of surface roughness on the shock boundary layer interaction flow field. The CFD simulations were carried out with the same boundary conditions as that used by the experimental studies conducted by Inger. The present study mainly focuses to have a detail understanding of the flow field of shock bounder layer interaction under the influence of a rough wall. The accuracy of different turbulent model in predicting the flow physics were compared. The effect of surface roughness on separation point, interaction length etc. was studied in detail.

2. Computational Domain and Numerical Methods

For the present study a 2-D circular bump geometry of radius 580 mm was considered. The width of the channel is 190 mm. The circular bump is located at a distance of 677 mm from the inlet. The computational model and boundary conditions used for the present simulation is same as that of the experimental study conducted by Inger. The computational domain details are shown as in Fig.1.

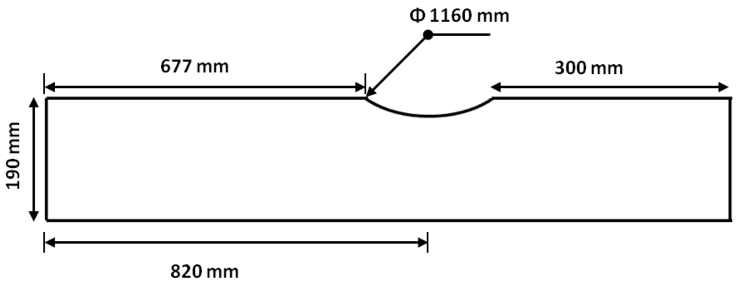

Fig. 1. Computational domain

The inlet stagnation conditions used for the simulation were 140 kPa and 310 K. The Mach number at the inlet was 0.73 and the Reynolds number (Re) per unit length was 1.7 x 10^6/m. The free stream boundary layer thickness (δ_0) is 13.5 mm. In the experiment, the back pressure was controlled by using a throat. The position of this throat and the back pressure values were not specified in the reference paper [11]. So for the simulation the exit pressure was gradually reduced to match the numerically simulated shock location with the experimental value. The derived back pressure value was 98 kPa.

The computational model was discretized into structured quadrilateral cells with clustering of cells near to the wall. Unsteady Reynolds Averaged Navier-Stokes equations were used to mathematically simulate the flow physics. The working gas was assumed to behave the ideal gas laws and the viscosity will vary with respect to temperature according to the Sutherland law. The flux component of the governing equation was discretized using Reo-FDS scheme. The special discretization was carried out using second order schemes. The governing flow equations were solved in a coupled manner using commercial solver, Fluent.

The surface roughness effect on shock boundary layer interaction greatly depends on the boundary layer turbulence simulation. Generally the RANS based k-ε turbulence model uses the wall functions to simulate the roughness near the wall. The wall laws for the mean velocity modified to incorporate the roughness value are as shown in Eq. (1).

$$u^+ = \frac{1}{k}\ln\left(y^+\right) + 5.5 - \Delta B \tag{1}$$

where ΔB is the downward shift of the velocity profile and depends on the size and type of the roughness. For uniform sand grain surface ΔB is predicted using Eq. (2)

$$\Delta B = \frac{1}{k}\ln\left(1 + 0.3 k_s^{\,+}\right) \tag{2}$$

For RANS based k- ω model the roughness effect is modelled by applying the boundary condition for ω which incorporates the wall roughness parameter. The equation for determining ω is shown in Eq. (3).

$$\omega\big|_{y=0} = \left(u_\tau^{\,2}/v\right) S_R \tag{3}$$

where S_R is the roughness parameter defined as

$$S_R = \begin{cases} \left(50/k_s^{\,+}\right)^2 & k_s^{\,+} < 25 \\ 100/k_s^{\,+} & k_s^{\,+} \geq 25 \end{cases} \tag{4}$$

3. Results and Discussion

The shock boundary layer interaction flow field is explained in Fig.2, with the help of the Mach number (M) contours across the section. It can be clearly noticed that the formation of shock front causes the flow to separate. The separated flow reattaches downstream of the channel. Reverse flow can be observed in this separated region.

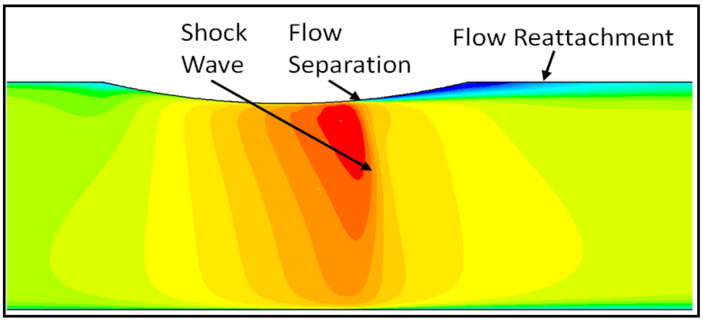

Fig. 2. Mach number distribution across the transonic bump section for smooth wall

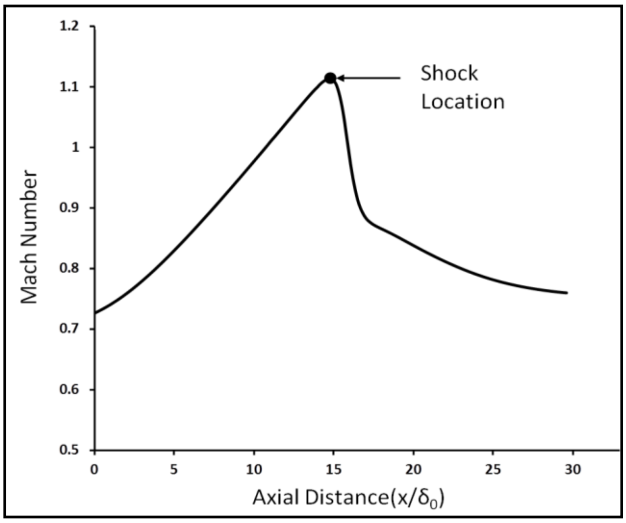

Fig. 3. Mach number distribution across the transonic bump section for smooth wall

Fig.3 shows the Mach number distribution across the center line for smooth wall case. The presence of shock wave is characterized by a sudden decrease in Mach number, which is clearly observable from Fig.3.

Initially for checking the accuracy of different turbulence model in predicting the roughness effects, three cases with different turbulence models such as realizable k-epsilon, standard k-omega and SST-k-omega respectively, were simulated. The CFD simulation conditions for the three cases are shown in Table.1.

Table 1. CFD conditions for different turbulence model simulation

Cases	Turbulence	Inlet Total Pressure (p_0)	Outlet Pressure (p)
1	Realizable k-epsilon	140 kPa	98kPa
2	Standard k-omega	140 kPa	98kPa
3	SST k-omega	140 kPa	98kPa

Fig.4 shows the pressure coefficient across the bump wall for different turbulence models. The computationally predicted results show a good agreement with the experimental values upstream to the shock location. Downstream of the shock the computationally determined value show slight deviation from the experimental values. These may be due to the non equilibrium effects associated with the shock boundary layer interaction. The realizable k-ε models show more closer results compared to the experiment. The surface roughness simulation based on the wall function, as used in k-ε, shows more accurate flow prediction compared to the ω based model.

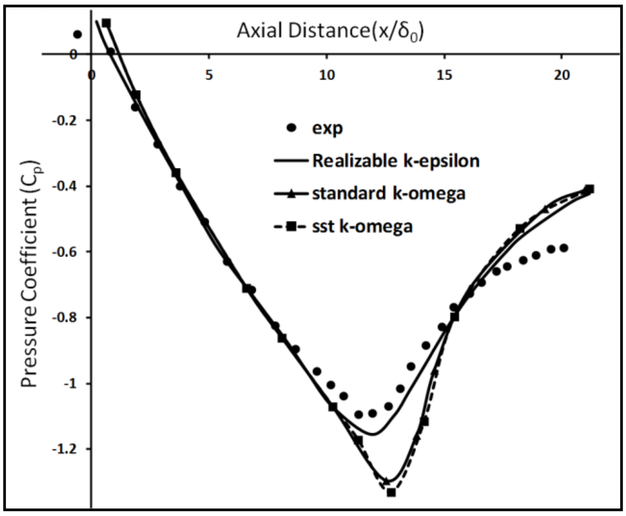

Fig. 4. Pressure coefficient distributions along the bump wall for different turbulence models

The pressure coefficient comparison along the bump wall for a smooth and rough wall is shown in Fig.5. It can be noticed that for a rough wall the shock strength will be lesser compared to the smooth wall. This is mainly due to the elevated friction losses due to the wall roughness effect. Also the separation point shifts upstream of the bump surface for the rough wall compared to a smooth wall.

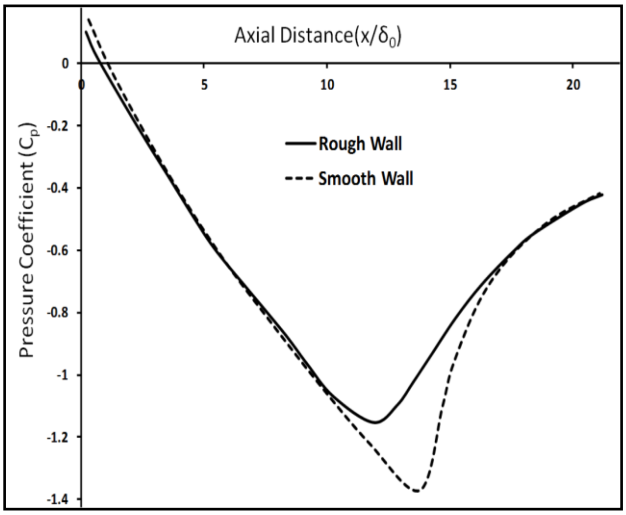

Fig. 5. Pressure coefficient distributions along the bump surface for rough wall (k_s=580μm) and smooth wall

As the surface roughness value increases the shock strength also decreases. The separation point slightly shifts upstream as surface roughness value increases. This can be clearly visualized from the pressure coefficient distribution along the bump surface with two different surface roughness heights of 580 μm and 1470 μm respectively, as shown in Fig.6.

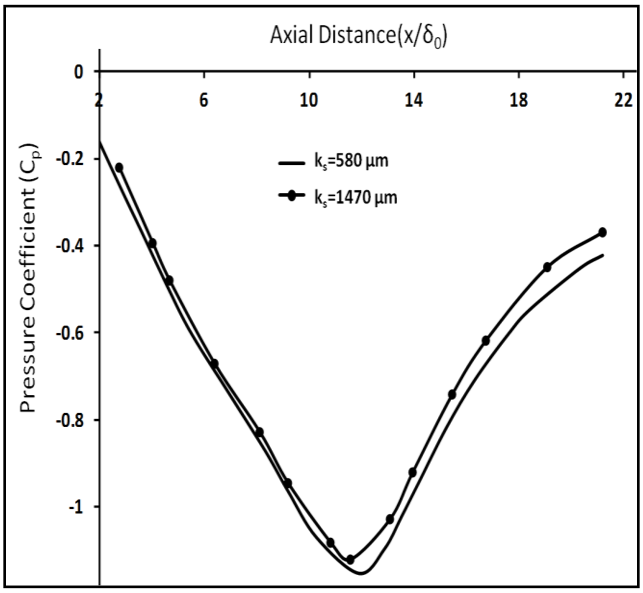

Fig. 6. Pressure coefficient distributions along the bump surface for difference roughness heights

4. Conclusions

In the present study, the wall surface roughness effect on the turbulent shock boundary layer interaction in transonic circular bump geometry was investigated using computational techniques. The accuracy of different turbulence model in predicting the surface roughness effect on shock boundary layer interaction effects was also investigated. It was found that the realizable turbulence model which uses the wall function based roughness model predicts more accurate results. Compared to a smooth wall the shock strength for a rough wall is lesser mainly due to the elevated friction losses. Also for a rough wall the flow separation starts much ahead compared to that of a smooth wall. As the wall roughness value increases, the shock strength decreases. This is obvious due to the increase in friction losses. The separation point slightly shifts upstream as surface roughness value increases.

References

[1] Bachalo, W.D., Johnson, D.A., 1979. “An Investigation of Transonic Turbulent Boundary Layer Separation generated in an Axi Symmetric Flow Model,” AIAA- 12th Fluid and Plasma Dynamics Conference.

[2] Bradshaw, P., Galea, P.V., 1967. Step Induced Separation of a Turbulent Boundary Layer in Incompressible Flow, Journal of Fluid Mechanics 27, p.111.

[3] Settles, G.S., Fitzpatrick, T.J., 1979. Detailed Study of Attached and Separated Compression Corner Flowfields in High Reynolds Number Supersonic Flow, AIAA 17, p.579.

[4] Bookey, P.,1979. An Experimental Study of Shock/Turbulent Boundary Layer Interactions at DNS Accessible Reynold’s Numbers, AIAA 17, p.579.

[5] Ragunathan, S., Mabey, D.G., 1987. Passive Shock Wave/ Boundary Layer Control on a Wall Mounted Model, AIAA 25, p.275.

[6] Kim, S.D., Kwon, C.O., Song, D.J., 2004. Comparison of Turbulence Models in Shock-Wave/ Boundary Layer Interaction, KSME International Journal 18, p.153.

[7] Deck, S., 2005. Numerical Simulation of Transonic Buffet over a Super Critical Airfoil, AIAA Journal 43, p.1556.

[8] Wollblad, C., Davidson, L., Eriksson, L.E., 2006. Large Eddy Simulation of Transonic Flow with Shock Wave/ Turbulent Boundary Layer Interaction, AIAA 44, p.2340.

[8] Wollblad, C., Davidson, L., Eriksson, L.E., 2006. Large Eddy Simulation of Transonic Flow with Shock Wave/ Turbulent Boundary Layer Interaction, AIAA 44, p.2340.

[9] Koing, B., Patzold, M., Lutz, T., Kramer, E., Rosemann, H., Richter,K., Uhlemann,H., 2009. Numerical and Experimental Validation of Three Dimensional Shock Control Bumps, Journal of Aircraft 46, p.675.

[10]Babinsky, H., Inger, G,R., McConnel, A,D., 1999. “A Basic Experimental/Theoretical Study of Rough Wall Turbulent Shock/Boundary Layer Interactions,” Proceedings of the 22nd International Symposium on Shock Waves. London, UK.

[11]Inger, G,R., Gendt, C., 1997. “An Experimental Study of Transonic Shock/ Boundary Layer Interaction on a Roughened Surface,” 35th AIAA Aerospace Science Meeting and Exhibit. Nevada, USA.

Available online at www.sciencedirect.com

SciVerse ScienceDirect

Procedia Engineering 00 (2012) 000–000

Procedia Engineering

www.elsevier.com/locate/procedia

5th BSME International Conference on Thermal Engineering

RANS Computation of Transonic Buffet Over a Supercritical Airfoil

A.B.M. Toufique Hasan[a]*, Md. Mahbub Alam[b]

[a] *Assistant Professor, Department of Mechanical Engineering, Bangladesh University of Engineering and Technology (BUET), Dhaka-1000, Bangladesh*
[b] *Engineer Officer, Biman Bangladesh Airlines Limited, Dhaka, Bangladesh*

Abstract

Transonic flow over an airfoil involves shock induced oscillation at certain free steam Mach number and angle of attack due to the interaction of shock wave with airfoil boundary layer which consequences fluctuating lift and drag coefficient, aero acoustic noise and vibration, high cycle fatigue failure (HCF), buffeting and so on. In the present study, Reynolds Averaged Navier-Stokes (RANS) equations have been used to predict the transonic buffer and corresponding aerodynamics behaviour over NASA SC(2) 0714 supercritical airfoil. RANS computations have been performed at free stream Mach number of 0.77 while the angle of attack was varied from 2° to 7°. The results obtained from the numerical computation have been validated with the experimental results. Mach contour, lift and drag coefficient, and pressure history over the airfoil surface have been analyzed and confirmed the transonic buffet phenomena.

Keywords: Transonic flow, Buffet, Supercritical Airfoil.

Nomenclature

c	chord length (mm)
c_l	lift coefficient (-)
c_d	drag coefficient (-)
f	frequency (Hz)
M_∞	free stream Mach number (-)
t	time (s)
T	time period (s)
p	static pressure (kPa)
p_{rms}	root mean square of pressure fluctuation (kPa)
Greek symbols	
α	angle of attack (°)

1. Introduction

The transonic flow over an airfoil is associated with the appearance of unsteady shock waves which interact strongly with the boundary layer. At a given free-stream Mach number and for small angle of attack, the flow reattaches; while at sufficient high angles of attack, the boundary layer separates either as a bubble at the foot of the shock or at the trailing edge [1-2]. At particular transonic flow conditions, the self-excited shock oscillates alternatively along the airfoil surfaces. This

---

* Corresponding author. Tel.: +880-173-071-4444; fax: +880-2-8613026.
E-mail address: toufiquehasan@me.buet.ac.bd

large-scale flow-induced shock motion is known as transonic shock buffet which is potentially detrimental for aerodynamic structure as well as the safe operation of turbomachinery .

Several computational and experimental studies showed that the buffet onset is influenced by the geometry and trailing edge viscous-inviscid interaction. Lee [3] proposed a feedback mechanism for self-excited shock motion on a supercritical airfoil. On the other hand, prominent features of the shock buffet of the 18-percent-thick circular-arc airfoil have been computed by Gillan [4] and Rumsey *et al.* [6] with Navier-Stokes and thin-layer Navier-Stokes codes, respectively. These computations highlighted the sensitivity of this type of problem to the turbulence and the flow modeling and the importance of shock and trailing-edge separation. However, these studies have determined the range of Mach number for the onset of shock buffet for the circular-arc airfoil quite accurately. In case of 18-percent circular-arc airfoil, trailing edge separation has observed prior to shock induced separation and shock buffet onset [6-7]. Shock oscillation is antisymmetric and hysteresis occurs at the range of onset Mach number for this airfoil [8].

Though supercritical airfoils are introduced to increase the drag divergence Mach number and thus to extend the buffet boundary, several experiments showed that these airfoils also experience the shock buffet at flight conditions [9-11]. Xiao *et al*. [11] numerically investigated the transonic buffet over a Bauer–Garabedian–Korn (BGK) No. 1 supercritical airfoil. Two steady cases ($M_\infty = 0.71$, $\alpha = 1.396°$ and $M_\infty = 0.71$, $\alpha = 9.0°$) and one unsteady case ($M_\infty = 0.71$, $\alpha = 6.97°$) were analyzed in detail. Space-time correlations of the unsteady pressure field were used to calculate the time for pressure waves to travel downstream within the separated region from the shock wave to the airfoil trailing edge and then back from the trailing edge to the shock outside the separated region. The reduced frequency so calculated agreed well with the computed buffet frequency.

In the present study, the Reynolds averaged Navier-Stokes (RANS) equations with k-ω SST (Shear Stress Transport) two equation turbulence model is applied to predict the shock induced buffet onset over a supercritical airfoil NASA SC(2) 0714. The fee stream transonic Mach number is kept fixed at 0.77 while the angle of attack was varied from 2° to 7°. The transonic buffet is determined by the appearance of fluctuating aerodynamic properties such as lift coefficient, drag coefficient and static pressure fluctuation at particular combination of flow conditions. A detailed analysis on the buffet flow together with the large scale self-excited shock oscillation are investigated for the range of flow conditions.

.

2. Numerical Methods

2.1. Governing equations

The flow in this study is considered to be viscous, compressible, turbulent, and unsteady. Governing equations for the present RANS computations are the conservation of mass, conservation of momentum and the energy equations written in 2-D coordinate system. Two additional transport equations of k-ω SST (Shear Stress Transport) turbulence model are included to model the turbulence in the flow field. The governing equation can be written in the following vector form:

$$\frac{\partial \boldsymbol{U}}{\partial t} + \frac{\partial \boldsymbol{E}}{\partial x} + \frac{\partial \boldsymbol{F}}{\partial y} = \frac{\partial \boldsymbol{R}}{\partial x} + \frac{\partial \boldsymbol{S}}{\partial y} + \boldsymbol{H} \tag{1}$$

Here $\boldsymbol{U}$ is the conservative flux vector. $\boldsymbol{E}$ and $\boldsymbol{F}$ are the inviscid flux vectors and $\boldsymbol{R}$ and $\boldsymbol{S}$ are the viscous flux vectors in the x and y directions, respectively. $\boldsymbol{H}$ is the source terms corresponding to turbulence.

The governing equations are discretized spatially using a Finite volume method of second order scheme. For the time derivatives, an implicit multistage time stepping scheme, which is advanced from time t to time $t + \Delta t$ with a second order Euler backward scheme for physical time and implicit pseudo-time marching scheme for inner iteration, is used. A time step size of 10^{-5} was sufficient for this type of unsteady computation.

2.2. Computational Domain and Boundary Condition

The computational domain together with the grids are shown in Fig. 1(a). The chord length c of NASA SC(2) 0714 supercritical airfoil is considered to be 152.4 mm. The upstream and downstream boundaries are located at 11.5c and 21c, from the leading edge of the airfoil. On the other hand, the top and bottom boundaries are 12.5c apart from the airfoil surfaces. This spacing was considered to be sufficient to apply free-stream conditions on the outer boundaries. The adiabatic no-slip conditions are applied to airfoil surfaces. The Reynolds number based on the airfoil chord length, $\mathrm{Re} = 2.8\times10^6$.

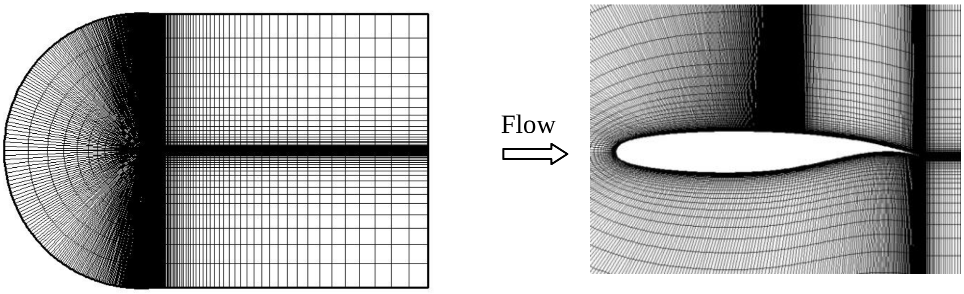

(a) (b)

Fig. 1. (a) Computational domain with grids; (b) Closed-up view of grids around NASA SC(2) 0714 Airfoil.

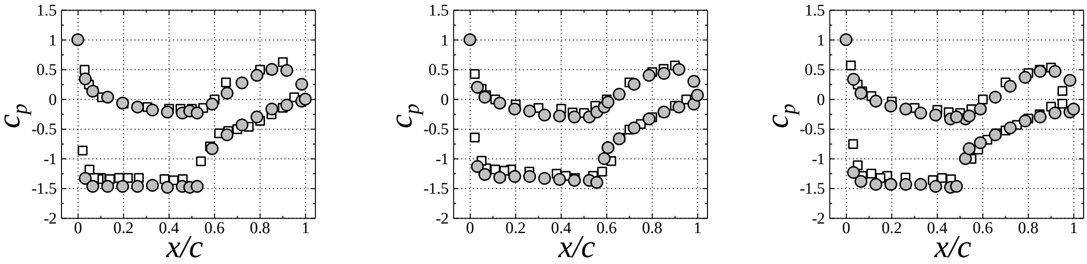

(a) (b) (c)

Fig. 2. Distribution of pressure coefficient along the airfoil surfaces; (a) $M_\infty = 0.72$, $\alpha = 2.5^o$; (b) $M_\infty = 0.74$, $\alpha = 2.0^o$ and (c) $M_\infty = 0.74$, $\alpha = 3.0^o$.

A structured clustered grid system using quadrilateral cells was employed in the computations. The total number of grids is 51000 which gives a grid independent solution. For viscous flow calculation, extra fine spaced grids was constructed over the airfoil surfaces as shown in Fig. 1(b). The first point above the airfoil surface is located at 0.0000169*c* from the airfoil surface which corresponds to $y^+ < 1$. A solution convergence was obtained when the residuals for each of the conserved variables were reduced below the order of magnitude 5.

3. Computational validation

Before going to the detail discussion of the present problem, the computational results have been validated with the available experimental data. Computational validation has been performed by comparing pressure coefficients over the supercritical airfoil for three different conditions. Experimental results are obtained from Ref. [9].

Figure 2 shows the distribution of pressure coefficient, c_p along the airfoil surfaces obtained both from the experiments and the computations for different buffet conditions. The open square symbols are the experimental data and the closed circles are the computational results. In general the trend of c_p are same along the airfoil surfaces both from experiment and the computations. The positions of the shock wave are also at the identical positions for both experimental and computational cases. However, for $M_\infty = 0.72$, $\alpha = 2.5^o$, computational results are showing larger pressure drop than the experimental values on the upper surface of the airfoil as shown in the Fig 2 (a). However, a good relation exists between the experiment and present computational results for other conditions as shown in Figs. 2(b) and 2(c).

4. Results and Discussion

For $M_\infty = 0.77$ and $\alpha = 2°$ a steady normal shock is observed along the mid-chord position of airfoil. The Mach number is gradually increased and forms a supersonic region around the upper surface of the airfoil. The shock Mach number is 1.40 in this case. Behind the shock wave, a subsonic region is found up to the trailing edge. Type 1 shock – boundary layer interaction is detected proposed by Mundell and Mabey [12]. Moreover, an attached flow region all over the upper surface is observed.

In case of $M_\infty = 0.77$ and $\alpha = 3°$ as shown in Fig. 3 , the shock Mach number is found to be 1.45. At this case transonic shock buffet is observed with small displacement of shock wave which can be assured with fluctuated lift and drag coefficient. From Mach contour in one cycle of shock oscillation it is observed that from $t = 1/11\ T$ to $3/11\ T$, the supersonic region is wider; however from $t = 3/11\ T$ to $t = 8/11\ T$, it becomes narrower. And from $t = 9/11T$ to $t = 11/11T$ it becomes wider again. Type 1 shock – boundary layer interaction with attached flow region throughout the upper surface is detected proposed by Mundell and Mabey [12]. No signification formation of vertex is observed during this time period.

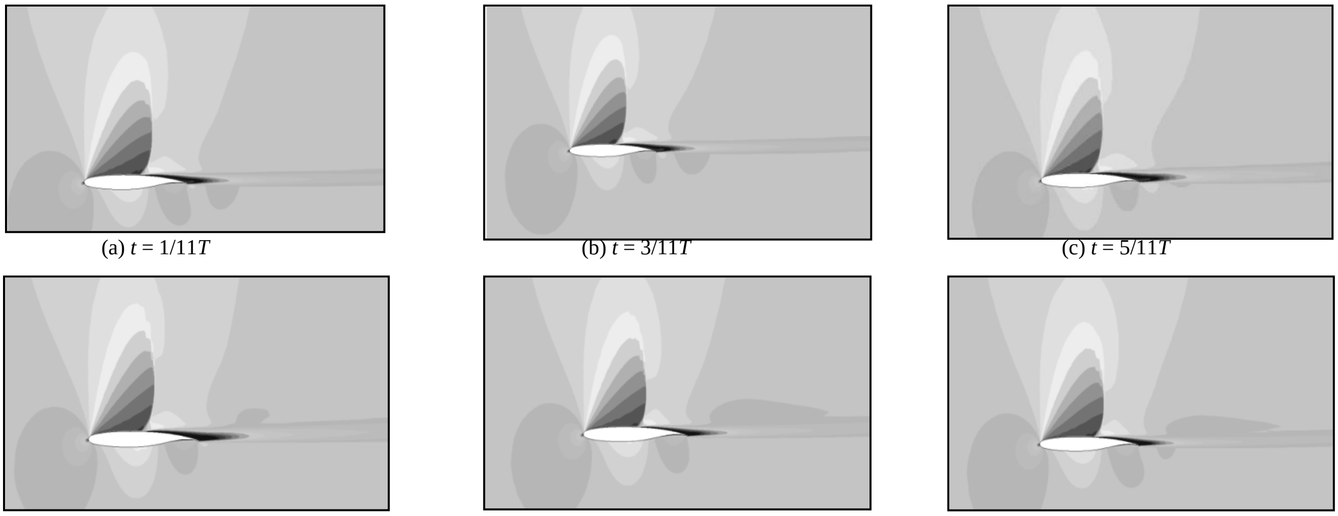

(a) $t = 1/11T$ (b) $t = 3/11T$ (c) $t = 5/11T$

(d) $t = 7/11T$ (e) $t = 9/11T$ (f) $t = 11/11T$

Fig. 3. Contours of Mach number during one cycle of flow oscillation, T for $M_\infty = 0.77$, $\alpha = 3°$.

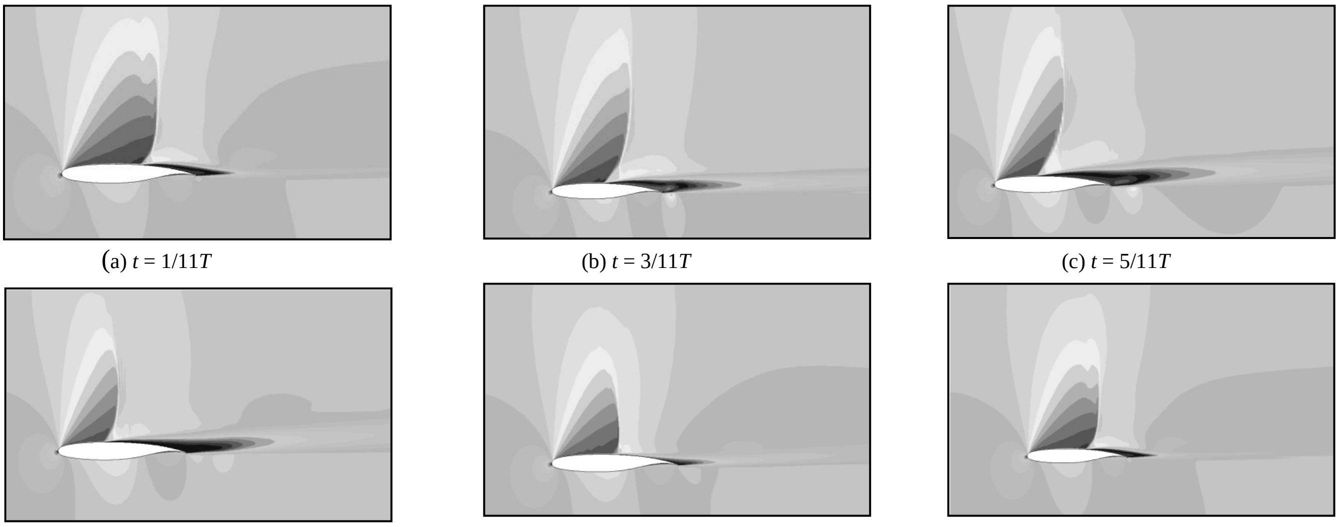

(a) $t = 1/11T$ (b) $t = 3/11T$ (c) $t = 5/11T$

(d) $t = 7/11T$ (e) $t = 9/11T$ (f) $t = 11/11T$

Fig. 4. Contours of Mach number during one cycle of flow oscillation, T for $M_\infty = 0.77$, $\alpha = 4°$.

Results for $M_\infty = 0.77$, $\alpha = 4°$ during one cycle of shock oscillation are shown in Fig. 4. During the oscillation, the shock motion is clearly visible and the maximum shock Mach number increases in this case compared to Fig. 3. Type 1 shock – boundary layer interaction is detected from $t = 1/11\ T$ to $t = 3/11\ T$; however Type 3 shock – boundary layer interaction is observed from $t = 5/11\ T$ to $t = 7/11\ T$. After that again Type 1 shock – boundary layer interaction is noticed. As a result, attached flow is observed from $t = 1/11\ T$ to $t = 3/11\ T$ throughout the upper surface, separated flow is observed from $t = 5/10\ T$ to $t = 7/10\ T$ from shock position to trailing edge. And again attached flow is found for the rest of the time instants. During the separated flow, a bulge is observed which then forms a new vortex and becomes larger. A secondary vortex is also formed at the vicinity of trailing edge which coalesces and forms large separated flow region.

The cases of $\alpha = 5°$ and 6° showed the almost the same results with fluctuating supersonic zone and hence the unsteady shock movement. The shock excursion zone for these cases are more intensified compared to the previous cases. However, the contour maps of Mach number are not presented here for brevity. However, results for $\alpha = 7°$ are shown in Fig. 5. In this case, Type 2 shock – boundary layer interaction is observed from $t = 1/11T$ to $t = 5/11T$ time instance and from $t = 9/11T$ to $t = 11/11\ T$ time instance. Again Type 3 shock – boundary layer interaction is noticed at $t = 5/11T$ to $t = 7/11T$ time instance. Fully separated flow region all over the upper surface is observed throughout the cycle. During the separated flow region a bulge is observed which then forms a new vortex and becomes larger. A secondary vortex is also formed at the vicinity of trailing edge which coalesces and forms large separated flow region.

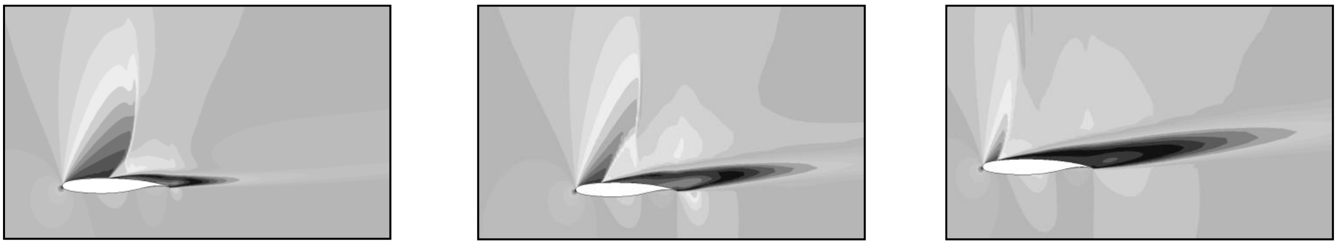

(a) $t = 1/11T$ (b) $t = 3/11T$ (c) $t = 5/11T$

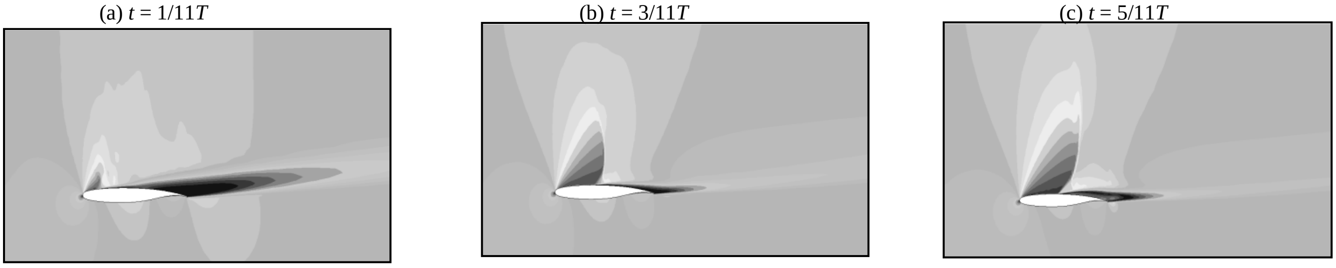

(d) $t = 7/11T$ (e) $t = 9/11T$ (f) $t = 11/11T$

Fig. 4. Contours of Mach number during one cycle of flow oscillation, T for $M_\infty = 0.77$, $\alpha = 7°$

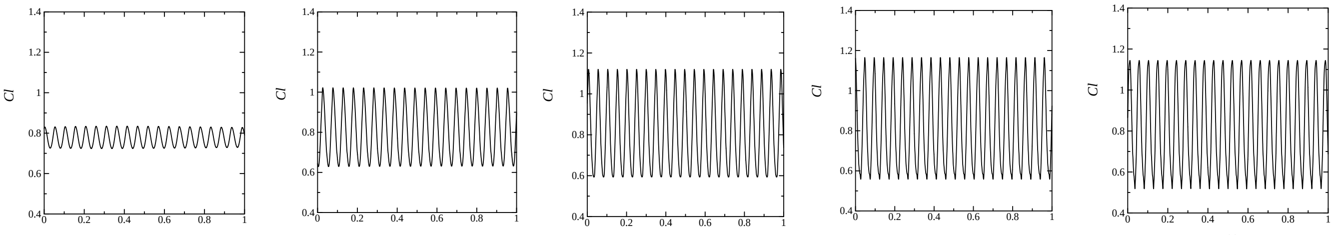

(a) (b) (c) (d) (e)

Fig. 6. Evolution of lift coefficient C_l at $M_\infty = 0.77$; (a) $\alpha = 3°$, (b) $\alpha = 4°$, (c) $\alpha = 5°$, (d) $\alpha = 6°$, (e) $\alpha = 7°$

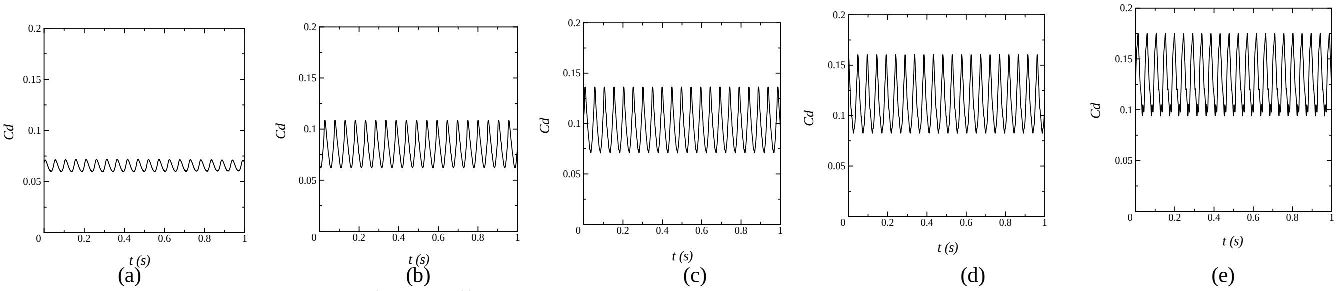

(a) (b) (c) (d) (e)

Fig. 7. Evolution of drag coefficient C_l at $M_\infty = 0.77$; (a) $\alpha = 3°$, (b) $\alpha = 4°$, (c) $\alpha = 5°$, (d) $\alpha = 6°$, (e) $\alpha = 7°$

The transonic buffet phenomena is further confirmed by the fluctuation lift and drag coefficients as shown in Figs. 6 and 7, respectively. The amplitude of aerodynamic oscillation is increased with an increase of angle of attack for the same Mach number. The mean c_l's are 0.730 (constant), 0.779, 0.826, 0.857, 0.862, 0.831 for $\alpha = 2°, 3°, 4°, 5°, 6°$, and 7°, respectively as shown in Fig. 6. The amplitudes of c_l fluctuation are 0.102, 0.389, 0.526, 0.605, 0.626 for $\alpha = 3°, 4°, 5°, 6°$, and 7°, respectively. Moreover, from Fig. 7 it was found that the mean c_d's are 0.05 (constant), 0.066, 0.085, 0.104, 0.122, 0.135 for $\alpha = 2°, 3°, 4°, 5°, 6°$, and 7°, respectively. And the fluctuating amplitude associated with c_d are 0.011, 0.046, 0.065, 0.078, 0.081 for $\alpha = 3°, 4°, 5°, 6°$, and 7°, respectively.

Time histories of static pressure are measured at different streamwise locations along the upper surface of the airfoil. Results are shown for $\alpha = 7°$ in Fig. 8 for brevity. It is found that the shock boundary interaction causes the fluctuation in static pressure along the upper surface. The intensity of pressure fluctuation increases from x/c=0.10 and reaches the maximum at x/c= 0.40. After that the pressure fluctuation decreases due to reduced shock induced boundary layer separation.

Due to the unsteady phenomena of static pressure from the pressure history along the airfoil upper surface, it has become essential to find out highest pressure prone area along the airfoil. The unsteady root mean square (RMS) of pressure oscillations are evaluated to identify intensified pressure position from 2° to 7°. P_{rms} is calculated as

$$p_{rms} = \sqrt{\sum_{i=1}^{n} \frac{(p_i - \overline{p})^2}{n}} \qquad \text{where} \qquad \overline{p} = \sum_{i=1}^{n} \frac{p_i}{n}$$

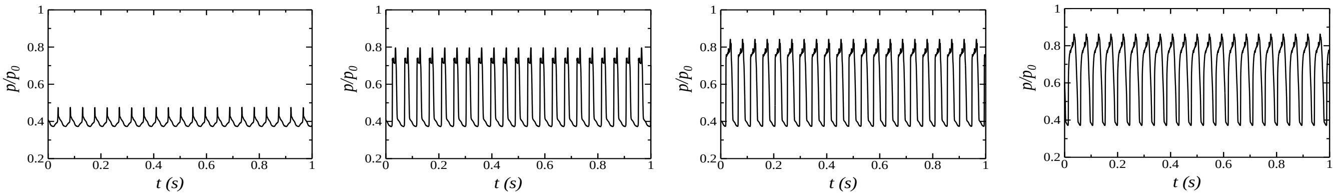

(a) x/c = 0.10 (b) x/c = 0.20 (c) x/c = 0.30 (d) x/c = 0.40

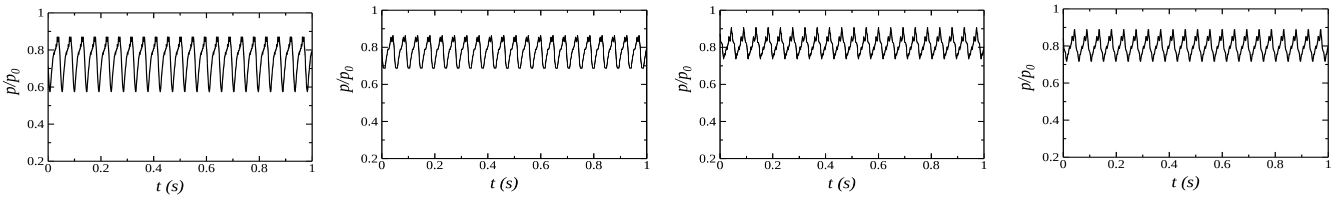

(e) x/c = 0.50 (f) x/c = 0.60 (g) x/c = 0.70 (h) x/c = 0.80

Fig. 8. Static pressure time histories at the upper surface of the airfoil for M_∞ = 0.77, α = 7° along the different axial positions

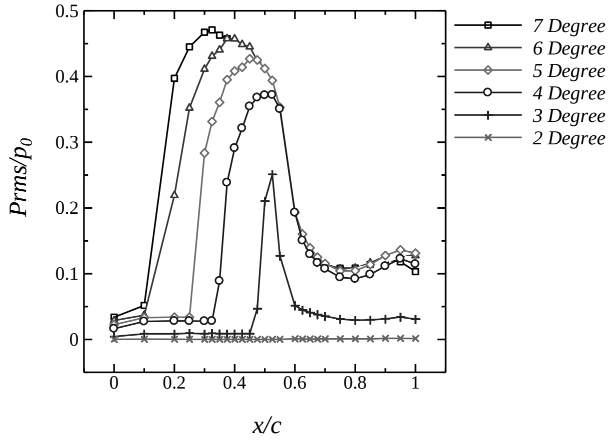

Fig. 9. Root mean square of static pressure, $Prms/p_0$ distribution along the airfoil upper surface for different angles of attack

In the above equation, p_i is the instantaneous static pressure, $\overline{p}$ is the time mean static pressure and n is the number of sampling points. For the calculation of p_{rms}, n is taken as 10^4. p_{rms} is normalized with free stream static pressure p_0 and the results are shown in Fig 9. As there is no shock oscillation for 2°, the value of p_{rms} is zero along the airfoil upper surface. For 3° angle of attack, p_{rms}/p_0 starts to increase from leading edge and shows a peak value of 0.251 at 52.5% c. This signifies large pressure fluctuation and intensity at this location. Further movement upto trailing edge shows sudden drop of p_{rms}/p_0 at 60% chord location which decreases slowly ahead of 95% c. At 95% of chord location, there is a tendency to rise of p_{rms}/p_0 is observed with a value of 0.034 due to pressure fluctuation for the result of vortex formation at this separated flow region. Further increase in angle of attack leads to forward movement of intensified position of pressure oscillation. For 4° angle of attack, the value of peak p_{rms}/p_0 is 0.372 at 52.5% of chord position. With advancement upto trailing edge shows decrease of p_{rms}/p_0 value ahead 95% of chord location. For this case also at 95% of chord location sudden rise of p_{rms}/p_0 with a value of 0.123 is observed due to vortex formation and interaction with trailing edge. For 5° angle of attack, the peak value is found to be 0.427 at 45% chord location. Further increase of angle of attack leads to forward movement of intensified position of airfoil along with the increment of p_{rms}/p_0. For 6° angle of attack value of peak p_{rms}/p_0 is 0.457 at 37.5% of chord position. And finally, the peak p_{rms}/p_0 is found to be 0.47 at 32.5% chord location for 7° angle of attack.

5. Conclusions

A computational study using Raynolds Averaged Navier-Stokes (RANS) equations has been performed to investigate the transonic buffer phenomena over a supercritical airfoil NASA SC(2) 0714 for a fixed free-stream mach number of 0.77 while the angles of attack are varied from 2° to 7°. The computational results have been validated witht the available experimental data. The results obtained from the present study can be summerized as below:

- The present RANS computation can capture the transonic buffet phenomena acurately for flow over a supercritical airfoil NASA SC(2) 0714.
- No shock oscillation is observed at angle of attack of 2° for M_∞=0.77.

- Self-sustained shock oscillation and hence the transonic buffet is observed for angle of attack of 3° to 7° for the same Mach number of M_∞=0.77.
- Shock oscillating zone along the upper surface of the airfoil is increased with an increase of angle of attack.
- The intensity of shock-boundary layer interaction is increased for higher angles of attack.
- The unsteady shock movement creates the fluctuations in aerodynamic peoperties such as lift and drag.
- The transonic buffet is further confirmed by the static pressure fluctuation along the upper surface of the airfoil.
- The magnitude of peak root mean square (RMS) of pressure oscillation is increased with an increase of angle of attack.
- The position of peak RMS of pressure oscillation is shifted toward the leading edge of the airfoil with increasing angle of attack.

References

[1] Crouch, J. D., Garbaruk, A., Magidov, D., Travin, A., 2009. Origin of Transonic Buffet on Aerofoils, Journal of Fluid Mechanics, 628, p. 357.
[2] Lee, B. H. K., 2001. Self-sustained Shock Oscillations on Airfoils at Transonic Speeds, Progress in Aerospace Sciences, 37, p.147.
[3] Lee, B. H. K., 1990. Oscillatory Shock Motion caused by Transonic Shock-boundary Layer Interaction, AIAA Journal, 28, p.942.
[4] Gillan, M. A., 1995. "Navier-Stokes Simulation of Self-excited Shock Induced Oscillations", AIAA- 95-1809.
[5] Rumsey, Christopher L., Sanetrick, Mark D., Biedron, Robert T., Melson, N. Duane, Parlette, Edward B. , 1995. Efficiency and Accuracy of Time-accurate Turbulent Navier-Stokes Computations, Proc. of the 13th AIAA Applied Aerodynamics Conference, AIAA-95-1835.
[6] Chen, L.W., Xu, C.Y., Lu, X.Y., 2010. Numerical Investigation of Compressible Flow Past an Aerofoil, Journal of Fluid Mechanics, 643, p.97.
[7] McDevitt, J. B.; Levy, L. L., Jr.; and Deiwert, G. S., 1976. Transonic Flow about a Thick Circular-Arc Airfoil, AIAA Journal, 14, p.606.
[8] Edwards, J. W., 1993. "Transonic Shock Oscillations Calculated with a New Interactive Boundary Layer Coupling Method", AIAA-93-0777.
[9] Bartels, R., E, and Edwards, J. W., 1997. "Cryogenic Tunnel Pressure Measurements on A Supercritical Airfoil for Several Shock Buffet Conditions", NASA TM-110272.
[10] Deck, S., 2005. Numerical Simulation of Transonic Buffet over A Supercritical Airfoil, AIAA Journal, 43, p.1556.

[11] Xiao, Q., Tsai, H., Liu, F., 2006. Numerical Study of Transonic Buffet on A Supercritical Airfoil, AIAA Journal, 44, p.620.

[12] Mundell A.R.G., Mabey D.G.,1986. Pressure Fluctuation caused by Transonic Shock/ Boundary-layer Interaction, Aeronautical Journal, p. 274.